

# Computational Evaluation of Shear Stress and Restenosis in Stented Coronary Arteries Using Optical Coherence Tomography

Joshua K. Hughey  
*Marquette University*

---

## Recommended Citation

Hughey, Joshua K., "Computational Evaluation of Shear Stress and Restenosis in Stented Coronary Arteries Using Optical Coherence Tomography" (2014). *Master's Theses (2009 -)*. Paper 246.  
[http://epublications.marquette.edu/theses\\_open/246](http://epublications.marquette.edu/theses_open/246)

COMPUTATIONAL EVALUATION OF SHEAR STRESS AND  
RESTENOSIS IN STENTED CORONARY ARTERIES USING  
OPTICAL COHERENCE TOMOGRAPHY

by

Joshua K. Hughey

A Thesis Submitted to the Faculty of the Graduate School,  
Marquette University,  
in Partial Fulfillment of the Requirements for  
the Degree of Master of Science

Milwaukee, Wisconsin

May 2014

ABSTRACT  
COMPUTATIONAL EVALUATION OF SHEAR STRESS AND  
RESTENOSIS IN STENTED CORONARY ARTERIES USING  
OPTICAL COHERENCE TOMOGRAPHY

Joshua K. Hughey

Marquette University, 2014

The cause of coronary artery neointimal thickness (NT) leading to restenosis in ~10% of drug-eluting stents (DES) is unknown, but adverse wall shear stress (WSS) may contribute. Prior studies comparing WSS to restenosis for first generation DES yielded conflicting results, and cited different mechanisms of action for DES agents. Studies to date have not accounted for stent geometry, which dictates local WSS patterns influencing drug concentration. The objective of this investigation was to evaluate current generation stent platforms via their WSS patterns and their respective impact on NT.

We prospectively enrolled 19 patients, who were randomized to thin-strut (81 $\mu$ m) 2-link Promus element (PE: n=7), thin-strut 3-link Xience Prime (XP: n=6), or thick-strut (145 $\mu$ m) 2-link Nobori stents (NO: n=6), and underwent optical coherence tomography (OCT) and coronary CT angiography (CTA) post-stenting (PS) and after 9-months follow-up (FU). PS and FU WSS were calculated using computational fluid dynamics (CFD) simulations of patient-specific 3D arteries reconstructed by the fusion of OCT and CTA data, and normalized to WSS in the proximal unstented region.

Stent-to-vessel area ratios were less in PE and XP than NO (0.24 $\pm$ 0.04 and 0.21 $\pm$ 0.03 vs. 0.34 $\pm$ 0.04, respectively;  $P < 0.05$ ). The difference between the NO and XP was significant. PS normalized stent-induced low WSS area/stent length was least in PE, followed by XP and NO (1.05 $\pm$ 0.27, 1.10 $\pm$ 0.20 and 2.00 $\pm$ 0.41 mm<sup>2</sup>/mm, respectively,  $P < 0.05$ ). The difference between the NO and PE was significant. When combining the data from the proximal, middle, and distal regions, an inverse correlation between PS WSS and NT at FU was greatest for the NO (-0.019 $\pm$ 0.001 mm/Pa) followed by PE (-0.017 $\pm$ 0.003 mm/Pa) and XP (-0.008 $\pm$ -0.003 mm/Pa). The difference in inverse correlation between the NO and XP was significant.

The difference in correlations of PS normalized WSS and NT at FU between the biolimus-eluting NO and everlimus-eluting XP stents may be attributed to the mechanisms of action for the specific elution agents. CFD simulations using OCT and CTA suggest that DES with thicker struts and a greater stent-to-vessel area ratio produce more adverse WSS, which may lead to a higher risk for restenosis and be influenced by DES agent.

## ACKNOWLEDGEMENTS

Joshua K. Hughey

First, I am deeply thankful for the opportunity my advisor and mentor, Dr. LaDisa, provided me by allowing me to join his lab. It was not a week after we spoke on the phone for the first time that he gave me a tour around Marquette and offered me a graduate research position. His passion and drive for cardiovascular research is passed on to everyone participating in his lab or coursework. He has provided guidance both academically and professionally and I look forward to continuing the relationship in the future.

I would like to thank all my committee members, Dr. Ellwein, Dr. Otake, and Dr. Gilat-Schmidt, for the time and effort put forth to advance my research presented in this thesis.

I am extremely grateful for the assistance of Dr. Ellwein throughout this project. Not only did she create the principal algorithm used for artery reconstruction, she was always willing to field the endless amount of questions I had over the past two years. Her assistance was greatly appreciated when troubleshooting code and creating new protocols.

I would like to thank Dr. Otake for his collaboration during this project. His insight when attempting to analyze and understand the data and results was tremendously valuable. Despite the time difference, Dr. Otake and his entire team at Kobe University were always able to resolve any issue or discrepancy with the data in short order. Without their hard work, this collaboration would not be possible.

I would like to thank Dr. Gilat-Schmidt. When participating in her image processing course, she related specific concepts to different areas of research including cardiovascular research. Algorithms generated with her help throughout her course are not only used in this specific project, but in projects throughout our entire research lab.

From the University of Missouri, I would like to thank Dr. John Viator. He graciously allowed me to join his lab as an undergraduate. While in his lab, not only did he guide me in my specific research project, he taught me how to perform scientific research. Without his guidance as an undergraduate, I would not have been equipped to become a graduate researcher.

I want to thank all my friends in the Laboratory for Translational, Experimental, and Computational Cardiovascular Research as well as the entire Biomedical Engineering Department. I have enjoyed our intellectual discussions regarding research as well as all the fun we had outside of school. I would also like to thank Kelsey Allison. From my undergraduate to graduate coursework and research, she has always been there to support me.

I want to thank my family. First, I want to thank my siblings, Jake and Becca. Whether it was on an athletic field, in the class room, or in my field of research, they have always been there to support me. For this love and support, I am forever grateful. Finally, I want to thank my parents, Ken and Judy. None of my success would have been

possible without their love and guidance. While my debt to you will forever be endless, I hope this piece of work is something you can look back on and be proud of.

## TABLE OF CONTENTS

ACKNOWLEDGEMENTS .....	i
LIST OF FIGURES .....	vi
LIST OF ACRONYMS .....	xii
CHAPTER 1: INTRODUCTION AND SPECIFIC AIMS .....	1
1.1 Cardiovascular Disease .....	1
1.2 Treatment Methods for Cardiovascular Disease .....	2
1.3 Restenosis and Thrombosis After Stenting .....	4
1.4 Restenosis Causing Blood Flow Alterations .....	4
1.5 Methods of Evaluating the Effectiveness of Stents .....	5
1.5.1 Intravascular Ultrasound .....	6
1.5.2 Optical Coherence Tomography .....	7
1.6 CFD as a Tool for Modeling Blood Flow .....	8
1.7 Objective and Specific Aims .....	9
1.7.1 Aim 1: Confirm Previous Studies Relating Low WSS and Stent Geometry .....	13
1.7.2 Aim 2: Comparison Between Post-Stent and Follow-up Low Normalized WSS .....	13
1.7.3 Aim 3: Evaluate Post-Stent WSS and Follow-up NT .....	14
CHAPTER 2: METHODS .....	15
2.1 Data Acquisition .....	15
2.2 Patient-Specific Vessel Reconstruction .....	16
2.2.1 Image Processing .....	16
2.2.2 Wire Pathway Reconstruction .....	17

2.2.3 Segment Registration .....	17
2.2.4 Model Assembly .....	19
2.3 Computational Stent Implantation .....	20
2.4 Steps Performed to Assure Accuracy During Vessel Reconstruction .....	22
2.5 Specification of CFD Boundaries Conditions and Simulation Parameters ....	26
2.6 Anisotropic Meshing of Patient-Specific Models.....	30
2.7 Data Normalization.....	30
2.8 Data Quantification Points.....	32
2.8.1 Regional Quantification.....	32
2.8.2 Local Quantification .....	34
2.9 Statistical Analysis.....	37
CHAPTER 3: RESULTS.....	39
3.1 Patient-Specific WSS and OSI Results.....	39
3.1.1 Post-Stenting Results .....	39
3.1.2 Follow-up Results .....	46
3.2 Post-Stenting WSS and Follow-Up Tissue Growth.....	54
3.2.1 Comparison Between Post-Stenting WSS and Follow-Up Neointimal Tissue .....	54
3.2.2 Total Neointimal Growth at Follow-Up .....	59
CHAPTER 4: DISCUSSION.....	61
4.1 Review of Specific Aims and Summary of Major Findings.....	61
4.2 Relationship to Previous Work Underscoring Unique Contributions.....	64
4.3 Limitations .....	67
4.4 Future Directions .....	68

BIBLIOGRAPHY..... 69

APPENDIX..... 76



## LIST OF FIGURES

Figure 1: Normal blood flow in a healthy artery (A) compared to a vessel with atherosclerosis (B). Image obtained from the National Heart Lung and Blood Institute. . 2	2
Figure 2: OCT (right) has ten times the spatial resolution compared to IVUS (left). IVUS image obtained from Nissen; Journal of the American Heart Association 2001..... 8	8
Figure 3: Promus element stent- Boston Scientific (top, multivu.com). Xience prime stent- Abbott Vascular (middle, fda.gov). Nobori stent- Temuro (bottom, terumo-europe.com). ..... 11	11
Figure 4: a) OCT image with lumen (green) and stent (purple) contours. b) and c) Stent and lumen contours, respectively, isolated from RGB image using thresholding previously described by Ellwein et al in CVET 2011. d) and e) Pixel locations for stent and lumen contours, respectively. (Blue point = OCT image center, black dot = contour center). ..... 17	17
Figure 5: Segments registered on the wire pathway (black line) according to vessel landmarks where possible. Remaining segments are then oriented to wire pathway and rotated such that segment centroids align with the vessel centerline (blue line). Vector from the image centroid to the upper-left hand corner was also tracked and plotted (red). ..... 19	19
Figure 6: Combined segments from CT and OCT (a) are lofted along with the branch segments to form a Parasolid model (b). ..... 20	20
Figure 7: Method of virtual stent implantation. Solid models of the outer surface of the stent and vessel lumen (e) were lofted from the purple and green contours of the OCT images (a). The stent model was used to create a shell with the thickness equal to that of the stent (b). The shell was intersected with the thick stent model (c) to create a patient-specific stent model (d). Subtracting the patient-specific stent model (d) from the lumen model (e) generated a computational representation of the blood flow domain (f)..... 21	21
Figure 8: Model produced from Gundert et al that does not account for malapposed struts (left). Model produced from current method that can create malapposed struts (right). . 22	22
Figure 9: Processes for assuring accuracy while creating patient-specific coronary models. .... 23	23

Figure 10: Abnormality (i.e. dissection) in the lumen contour that requires an increase in segment points. .... 24


Figure 11: OCT image (left). Slice from initial virtual stent implantation with struts not matching OCT image (middle). Slice after applying a specific rotation to the stent in Solidworks to better match the OCT image (right). \* = guidewire artifact.  = stent strut. .... 26

Figure 12: Using flow waveform, blood pressure, impedance spectra, and RCR parameters to replicate physiologic behavior (Fm=mean flow, Pm=mean pressure, Rc=characteristic impedance, Rd=distal resistance, C=capacitance, PPd=pulse pressure predicted by model, PPa=pulse pressure method). Image obtained from Westerhof, American Phys. Society, 1999. .... 29

Figure 13: Different values of WSS proximal to the stented region for three different patients. .... 31

Figure 14: Low normalized WSS distributions produced by the vessel (left) compared to distributions produced by the vessel and stent geometry (right). .... 33

Figure 15: Proximal, middle, and distal regions with maximum scaffolding that were isolated in an effort to correlate post-stenting WSS and follow-up NT. .... 35

Figure 16: WSS results from CFD with the zero degree position line (epicardial surface) from unwrapping (a). Zero degree line with Paraview slice (b). OCT image (c) and Paraview slice (d) are isolated to create their respective contours (e and f, respectively). Rotations  $\theta$  and  $\alpha$  are determined for the OCT contour and Paraview slice between the initial zero degree point and the epicardial surface. Rotations are applied to the lumen contour (g) and Paraview slice (h) making the final zero degree position spatially consistent.  $90^\circ$ ,  $180^\circ$ , and  $270^\circ$  positions are plotted to assure all points are spatially consistent. .... 37

Figure 17: Post-stenting distributions of low normalized WSS. .... 40

Figure 18: Post-stenting distributions of OSI > 0.1. .... 41

Figure 19: Comparison of the stent-to-vessel area ratio, \*=significance (mean $\pm$ SEM)... 42

Figure 20: Comparison of the post-stenting normalized area of low WSS as a percentage of the entire vessel (mean $\pm$ SEM). .... 43

Figure 21: Comparison of the post-stenting normalized stent-induced area of low WSS (mean±SEM).....	44
Figure 22: Comparison of the post-stenting normalized stent-induced area of low WSS per stent length, *=significance (mean±SEM).....	45
Figure 23: Comparison of the post-stenting stent-induced OSI greater than 0.1, *=significance (mean±SEM). ....	46
Figure 24: Follow-up distributions of low normalized WSS.....	47
Figure 25: Follow-up distributions of OSI > 0.1. ....	48
Figure 26: Comparison of the follow-up normalized area of low WSS as a percentage of the entire vessel (mean±SEM). ....	49
Figure 27: Comparison of the follow-up normalized stent-induced area of low WSS per stent length (mean±SEM). ....	50
Figure 28: Post-stenting and follow-up distributions of low normalized WSS.....	51
Figure 29: Comparison of the post-stenting and follow-up normalized area of low WSS as a percentage of the entire vessel, *=significance (mean±SEM).....	52
Figure 30: Comparison of the follow-up OSI greater than 0.1 (mean±SEM). ....	53
Figure 31: Comparison between post-stenting and follow-up OSI greater than 0.1 (mean±SEM).....	54
Figure 32: OCT image at follow-up (a) with circumferential NT measurements starting at the zero degree position (b). Paraview slice at post-stenting (c) with circumferential WSS measurements starting at the zero degree position (d). Correlation between post-stenting WSS and NT at follow-up (e). ....	55
Figure 33: Distal region comparison of inverse correlations of post-stenting WSS and follow-up neointimal thickness represented by the r-value and slope from regression analysis (mean±SEM).....	56

Figure 34: Middle region comparison of inverse correlations of post-stenting WSS and follow-up neointimal thickness represented by the r-value and slope from regression analysis (mean±SEM).....	56
Figure 35: Proximal region comparison of inverse correlations of post-stenting WSS and follow-up neointimal thickness represented by the r-value and slope from regression analysis (mean±SEM).....	57
Figure 36: High WSS region comparison of inverse correlations of post-stenting WSS and follow-up neointimal thickness represented by the r-value and slope from regression analysis (mean±SEM).....	57
Figure 37: Low WSS region comparison of inverse correlations of post-stenting WSS and follow-up neointimal thickness represented by the r-value and slope from regression analysis (mean±SEM).....	58
Figure 38: Combined proximal, middle, and distal regions comparison of inverse correlations of post-stenting WSS and follow-up neointimal thickness represented by the r-value and slope from regression analysis, *=significance (mean±SEM).....	58
Figure 39: Comparison of the change in volume from post-stenting to follow-up (mean±SEM).....	59
Figure 40: Comparison of the change in volume from post-stenting to follow-up as a percent of post-stenting volume (mean±SEM). ....	60
Figure 41: 3D volume in Volview showing the size in voxels and image spacing. ....	79
Figure 42: Using ImageJ, determine the Image Position for the most superior image.....	79
Figure 43: X, Y, and Z shifts output in Matlab.....	80
Figure 44: Naming the slice and creating the segment matrix.....	81
Figure 45: Saving the 'vesseln_sparse' or 'vesseln_one', depending if the image has an anomaly.....	83
Figure 46: Adjusting the number of points being saved for a contour. ....	84

Figure 47: Illustrating the X, Y, and Z coordinates of contours. ....	85
Figure 48: Determining the landmark positions in ITK-Snap and inserting them into Matlab. ....	87
Figure 49: Determining which OCT images correspond to the landmark positions. ....	88
Figure 50: Creating the matrices for find_pathpoints.m. ....	89
Figure 51: Adding the mm/pixel ratio. ....	91
Figure 52: Setting the candidate points (circled) for the landmark positions. ....	91
Figure 53: Transducer candidate points for the proximal and distal regions. ....	93
Figure 54: Setting up for-loops to properly determine transducer pathway. ....	94
Figure 55: Final rotated segments with the centerline (blue) and transducer pathway (black). Also, the upper-left hand corner of the images is tracked and plotted. ....	99
Figure 56: Naming the group for Simvascular. ....	100
Figure 57: Naming the groups in the group_contents file. ....	100
Figure 58: Truncating the transducer pathway based on the stented region. ....	102
Figure 59: Inputs for orient.m. ....	105
Figure 60: Setting 's' to be the OCT image being quantified. ....	107
Figure 61: Determining 'deg_shift', if the circumferential shift was applied in the wrong direction, comment out 'deg_shift' that was used and un-comment the other one. Note, one instance must be commented. ....	107
Figure 62: Final zero and epicardial surface (lime green point) are in the same location. Initial zero degree location (forest green point) and final 90 degree locations (blue point) are also plotted. ....	108

Figure 63: Example of shift being applied in the wrong direction. Final zero degree location (black point) and epicardial surface (lime green point) do not overlap. ....	109
Figure 64: WSS versus circumferential location plot. ....	110
Figure 65: Inputs for thickness.m program. ....	111
Figure 66: Thickness versus circumferential location plot. ....	112

LIST OF ACRONYMS  
(in order of appearance)

CVD = cardiovascular disease	FD-OCT = frequency-domain optical
CAD = coronary artery disease	coherence tomography
LDL = low density lipoprotein	CTA = computed tomography
BMS = bare-metal stent	angiography
DES = drug-eluting stent	SEM = standard error of the mean
PTCA = percutaneous transluminal	
coronary angioplasty	
NH = neointimal hyperplasia	
NT = neointimal thickness	
LST = late-stent thrombosis	
WSS = wall shear stress	
OSI = oscillatory shear index	
OCT = optical coherence tomography	
CFD = computational fluid dynamics	
IVUS = intravascular ultrasound	
TD-OCT = time-domain optical	
coherence tomography	

# Chapter 1

---

## Introduction and Specific Aims

### 1.1 Cardiovascular Disease

According to the American Heart Association, approximately 84 million Americans have some form of cardiovascular disease (CVD)[1]. The most prevalent form of CVD is coronary artery disease (CAD). CAD affects approximately 51% of those suffering from CVD and is the leading cause of death in the United States[1].

The coronary arteries are the heart's main source of blood, oxygen, and nutrients. CAD is caused by damage or disease to these vessels. The main contributor to CAD is atherosclerosis, defined as the hardening and narrowing of a blood vessel due to plaque build-up (Figure 1)[2]. The process of atherosclerosis begins when the endothelial cells lining the inside of the vessel wall are damaged. This damage can be caused by many factors including, but not limited to, high blood pressure, smoking, and elevated cholesterol levels. In particular, low-density lipoproteins (LDL) invade the damaged endothelium and enter the vessel wall[3]. Over time, the combination of LDL cholesterol and cells such as macrophages and smooth muscle cells form a plaque protruding from the vessel wall into the region available for blood flow. If this protrusion becomes severe enough, blood flow to the heart can be completely occluded resulting in myocardial infarction or death. Alternatively, the plaque may rupture, causing a local inflammatory reaction that may occlude the artery.



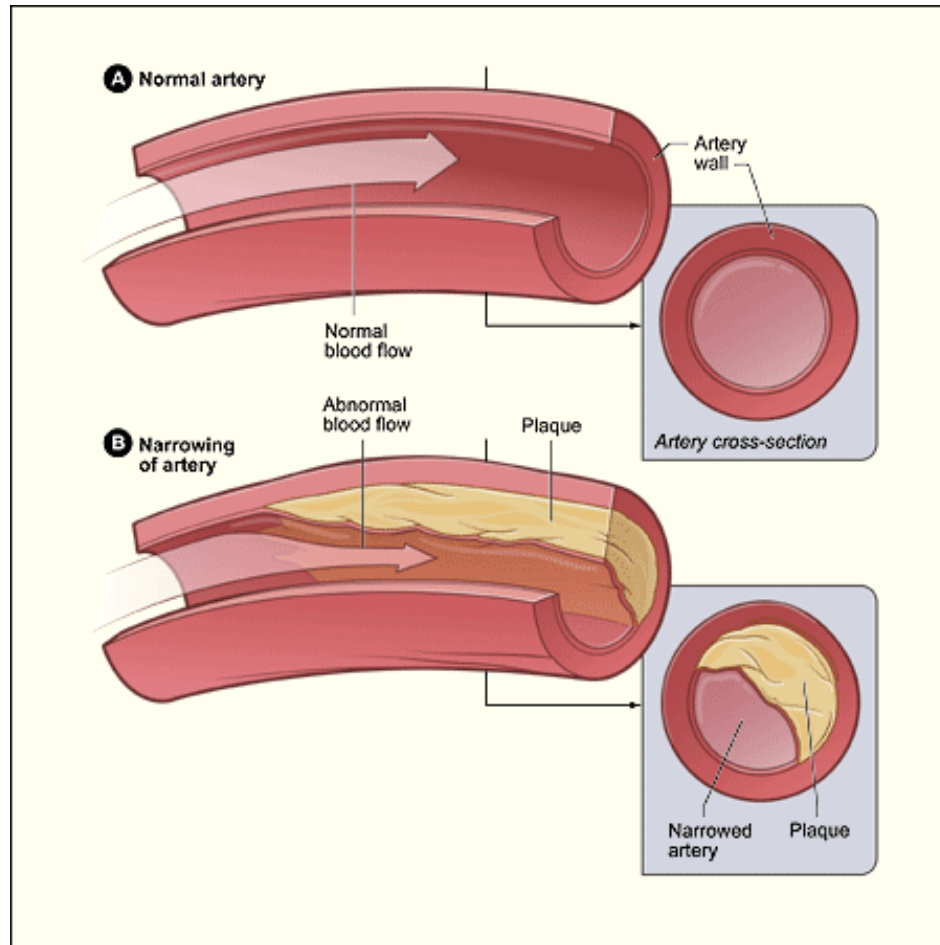


Figure 1: Normal blood flow in a healthy artery (A) compared to a vessel with atherosclerosis (B). Image obtained from the National Heart Lung and Blood Institute.

## 1.2 Treatment Methods for Cardiovascular Disease

Today, the standard form of treatment for CAD is stenting. Stents act as scaffolding mechanisms and are permanently embedded into the vessel wall in an effort to eliminate the effects of the plaque build-up. There are two main types of balloon-expandable stents, bare metal (BMS) and drug eluting (DES). A brief review of both technologies is provided below.

The introduction of BMS as a treatment method was a great advance compared to traditional percutaneous transluminal coronary angioplasty (PTCA). PTCA is a technique in which a deflated balloon is passed through the artery via a guide wire and catheter to

the region of plaque. The balloon is then inflated to a specific pressure in an effort to expand the local atherosclerotic plaque and improve blood flow. While PTCA is often used today as a tool for predilation before stenting, it alone is not a sufficient treatment method due to restenosis rates of 30-40%[4]. Restenosis is defined as a reduction in the luminal diameter of more than 50%[5]. Very recent studies suggest that drug-eluting balloons may reduce the rate of restenosis after PTCA, but long-term data is not yet available[6], [7]. Stents were invented to overcome the limitations of traditional PTCA and BMS were used in over 80% of all coronary interventions by 1999[4]. While BMS continued to grow in popularity as a treatment method, restenosis with the need for revascularization still had an occurrence rate of 20-30%[8].

In an effort to further reduce the occurrence of restenosis and amount of revascularization procedures, DES were introduced in 2001[9]. DES are similar to BMS in scaffold design and fabrication material such as stainless steel or cobalt chromium. However, DES contain a polymer coating of an anti-proliferative agent such as everolimus, biolimus A9, or paclitaxel that is released locally to prevent restenosis. The local drug delivery approach of DES provides a major advantage over systemic drug delivery that was often used previously. Patients were not able to tolerate the toxic doses of the drug when delivered systemically[10]. In contrast, the drug is released locally with DES in order to concentrate the drug to the target site.

Though DES have reduced restenosis rates, studies have shown they do not improve the incidence of late stent thrombosis (LST). LST is defined as blood clot forming 30 days to 1 year after the stent is implanted. This LST along with restenosis are limiting factors in the success of DES. Both factors are reviewed below.

### **1.3 Restenosis and Thrombosis After Stenting**

As previously mentioned, restenosis is the over-growth of tissue after stenting and it can be caused by an exaggerated inflammatory response. The inflammatory response can lead to the formation of neointimal hyperplasia (NH). NH is defined as an exaggerated type of healing that occurs in the lining of blood vessels[11]. NH causes an increased neointimal thickness (NT) in the blood vessel lining that can narrow the vessel and obstruct blood flow. Long-term studies indicate restenosis rates are reduced to 4-6% with DES, however, studies have shown DES are more susceptible to LST[12]. The LST has the potential to establish a blockage in the artery being treated, or a downstream vessel, and can therefore lead to a myocardial infarction and death. This increase in incidence of LST in DES has been attributed to suboptimal endothelial cell coverage[13][14]. The incidence rate of LST after DES implantation is only 0.5-2%, however, at one point it was reported that there was as high as a 50% mortality rate for patients who do experience LST[15].

### **1.4 Restenosis Causing Blood Flow Alterations**

There are several factors influencing restenosis, including local flow disturbances. These disturbances are caused, at least in part, by altered geometry within the artery (i.e. flow domain) triggered by stenting. Geometry is altered by the fact that the stent must be over-expanded relative to the native artery, as well as the geometric intricacies of the stent itself. Hemodynamic indices such as wall shear stress (WSS) and oscillatory shear index (OSI) have been correlated to NH, specifically, areas of low WSS and high OSI[16].

WSS is described as the frictional force acting tangentially from flowing fluid, in this case, blood. For simple flow, WSS can be calculated directly from the near wall velocity gradient as shown in Equation 1 where  $\tau$  is wall shear stress,  $\mu$  is dynamic viscosity,  $u$  is the velocity of the fluid close to the wall, and  $y$  is the distance from the wall.

Equation 1: Wall shear stress  $\tau = \mu * \frac{du}{dy}$

From Equation 1, one can conclude that the closer to the wall that the velocity can be determined, the more accurate the WSS calculation will be. Error related to this calculation is influenced by the technique used to obtain the near-wall velocity measurement, specifically, how close to the wall a given technique can resolve fluid velocity. Common techniques include Doppler and MRI; however, these techniques are only able to resolve velocity down to 0.9 mm resulting in a poor approximation of WSS[17]. In contrast, if one can accurately reconstruct a vessel such as a coronary artery using an imaging modality with higher resolution such as optical coherence tomography (OCT), computational fluid dynamics (CFD) can likely provide a much better estimate of WSS. The only limiting factors when calculating the distance from the artery wall with CFD is the size of the finite element mesh, and, therefore, the computational resources available to solve the governing equations of fluid flow.

### **1.5 Methods of Evaluating the Effectiveness of Stents**

In order to fully evaluate CAD and effectiveness of stents, one must be able to make measurements inside the vessel of interest. This is accomplished through medical imaging such as intravascular ultrasound (IVUS) and OCT. These imaging modalities

provide the user with the ability to determine the stent and strut placement within the vessel as well as a measurement of tissue growth over the stent struts (i.e. NT). These imaging modalities can also be used to create 3D reconstructions of the vessel for computational blood flow simulations[18][19][20][21].

### *1.5.1 Intravascular Ultrasound*

IVUS is a combination of an echocardiogram and cardiac catheterization. An ultrasound catheter tip is connected to a guidewire and navigated to the patients' coronary artery using angiography techniques. There are two types of IVUS, mechanical and solid state. Mechanical IVUS uses a mechanical transducer catheter that contains a rotating ultrasound source. The rotating ultrasound signal covers the entire vessel with no signal interference. Solid state IVUS uses phased array catheters that contain a flashing ultrasound source. With solid state IVUS, interference occurs and an area of no information is generated. The acoustic waves of a frequency usually between 20-40MHz are emitted from the catheter tip[22]. These waves, primarily, reflect off tissue and return back to the transducer as echoes or are scattered. The amount of echo returned after interacting with tissue is dependent on the tissue's acoustic impedance[23]. This information is sent from the catheter tip to an external computer that constructs a real time image of a section of the artery surrounding the catheter tip. This technique provides the clinician with an image of the inside of the vessel. IVUS has spatial resolution of 150 microns[24]. Due to the intricacies of a stented coronary artery where most stent struts (i.e. linkages) are not routinely  $\leq 100$  microns, this low resolution can lead to the loss of spatial information which can be vital when evaluating the efficiency of the stent and reconstructing the vessels[25]–[28]. However, IVUS permits plaque

characterization for complete lesion assessment using systems like that sold by Volcano and Boston Scientific[29], [30].

### *1.5.2 Optical Coherence Tomography*

OCT has shown to have a spatial resolution ten times that of IVUS as seen in Figure 2. This increased resolution provides improved detail in stented coronary arteries needed for an accurate reconstruction and analysis of hemodynamic indices from computational modeling results (i.e. WSS and OSI)[24], [31], [32]. OCT is similar to ultrasound; however, instead of emitting sound waves, OCT emits near-infrared light into the vessel. There are two types of OCT, time-domain (TD-OCT) and frequency-domain (FD-OCT). This study used FD-OCT as it provides improved resolution and acquisition speed as well as more accurate segmentation of the lumen and stent boundaries used during the CFD modeling process. The optical diode used in FD-OCT is attached to the end of a guide catheter and emits a low coherence near-infrared light beam directed toward the target tissue. The magnitude and location of the backscattered light from the tissue is interpreted to create an image. This backscattered signal is detected in the frequency domain. Because the signal is in the frequency domain, the acquisition time is decreased compared to TD-OCT. Frequency information is acquired with a broadband light source, charge-coupled device camera, and a spectrometer[33]. The broadband light source improves the axial resolution compared to TD-OCT; however, there is also a significant signal drop-off with depth[33]. While OCT allows for an assessment of coronary disease and the ability to see strut apposition against the vessel wall, the practice remains scarce in a clinical setting.

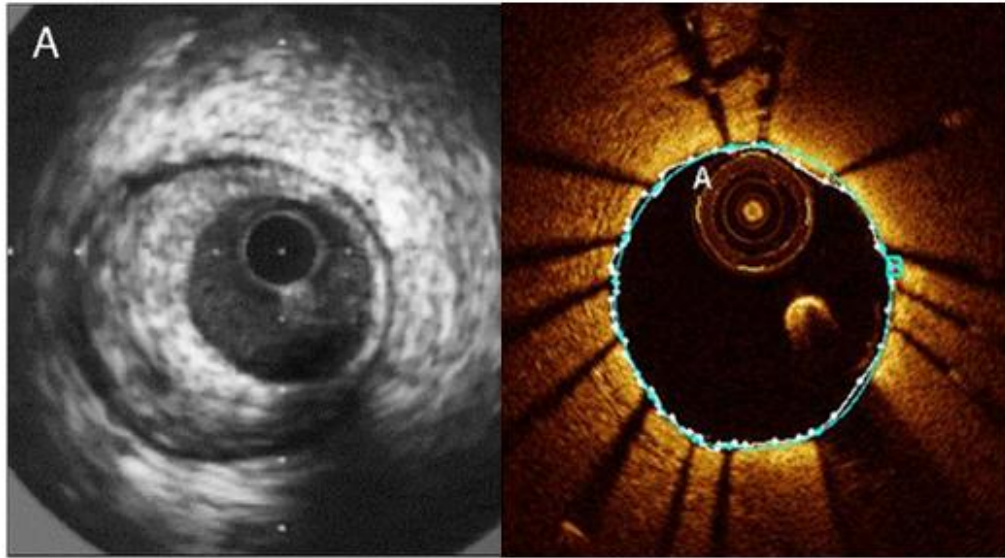


Figure 2: OCT (right) has ten times the spatial resolution compared to IVUS (left). IVUS image obtained from Nissen; *Journal of the American Heart Association* 2001.

## 1.6 CFD as a Tool for Modeling Blood Flow

CFD is an advanced simulation tool commonly used in fluid mechanics to solve the governing equations of fluid flow using numerical methods and algorithms. CFD is a useful method for analyzing the effect of stents in coronary arteries given that complex engineering metrics such as local velocity distributions are difficult to obtain in vivo. Using CFD, one can quantify key indices of NT and hemodynamic consequences of stenting including WSS and OSI[16], [19]–[21], [34].

From the simulation results, time-averaged WSS ( $\tau_{mean}$ ) is determined as follows. Total stress on the vessel wall (Equation 2),  $\sigma$ , is the sum of pressure and viscous forces as seen below where  $p$  is pressure,  $I$  is the 3x3 identity matrix,  $\mu$  is viscosity, and  $\nabla u$  is the velocity gradient.

Equation 2: Total stress on the wall 
$$\sigma = pI + \mu(\nabla u + \nabla u^T)$$

A normal vector (Equation 3),  $n_s$ , is defined for each point on the luminal surface. The traction vector,  $t$ , is the product of the total stress on the wall ( $\sigma$ ) and the normal vector ( $n_s$ ) as seen below.

Equation 3: Traction vector 
$$t = \sigma + n_s$$

Subtracting the normal component of traction isolates the surface vector of traction ( $t_s$ ) as seen below in Equation 4.

Equation 4: Surface vector of traction 
$$t_s = t - (t * n_s) * n_s$$

$\tau_{mean}$  (Equation 5) is defined as the magnitude of the time-averaged surface vector of traction  $t_s$  as seen below where  $T$  is the period of the cardiac cycle[35].

Equation 5: Time-averaged WSS 
$$\tau_{mean} = \frac{1}{T} \int_0^T t_s dt$$

As previously mentioned, OSI has also been correlated to NH. OSI is a measure of directionality of WSS. Lower OSI values indicate WSS is oriented predominately in the primary direction of blood flow while a value of 0.5 is indicative of bi-directional WSS with a time-average value of zero over the cardiac cycle. OSI is computed as seen in Equation 6[35].

Equation 6: Oscillatory shear index 
$$OSI = \frac{1}{2} \left( 1 - \frac{\left| \frac{1}{T} \int_0^T t_s dt \right|}{\frac{1}{T} \int_0^T |t_s| dt} \right)$$

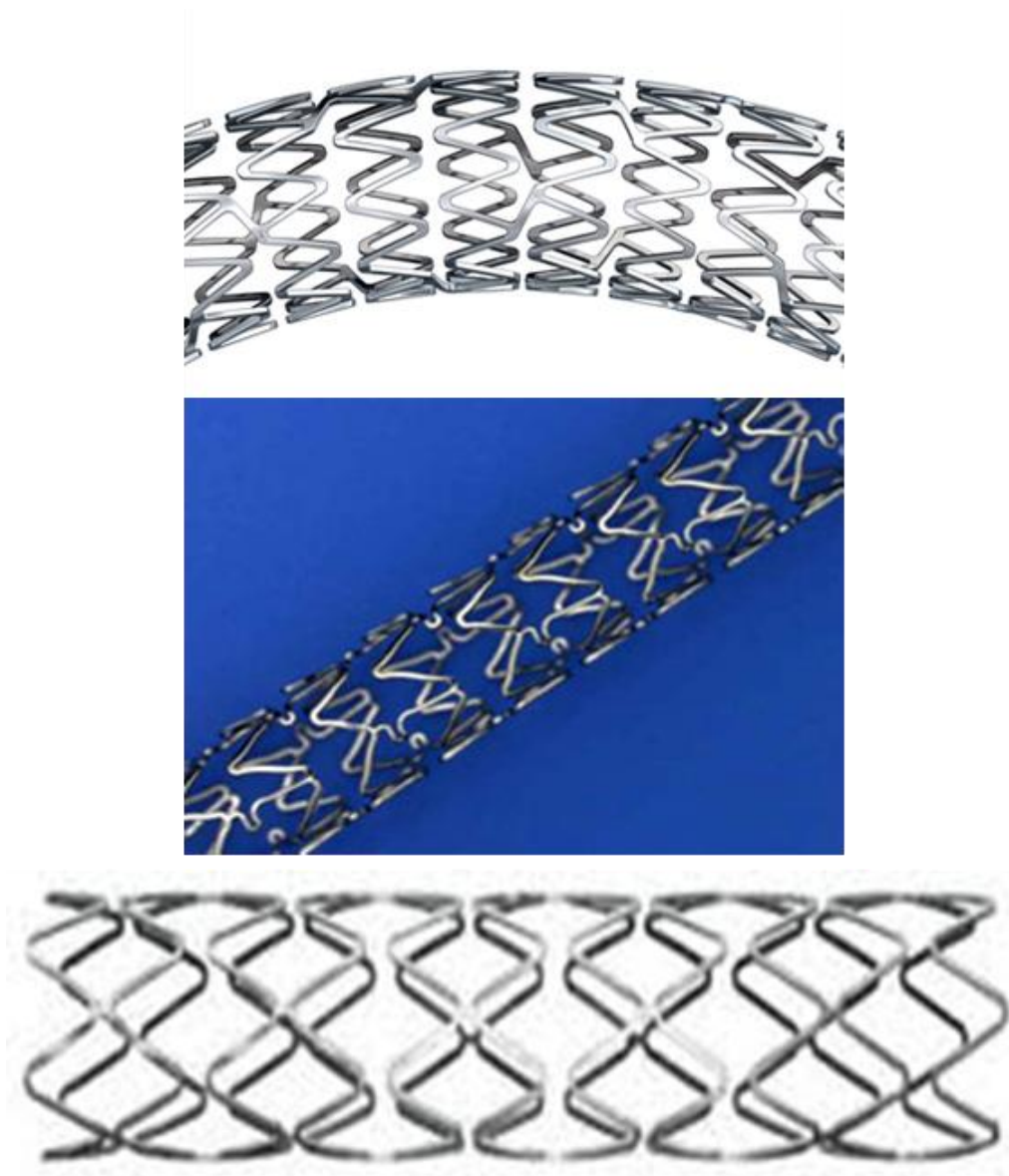
## 1.7 Objective and Specific Aims

There is limited data on the correlation between WSS distributions and NT for current generation DES. Gaining a better understanding of the relationship between



adverse WSS distributions and NT for current generation DES has the potential to reduce the number of revascularization procedures and, in turn, reduce healthcare costs.

The objective of this thesis was to evaluate the effects of three different stents implanted into coronary arteries on WSS and NT. Specifically, this study will investigate the effects of the Nobori (Temuro), Promus Element (Boston Scientific), and Xience Prime (Abbott Vascular) stents as seen in Figure 3 via their WSS distributions immediately (post-stenting) and 9 months after stent implantation (follow-up) relative to their respective NT that develops. The objective will be completed using three aims introduced and discussed beginning in section 1.7.1.



*Figure 3: Promus element stent- Boston Scientific (top, multivu.com). Xience prime stent- Abbott Vascular (middle, fda.gov). Nobori stent- Terumo (bottom, terumo-europe.com).*

The Nobori, Promus Element, and Xience Prime are current generation DES and their respective specifications including strut thickness, width, angle relative to flow, and drug-elution characteristics can be found in Table 1. As the Table 1 illustrates, the Nobori stent is thicker compared to the Promus Element and Xience Prime stents. Also, stent geometry is the only differing aspect between the Promus Element and Xience Prime

stents as the elution agent and coating are equivalent. Outcomes of this study will improve the understanding of how different stent designs affect NT relative to the respective anti-proliferative drugs for each DES.

	<b>Nobori</b>	<b>Promus Element</b>	<b>Xience Prime</b>
<b>Strut Thickness (mm)</b>	0.135	0.08	0.08
<b>Strut Width (mm)</b>	0.15	0.086	0.09
<b>Angle Relative to Flow (deg)</b>	50.4	52.3	45.7
<b>Elution Agent</b>	Biolimus A9	Everolimus	Everolimus
<b>Total Drug Dose (<math>\mu\text{g}/\text{mm}^2</math>)</b>	6.9	1.2	0.85
<b>Release – 4 or 12<sup>†</sup> weeks</b>	45% <sup>†</sup>	80%	80%
<b>Plasma Concentration (ng/mL)</b>	0.09	0.33-0.5	0.33-0.5
<b>Diffusion Coefficient</b>	0.1005	0.1014	0.1014
<b>Polymer</b>	PLA Bioabsorbable	PMBA+PVDF-HFP Durable	PMBA+PVDF-HFP Durable
<b>Coated Area</b>	Abluminal	Abluminal and Luminal	Abluminal and Luminal

*Table 1: Nobori, Promus Element, and Xience Prime stent specifications[36]. PMBA: poly-n-butyl methacrylate; PVDF-HFP: vinylidene fluoride and hexafluoroisopropylene; PLA: poly-lactic acid.*

### *1.7.1 Aim 1: Confirm Previous Studies Relating Low WSS and Stent Geometry*

The first aim of this study is to use patient-specific models to confirm previous idealized studies regarding stent design characteristics and their effect on adverse WSS distributions. Stent geometry has been shown to affect the distribution of WSS, and, in turn, affect NT[16]. Gundert et al created a hierarchy of factors that can result in adverse WSS distributions by virtually implanting various stents into idealized coronary arteries[34]. The hierarchy includes strut thickness, stent-to-lumen area ratio, angle of struts relative to the primary direction of blood flow, and the arrangement of connector elements[37]. To accomplish aim 1, stents are virtually implanted into patient-specific reconstructions of coronary arteries based on OCT images. CFD simulations are performed and areas of low WSS determined.

### *1.7.2 Aim 2: Comparison Between Post-Stent and Follow-up Low Normalized WSS*

The second aim of this study is to compare post-stent normalized low WSS with follow-up normalized low WSS. During the follow-up period, tissue grows atop and around the stent struts. In theory, this tissue growth should return the WSS closer to the artery's native value, thereby decreasing the consequences of adverse WSS distributions. Reconstructions of coronary vessels in aim 2 are created at post-stenting and follow-up. This aim provides analysis of how well the different stent struts are apposed in the vessel 9 months after stent implantation. A stent strut is considered malapposed if it is not flush against the arterial wall[38]. Also, results from this aim provide overall insight on tissue growth within the stented region with respect to different stent geometries and elution

agents. We hypothesize that the thick strutted Nobori will yield greater NT compared to the thinner strutted Promus Element and Xience Prime.

### *1.7.3 Aim 3: Evaluate Post-Stent WSS and Follow-up NT*

The third and final aim of this study is to evaluate post-stent WSS and follow-up NT. Adverse distributions of WSS caused by stenting can cause increased NT leading to restenosis. There have been only a few small studies correlating WSS distributions to NT for first generation DES, which collectively yielded conflicting results[39]–[41]. OCT images offer the capability to quantify the arterial response (i.e. vessel damage and NT) within the stented region and hypothesize associations between WSS post-stenting and follow-up NT. This approach will help predict how different current generation DES impact NT.

## Chapter 2

---

### Methods

#### 2.1 Data Acquisition

Computed tomography angiography (CTA) and OCT imaging were performed immediately after stenting, as well as at 9 months follow-up. CTA is a noninvasive procedure that enables visualization of the region available to blood flow within coronary arteries. The acquisition of this data was completed by Dr. Hiromasa Otake and his team at Kobe University Graduate School of Medicine in Kobe, Japan. This study was approved by the ethical committee of Kobe University and Institutional Review Board at Marquette University. CTA was performed using a 320-detector row CTA (Toshiba Aquilion One™, Otawara, Japan) in accordance with guidelines set by the Society of Cardiovascular Computed Tomography[42]. An intravenous bolus (30-90 ml) of contrast agent was injected at a flow rate of 0.07 ml/kg/s. The tube current time product was 300-400 mAs and a tube voltage of 100 or 120 kVp. Scans were performed using ECG-based tube current modulation or sequential image acquisition. Transaxial images were reconstructed with 0.75 millimeter slice thickness and 0.3 millimeter slice increment using a medium-smooth convolution kernel. Coronary angiography data was visualized using Volview (Kitware, Clifton, NY). Volview is an open-source volume visualization system designed for examination of medical data in a research setting. Volview has the capability to load a wide range of file formats and generate high-quality 3D renderings.

Specifically, this study used Volview to isolate the stented artery and create 3D volumes from the CTA data.

## **2.2 Patient-Specific Vessel Reconstruction**

Vessel reconstruction was divided into five steps of image processing, wire pathway reconstruction, segment registration, model assembly, and stent implantation. This patient-specific reconstruction process was created and validated by Ellwein et al[21]. Each of these steps is reviewed below. Additional details and methods developed for the current work are highlighted.

### *2.2.1 Image Processing*

OCT images were processed using Matlab (MathWorks; Natic, MA). Lumen and stent contours of the OCT images were first isolated and converted to grayscale. The headers, footers, and other markings were then masked and a binary image of the contours was created. The binary images were scaled with a calibration value found using ImageJ ([www.imagej.net](http://www.imagej.net)). In ImageJ, a line of a known length was placed along the scale provided on the OCT image. Using ImageJ's 'Set Scale' feature, the length in pixels of the line, and, in turn, the number of millimeters per pixel for the image were determined. The pixels of the binary image were then converted to Cartesian coordinates with the z-coordinate for each image segment representing its pullback distance. This process can be seen in Figure 4. Finally, the segments were aligned vertically in succession resulting in a stack of OCT segments positioned with the z-axis intersecting each segment at its centroid.

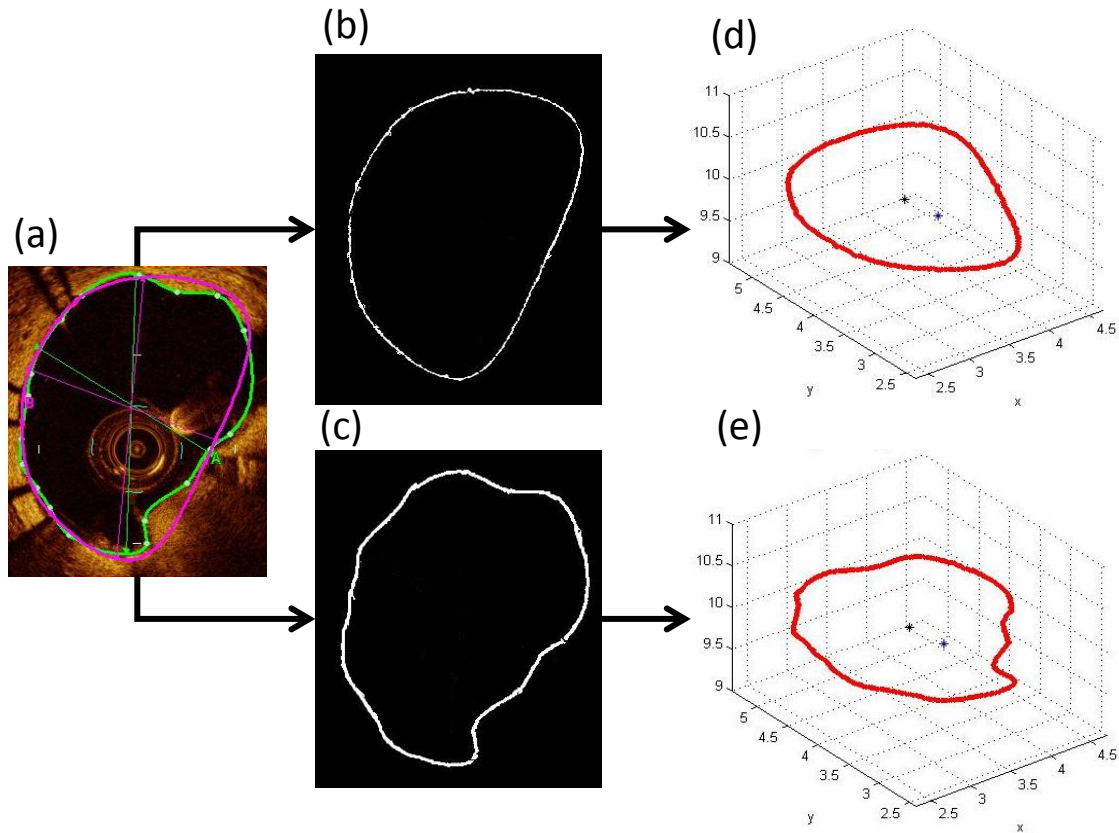


Figure 4: a) OCT image with lumen (green) and stent (purple) contours. b) and c) Stent and lumen contours, respectively, isolated from RGB image using thresholding previously described by Ellwein et al in CVET 2011. d) and e) Pixel locations for stent and lumen contours, respectively. (Blue point = OCT image center, black dot = contour center).

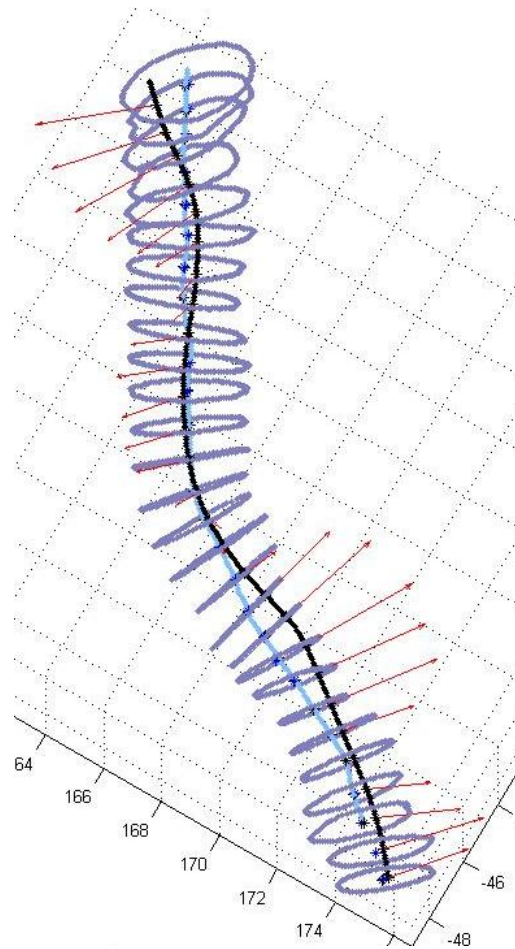
### 2.2.2 Wire Pathway Reconstruction

During OCT data acquisition, the images are obtained orthogonal to the photodetector at the tip of the imaging wire and do not necessarily lie on the vessel centerline, or orthogonal to it. Consequently, the wire pullback pathway must be determined to ensure precise segment registration. The wire pathway with minimum bending energy was determined by applying a shortest path algorithm to a graph representation of the artery as previously described in detail by Ellwein et al[21].

### 2.2.3 Segment Registration



Segments from the OCT images were registered on the reconstructed wire pathway according to known vessel landmarks from CTA such as the edge of the stent or a bifurcation, where available. The remaining segments were positioned longitudinally according to OCT image spacing. Finally, segments were oriented orthogonal to the wire pathway and rotated such that their centroids were aligned with a vessel centerline generated from the CTA data using the open-source software packages ITK-Snap ([www.itksnap.org](http://www.itksnap.org)) and VMTK ([www.vmtk.org](http://www.vmtk.org)) as seen in Figure 5. 3D segmentation in ITK-Snap was performed using intensity regions with a lower threshold of 175 and no upper threshold, and a snake propagation of 25 iterations, as previously done by Antiga et al[43]. This lower threshold coupled with the CTA intensity was determined by comparing the segments generated from the CTA and OCT data. The area of the segment from CTA and its corresponding OCT image were compared using the ‘group\_calcAreas’ function in Simvascular (<https://simtk.org/home/simvascular>). If these areas did not match, the threshold and CTA intensity were adjusted accordingly. This process was completed on a patient to patient basis.

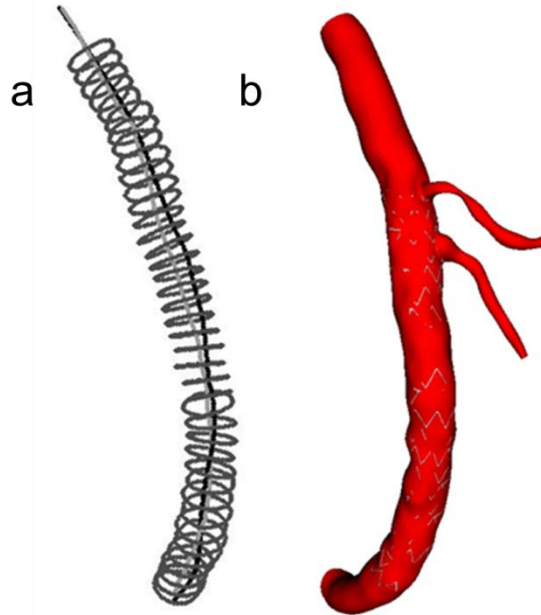


*Figure 5: Segments registered on the wire pathway (black line) according to vessel landmarks where possible. Remaining segments are then oriented to wire pathway and rotated such that segment centroids align with the vessel centerline (blue line). Vector from the image centroid to the upper-left hand corner was also tracked and plotted (red).*

#### 2.2.4 Model Assembly

OCT segments from the stented region were coupled with CTA segments from the distal and proximal regions of the stent to form the entire vessel. CTA segments of branches within or near the stented region were created and added to the vessel as well since OCT was not conducted for these side branches. 3D representations of the proximal and distal regions to the stent were created using ITK-Snap and VMTK. These regions were queried using customized Matlab scripts to create orthogonal segments defining the vessel lumen. The same Matlab scripts were used to create segments that

defined the branches. The segments from CTA as well as OCT were imported into the open-source software Simvascular. The total group of segments was then lofted and blended to form a Parasolid model (Siemens, Plano, TX) of the entire flow domain as seen in Figure 6. The follow-up model was constructed using the same process described above except with lumen segments from the follow-up OCT images.

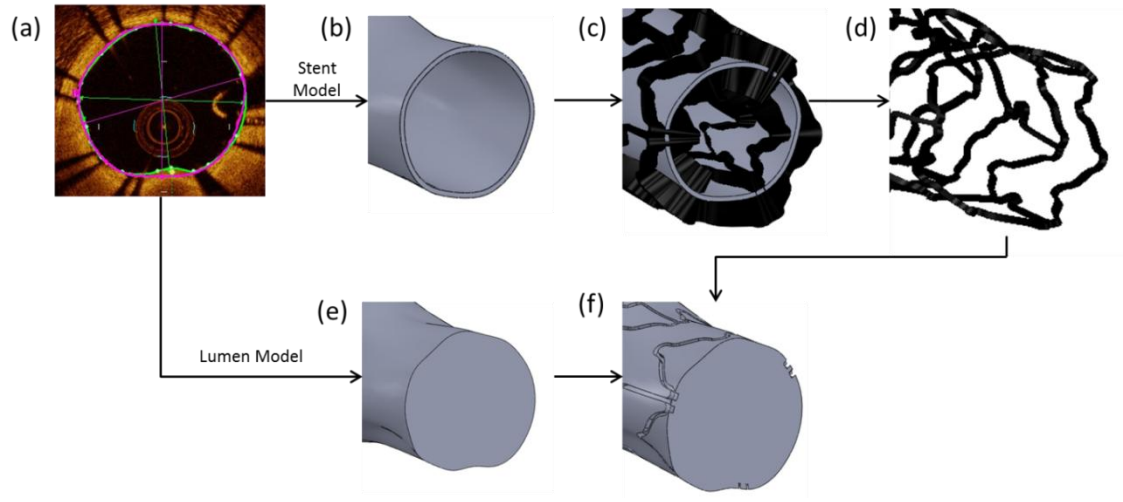


*Figure 6: Combined segments from CT and OCT (a) are lofted along with the branch segments to form a Parasolid model (b).*

### **2.3 Computational Stent Implantation**

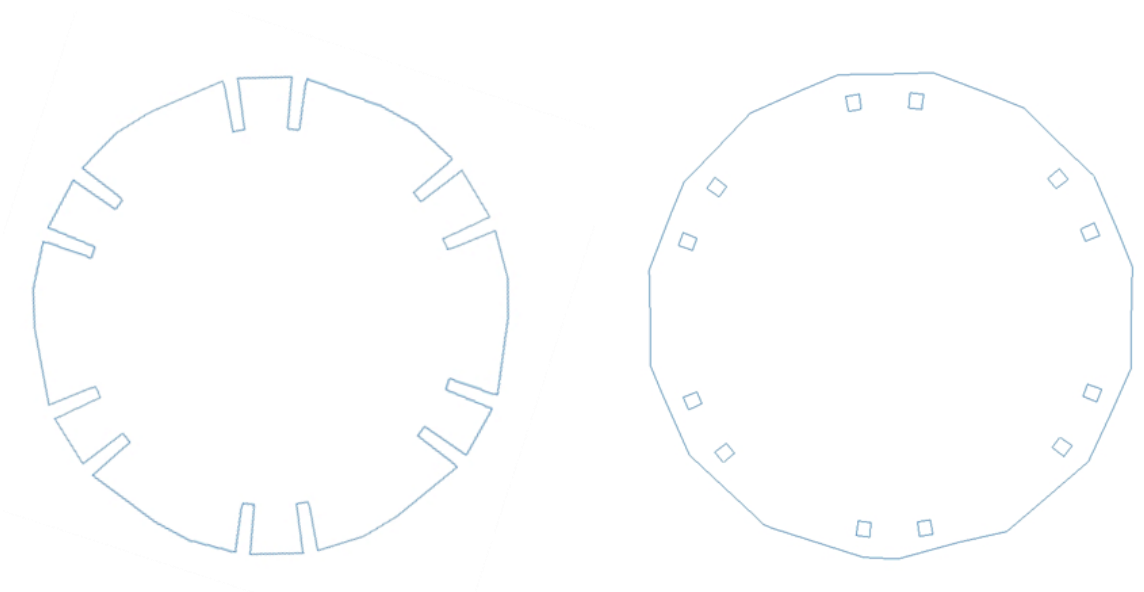
A series of Boolean operations was used to virtually implant the DES into the patient-specific vessels similar to those previously described by Gundert et al[44] (Figure 7). First, a thick version of either the Nobori, Promus Element, or Xience Prime stent was created using SolidWorks (Solidworks Corp., Concord, MA). The length of the stent was adjusted in accordance to the stent implanted in each patient. Next, the stent contours from OCT images were used to create a model and shell with a thickness equal

to that of the specific stent used in the case. This shell was then intersected with a thick version of the stent to create a patient-specific stent model. Finally, this patient-specific stent model was subtracted from the lumen model to generate a computational representation of the blood flow domain.



*Figure 7: Method of virtual stent implantation. Solid models of the outer surface of the stent and vessel lumen (e) were lofted from the purple and green contours of the OCT images (a). The stent model was used to create a shell with the thickness equal to that of the stent (b). The shell was intersected with the thick stent model (c) to create a patient-specific stent model (d). Subtracting the patient-specific stent model (d) from the lumen model (e) generated a computational representation of the blood flow domain (f).*

While this method is based off of the similar process created by Gundert et al[44], the previous process did not account for malapposed struts within the lumen, thereby leading to thickened representations of struts to an unrealistic dimension that could create erroneous changes in local artery and stent morphology when used for subsequent CFD simulations. Accounting for malapposed struts was a novel aspect of this study. The difference between the two methods can be seen in Figure 8.



*Figure 8: Model produced from Gundert et al that does not account for malapposed struts (left). Model produced from current method that can create malapposed struts (right).*

## **2.4 Steps Performed to Assure Accuracy During Vessel Reconstruction**

In order to assure that the vessel reconstruction and stent implantation processes were performed accurately, a series of checks were performed throughout the entire process as shown in Figure 9.

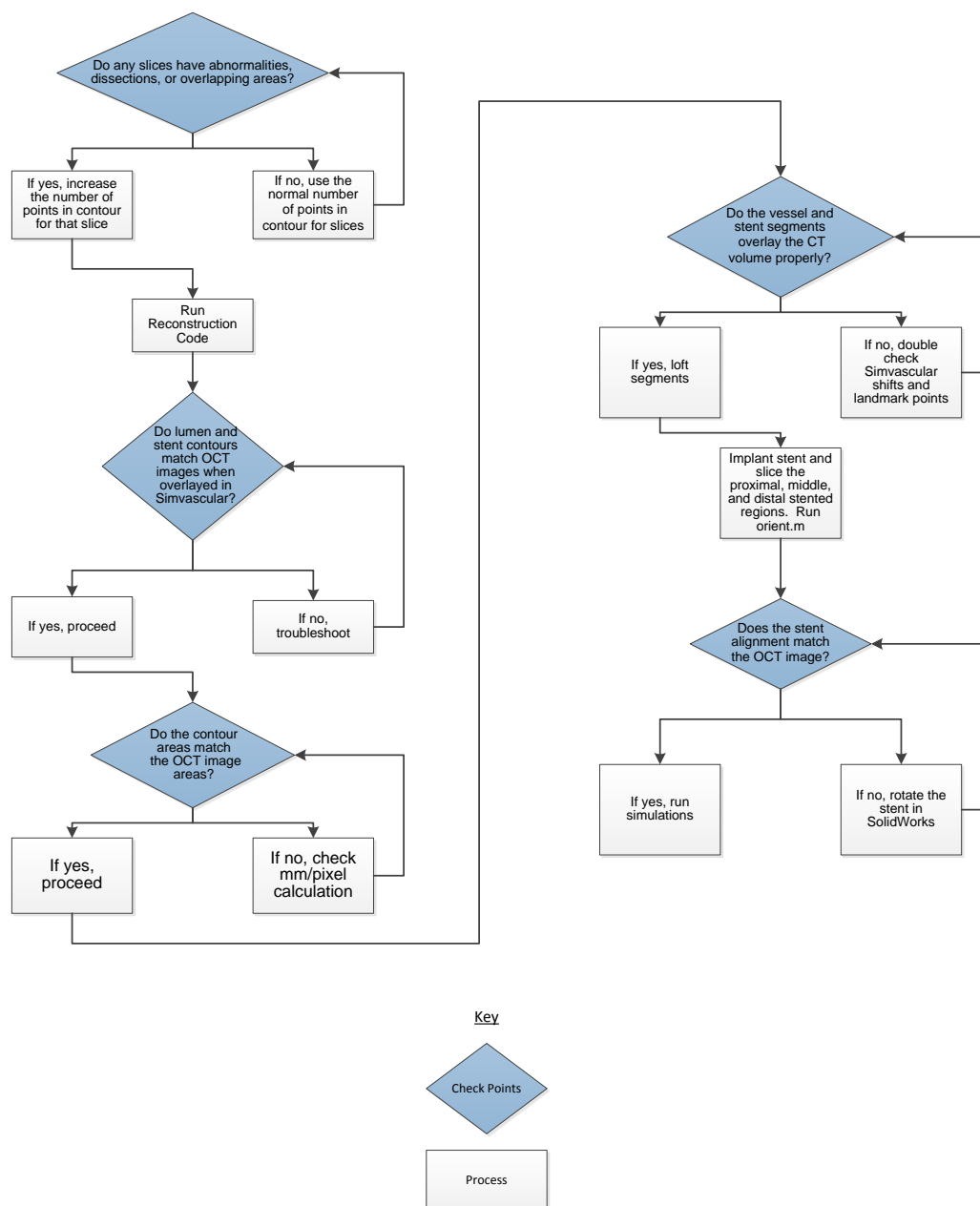
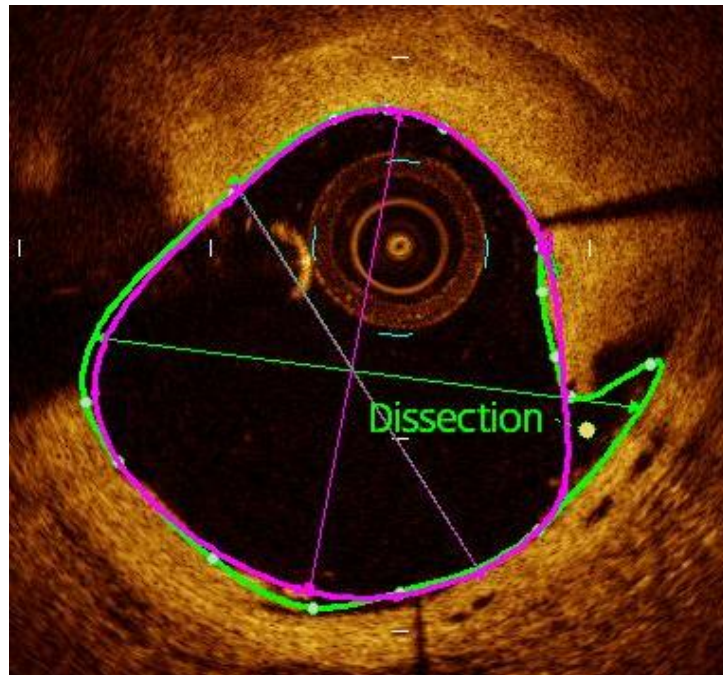


Figure 9: Processes for assuring accuracy while creating patient-specific coronary models.

First, the OCT images were analyzed by visual inspection to determine if there were any images with contours containing abnormalities (e.g. dissections, protrusions and overlapping edges). Such abnormalities, as depicted in Figure 10, can create inaccurate segments and cause interpolation errors when lofting the segments. To prevent errors

while still maintaining the correct contours, the number of points used to create the segment is increased in images with such abnormalities.



*Figure 10: Abnormality (i.e. dissection) in the lumen contour that requires an increase in segment points.*

Next, the lumen contour segments were overlapped with their respective stent contour segments in Simvascular to determine if they were in the correct orientation. This assured that the correct path and rotation was used to align the stent contours. Then, also in Simvascular, the areas of the segments were determined and compared to the areas of the contours on their respective OCT image. This step confirms that the millimeters per pixel calculation determined using ImageJ was correct. Next, the final combination of OCT and CTA segments were superimposed on the entire CTA volume in Simvascular. This step assures that the landmarks used to determine the transducer path were correct. Also, Simvascular uses a coordinate system with an image origin at

(0,0,0); however ITK-Snap and VMTK use the NIFTI coordinate system, and the centerline generated from these programs will also be in this coordinate system.

Therefore, the coordinate shifts provided in Equation 7 were applied to convert between NIFTI and Simvascular coordinates where  $(X_{sp}, Y_{sp}, Z_{sp})$  are the spacings in the X, Y, and Z directions,  $(X_0, Y_0, Z_0)$  are the coordinates of the Image Position (Patient) field (0020,0032) of the most superior image, and  $N_{sl}$  is the number of slices in the data set. These shifts are assuming that VolView places the image origin at (-0.125,-0.125,-0.125) and images are 512x512. If these shifts are performed properly, the segments will line up with the stented vessel in Simvascular.

$$X - shift = (-0.125 + 511 * X_{sp}) - (-X_0)$$

$$Y - shift = (-0.125 + 511 * Y_{sp}) - (-Y_0)$$

$$Z - shift = (-0.125 + (N_{sl} - 1) * Z_{sp}) - (-Z_0)$$

Equation 7: Conversion between NIFTI and Simvascular coordinates

Finally, using a novel technique, it must be assured that the stent is accurately placed circumferentially within the vessel model. To do this, an initial model of the stented vessel is created using the steps mentioned above, and quickly evaluated without running a CFD simulation. Instead, a vtk model of the stented flow domain is loaded into Paraview (Los Alamos National Laboratory, [www.paraview.org](http://www.paraview.org)), and three slices are made, one each in the proximal, distal, and middle regions of the stent. The slice locations are taken from the lumen OCT segments used by Simvascular in the model creation process. Using a custom Matlab program, the struts in the slices are compared to



the strut shadows produced in the analogous OCT images and a degree of rotation is calculated. The three degrees of rotation are averaged and the stent is then rotated accordingly in Solidworks. The Boolean operations performed for virtual stent implantation are then conducted again, if needed, using the rotated version of the stent (Figure 11).

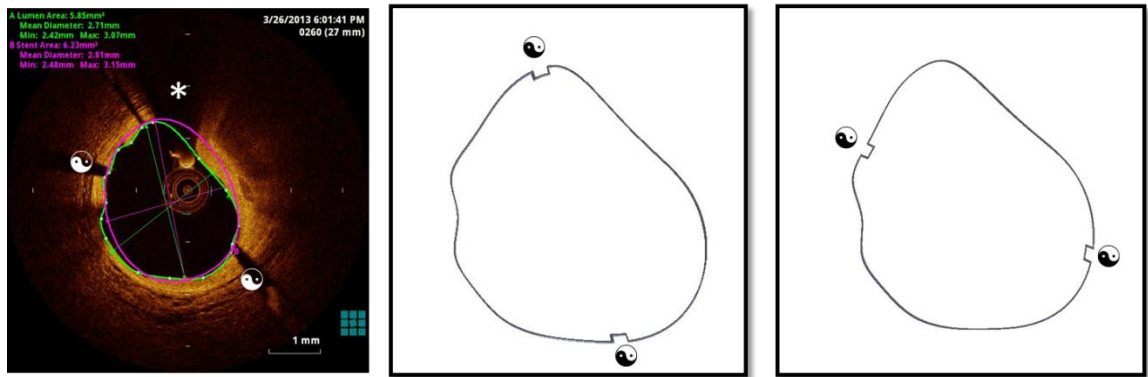


Figure 11: OCT image (left). Slice from initial virtual stent implantation with struts not matching OCT image (middle). Slice after applying a specific rotation to the stent in Solidworks to better match the OCT image (right). \* = guidewire artifact. ● = stent strut.

## 2.5 Specification of CFD Boundaries Conditions and Simulation Parameters

Post-stent and follow-up models were subjected to a canine pulsatile blood flow waveform acquired from the left anterior descending coronary artery[45]. This blood flow waveform is associated with Reynolds and Womersley numbers which made it applicable in many previous computational studies[46]–[49]. The mean blood flow through the stented artery was determined using cardiac output and assuming the coronary arteries received 5% of the cardiac output, of which the right and left coronary arteries received 16% and 84%, respectively[21], [50]. For patients whose cardiac output was not obtained, cardiac output and mean blood flow through the stented artery was determined using cardiac index and body surface area. The flow waveform was then

scaled to match the mean blood flow of the specific vessel and introduced at the model inflow face as a time-varying Womersley velocity profile. For all simulations, blood was assumed to be a Newtonian fluid with a viscosity and constant density of 4 cP and 1.06 g/cm<sup>3</sup>, respectively.

The flow split between the main vessel and subsequent branches was calculated assuming shear stress autoregulation (i.e. Murray's Law). Murray's Law states that when a parent vessel branches into daughter vessels, the cube of the diameter of the parent vessel is equal to the sum of cubes of the diameters of the daughter vessels[2]. This represents an ideal branching pattern that optimizes energy and metabolic need, and appears to be mediated by variations in artery caliber induced by WSS. Therefore, WSS was assumed to be equal in the main vessel and branch vessels as shown in previous studies by Williams et al[2], [49]. Assuming blood flow is fully developed, and has a constant velocity profile, WSS can be estimated by Equation 8 where  $\tau$  is WSS,  $\mu$  is viscosity,  $Q$  is average flow, and  $r$  is the lumen diameter.

Equation 8: Estimation of wall shear stress 
$$\tau = \frac{4\mu Q}{\pi r^3}$$

As previously stated, WSS for the main vessel and branch vessel are set equal to obtain the flow distributions to each coronary artery branch.

A three-element Windkessel representation was introduced on the outlets of the models in order to replicate the physiological influence of the arterial tree distal to the branch being examined. The three-element Windkessel model can be described by three main parameters  $R_c$ ,  $C$ , and  $R_d$ [2].  $R_c$  is the characteristic impedance representing the resistance, compliance, and inertance of the proximal artery of interest,  $C$  is the arterial

capacitance and accounts for the sum of the compliance of arteries beyond the model outlets, and  $R_d$  is the distal resistance in the absence of ventricular contraction[49]. Together,  $R_c$ ,  $R_d$ , and the time-varying resistance to blood flow resulting from ventricular contraction can be calculated as the ratio of mean blood pressure and mean blood flow. In the absence of ventricular contraction using the impulse response method demonstrated by Van Huis et al.,  $R_c$  and  $R_d$  constitute the zero hertz impedance ( $Z_0$ ).  $Z_0$  is between 22%-65% less than the total resistance value[51]. Therefore, the mean blood pressure and mean flow for each patient was scaled by 65% for the data to be constrained within the range presented by Van Huis et al.  $R_c$  is described by the average impedance of frequencies above 7Hz and can be calculated by Equation 9 where  $C_{ph}$  is the wave speed,  $\rho$  is the blood density, and  $r$  is the vessel radius[51].

$$R_c = \frac{C_{ph}\rho}{\pi r^2}$$

Equation 9: Characteristic impedance reflective of average impedance of frequencies above 7 Hz

A wave speed of 6.7 or 8.6 m/s was applied to represent either a left circumflex or left anterior descending canine coronary artery, respectively[52][49].  $R_c$  was calculated for each outlet branch and  $R_d$  was calculated as the difference between  $Z_0$  and  $R_c$ .

Capacitance at each outlet was calculated using a Matlab program that determines pulse blood pressure based on an inflow waveform, the calculated  $R_c$  and  $R_d$  values and an initial estimate for C. Specifically, in the frequency domain, the Fourier transform of the flow waveform was multiplied by impedance ( $Z$ ) which is calculated as seen in Equation 10  $f$  is the frequency, and C is the estimate of capacitance[53].

$$Z = Rc + 1/\left[\left(\frac{1}{Rd}\right) + i * 2 * \pi * f * C\right]$$

Equation 10: Impedance in the frequency domain

The maximum (systolic), minimum (diastolic), and difference between the maximum and minimum (pulse pressure) is compared to the desired blood pressure values. The capacitance value is adjusted knowing that lower compliance yields larger pulse pressures and vice versa[54]. This method is further illustrated in Figure 12.

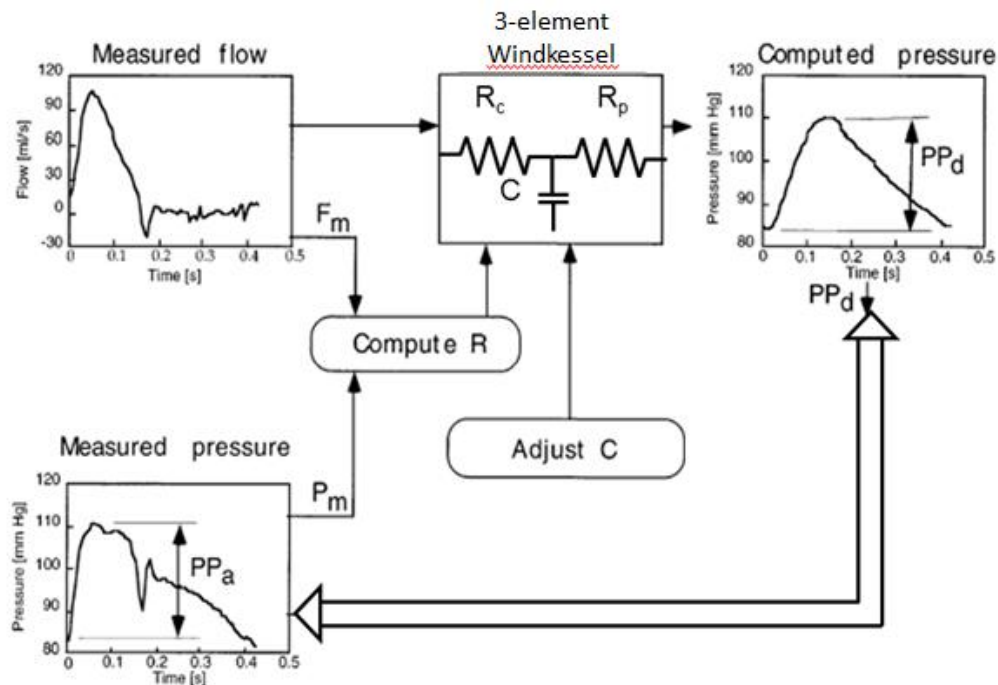


Figure 12: Using flow waveform, blood pressure, impedance spectra, and RCR parameters to replicate physiologic behavior ( $F_m$ =mean flow,  $P_m$ =mean pressure,  $R_c$ =characteristic impedance,  $R_d$ =distal resistance,  $C$ =capacitance,  $PP_d$ =pulse pressure predicted by model,  $PP_a$ =pulse pressure method). Image obtained from Westerhof, American Phys. Society, 1999.

## 2.6 Anisotropic Meshing of Patient-Specific Models

For each post-stent and follow-up model, an anisotropic mesh with unstructured tetrahedral elements was created using an automated mesh generation program (Simmetrix, Clifton Park, NY). A custom meshing macro allowed for different maximum element edge sizes on different faces. This feature was used to place more elements where they were most needed within the flow domain (i.e. the stent struts) and fewer elements where a coarse density was sufficient (i.e. the intrastrut regions and proximal and distal to the stent).

Mesh element sizes were determined based on the strut width of the specific stent that was implanted. The minimum element size at the stent face was set to  $\frac{1}{4}$  the strut width. This assured at least four elements across the width of the stent. Previous studies indicated that CFD results of the stented vessel model were independent of the mesh density using the aforementioned mesh parameter[37].

Simulations were performed using a stabilized finite element method to solve equations for conservation of mass (continuity) and balance of fluid momentum (Navier-Stokes). Four cardiac cycles were performed for each simulation to ensure convergence with a maximum difference in blood pressure and flow between equivalent time points in successive cardiac cycles of less than 1 mmHg and  $1 \text{ mm}^3/\text{s}$  units, respectively.

## 2.7 Data Normalization

Each patient has a different flow rate to the artery as a result of its estimation from anthropometric data, which may or may not be a true measure of coronary artery blood

flow. This results in different values of WSS proximal to the stented region for each patient (Figure 13).

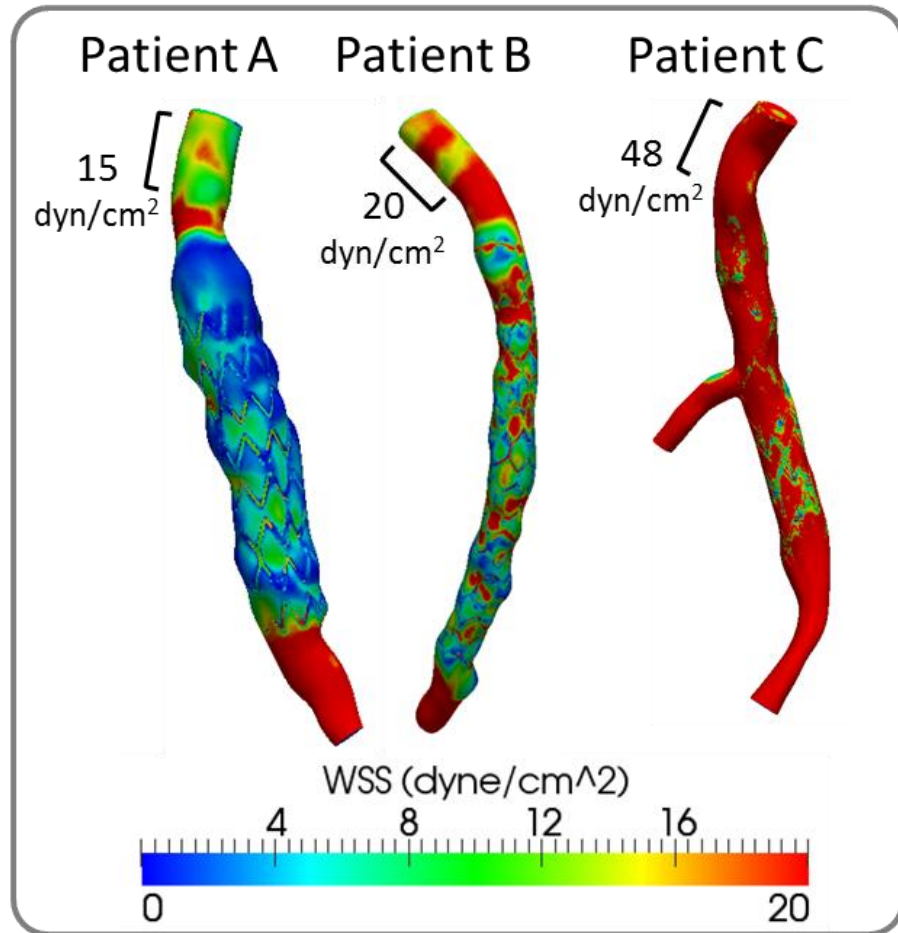


Figure 13: Different values of WSS proximal to the stented region for three different patients.

To account for these differences, we facilitate individual and group comparisons by normalizing (i.e. dividing) all WSS values for a given patient by an average WSS value from upstream of the stent where it is assumed the vessel is closer to its native diameter. This makes the range of WSS values between 0 and 1. This process generated a normalized low WSS threshold of 0.3 based on previous studies indicating WSS less than 4 dynes/cm<sup>2</sup> is an index of restenosis[21]:[55], and a prior study relating NH to

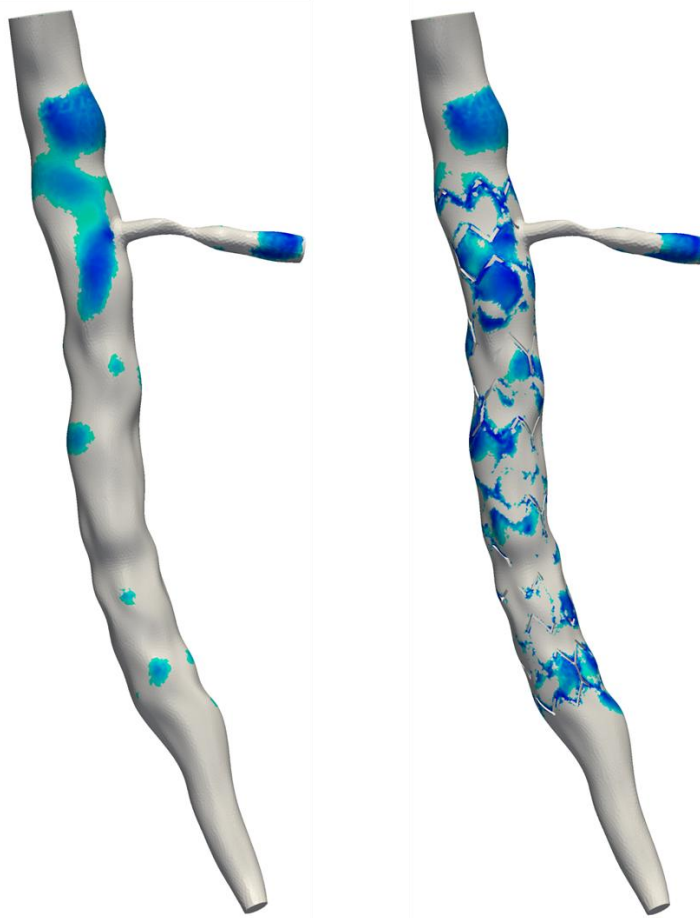
normalized WSS values after in rabbit iliac arteries[16]. While normalization can be completed based off a number of indices including flow, normalizing to WSS provides a universal threshold and range of values. Also, as previously mentioned, indices such as flow are determined based on a number of assumptions. Normalizing based on such values can provide a misrepresentation of WSS values.

## **2.8 Data Quantification Points**

As conducted in previous studies, time-averaged WSS and OSI were calculated and visualized over the last cardiac cycle for every post-stent and follow-up model.

### *2.8.1 Regional Quantification*

The percentage of the post-stent and follow-up vessel surface exposed to time-averaged WSS below 0.3 as well as  $OSI > 0.1$ [21], [56] was used to quantify the impact of the implanted stent. Further quantification metrics include stent-induced area of low WSS, area of low WSS per stent length, and stent-to-vessel area ratio. To calculate the stent-induced area of low WSS, simulations and normalized WSS procedures were performed on un-stented arteries created from post-stenting OCT data, but before performing the Boolean stent implantation procedure, and subtracted from the stented vessel. This eliminates the normalized low WSS areas that are caused by vessel geometry, rather than that of the implantation of the stent (Figure 14).



*Figure 14: Low normalized WSS distributions produced by the vessel (left) compared to distributions produced by the vessel and stent geometry (right).*

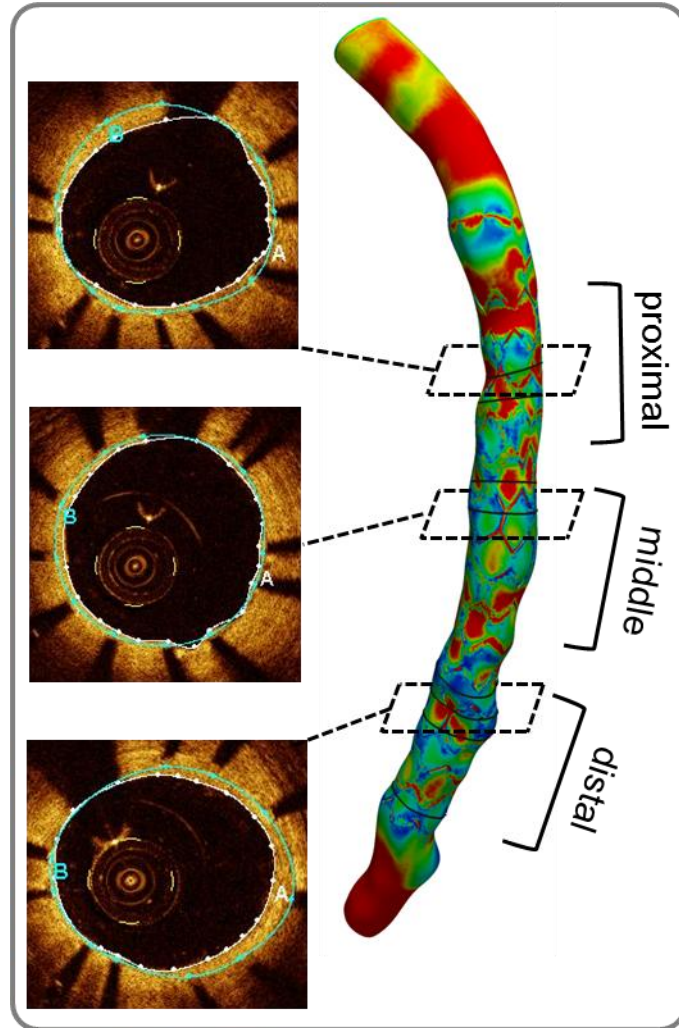
The area of low WSS per stent length further normalizes the cases to account for differences in the length of stents used in each patient. The stent-to-vessel area ratio represents the area of exposed stent to the area of the lumen within the flow domain where the stent was deployed.



### 2.8.2 *Local Quantification*

Total NT at follow-up was quantified in Solidworks. This was completed by subtracting the follow-up model volume from the post-stenting model volume. This provides a measure of total tissue growth in the stented region.

NT was measured from the follow-up OCT images by subtracting the lumen contour from the stent contour at equivalent circumferential locations relative to the image centroid. This NT measurement was correlated with normalized time-averaged WSS results obtained from the respective post-stent model along planes equivalent to those at which the follow-up OCT images were acquired. This correlation was completed at locations within 5 millimeter regions of the proximal, middle, and distal portions of the stent (Figure 15). Locations within these regions had consistent scaffolding for each stent (i.e. maximum number of struts circumferentially) since prior studies have indicated differences in scaffolding can also influence the severity of NT. It was concluded that there were not enough areas of  $OSI > 0.1$  at post-stenting to perform the correlation with NT at follow-up.



*Figure 15: Proximal, middle, and distal regions with maximum scaffolding that were isolated in an effort to correlate post-stenting WSS and follow-up NT.*

A process was created in order to assure that the NT measurement from the follow-up model aligns in the same spatial location as the time-averaged WSS value from the post-stenting model. First, both models were unwrapped using a process demonstrated by Gundert et al[44]. During the unwrapping, the model is mapped to a  $(\theta, L)$  coordinate system where  $\theta$  represents the angular position for 0-360 degrees in which the zero degree position is chosen by the user, and  $L$  represents the length along the vessel. The zero degree position is consistent for both the post-stent and follow-up

model. An imaginary line running down the epicardial surface (i.e. outer wall) of each artery was defined as the zero degree location. When saving the contours from the follow-up OCT image and post-stenting WSS slice, arbitrary initial zero degree locations are set. Next, we found the point nearest to the zero degree position (epicardial surface) for both the follow-up OCT image and equivalent post-stent time-average WSS slice from Paraview. The angle between the arbitrary initial zero degree locations and the point nearest the zero degree position was determined for the OCT contour and WSS slice using basic trigonometry. These angles were used as circumferential rotations. The respective circumferential rotations were applied to shift the initial zero degree positions to the epicardial zero degree position for the follow-up OCT contour and post-stenting WSS slice. A plot was created illustrating that the shifted zero degree location matches the epicardial zero degree location to assure that the shift was applied in the correct direction. This process is illustrated in Figure 16.

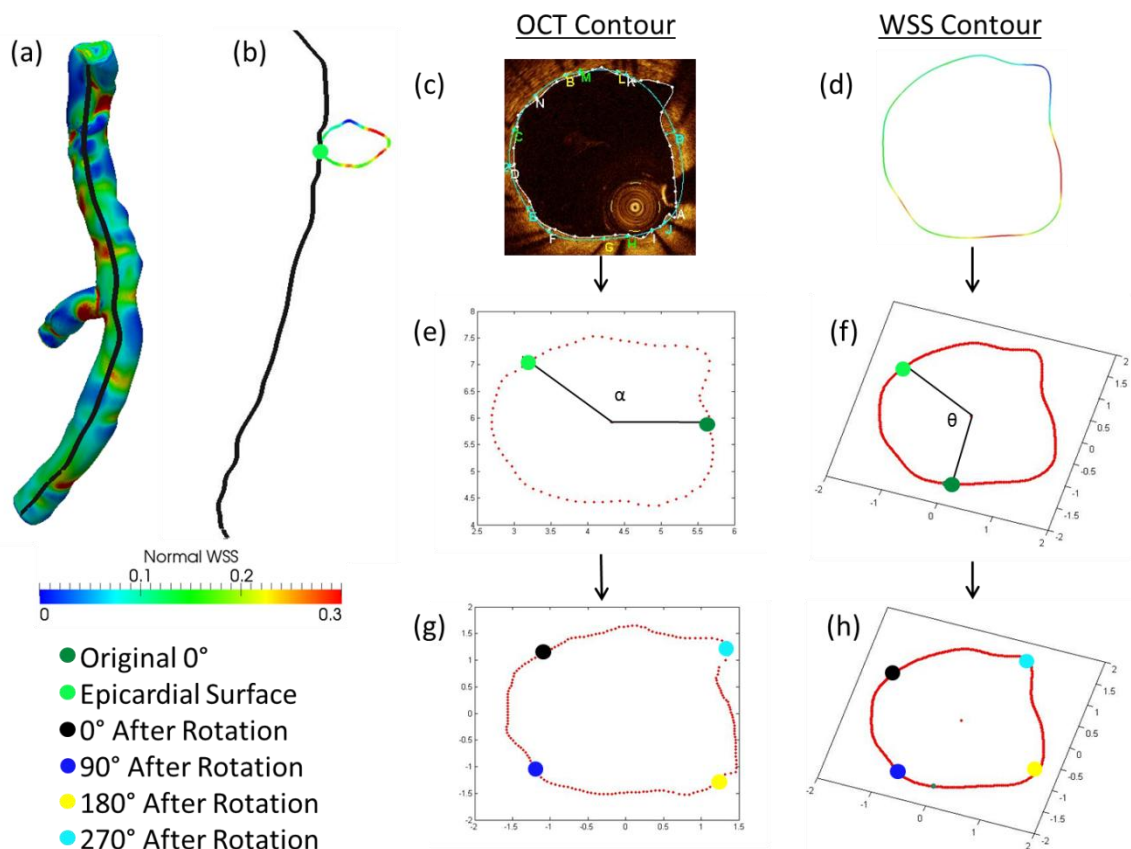


Figure 16: WSS results from CFD with the zero degree position line (epicardial surface) from unwrapping (a). Zero degree line with Paraview slice (b). OCT image (c) and Paraview slice (d) are isolated to create their respective contours (e and f, respectively). Rotations  $\theta$  and  $\alpha$  are determined for the OCT contour and Paraview slice between the initial zero degree point and the epicardial surface. Rotations are applied to the lumen contour (g) and Paraview slice (h) making the final zero degree position spatially consistent. 90°, 180°, and 270° positions are plotted to assure all points are spatially consistent.

## 2.9 Statistical Analysis

GraphPad Prism (GraphPad Software, Inc.) was used to perform statistical analyses between data points. Specifically, for each quantified metric (i.e. stent-to-lumen area ratio, stent-induced area of normalized low WSS, etc.), a one-way ANOVA analysis was performed to compare each of the stents to the other stents, that is, Nobori vs. Promus Element, Promus Element vs. Xience Prime, and Nobori vs. Xience Prime. A Tukey multiple comparisons test with a single pool variance was performed to determine

significance between stents. Data was considered statistically significant if  $P < 0.05$ .

Data are expressed as means  $\pm$  standard error of the mean (SEM).

## Chapter 3

---

### Results

#### **3.1 Patient-Specific WSS and OSI Results**

##### *3.1.1 Post-Stenting Results*

Post-stenting CFD model results for low normalized WSS and  $OSI > 0.1$  can be seen in Figure 17 and 18, respectively, for the three types of stents studied as well as by case number.

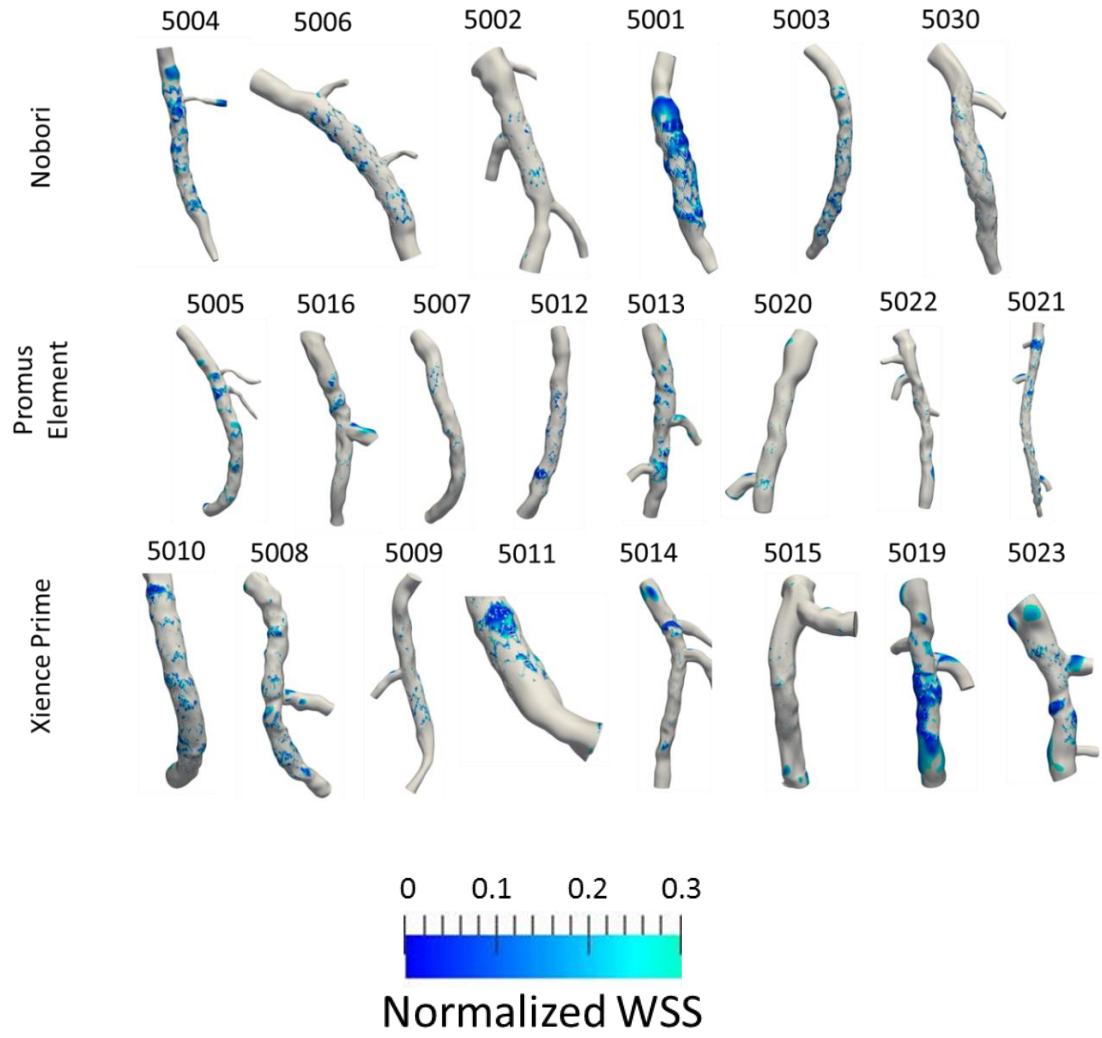


Figure 17: Post-stenting distributions of low normalized WSS.

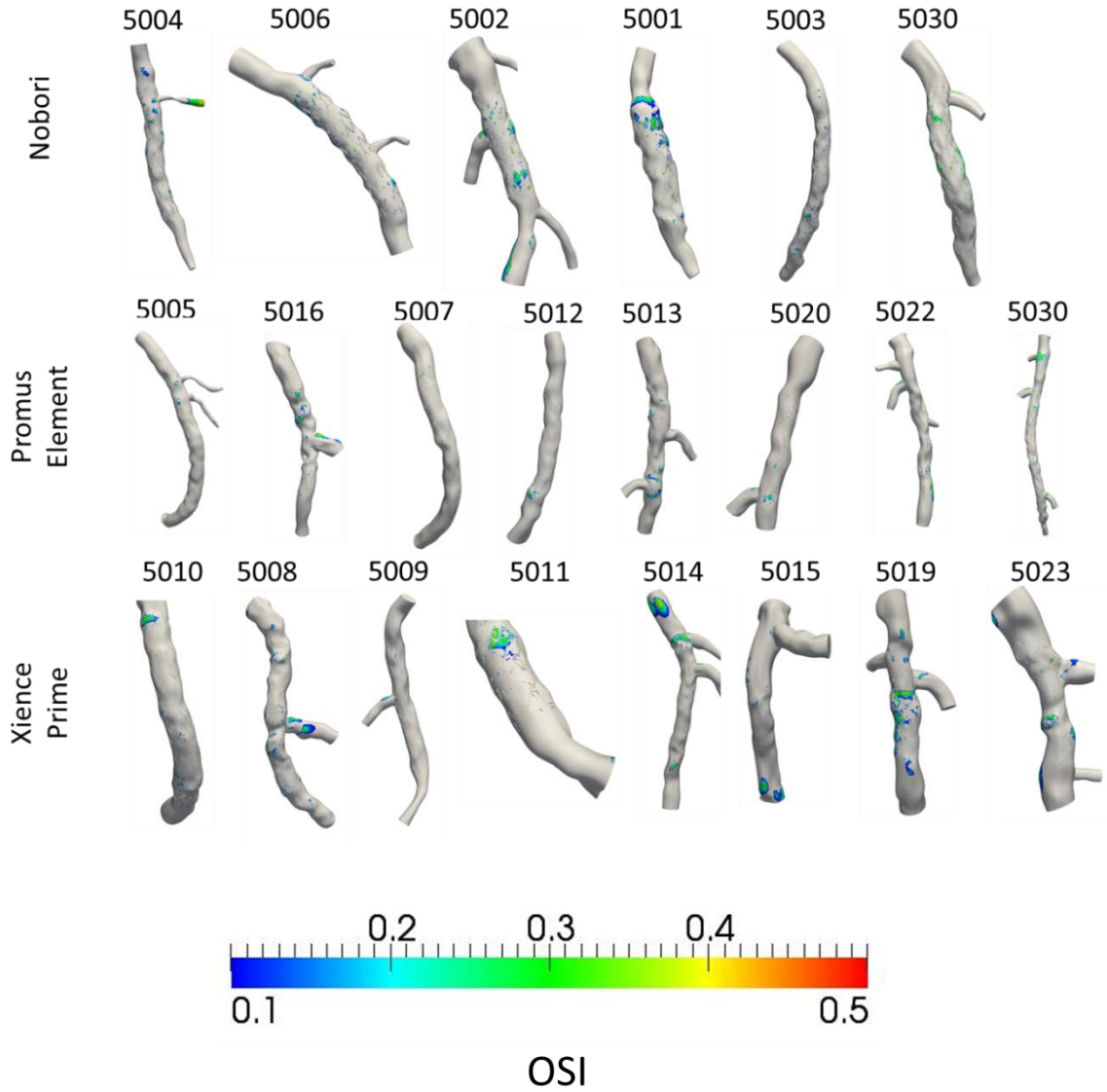


Figure 18: Post-stenting distributions of  $OSI > 0.1$ .

Stent-to-vessel area ratios for the three stents can be seen in Figure 19. The Nobori stent with its wider struts resulted in a significantly greater stent-to-vessel area ratio ( $0.34 \pm 0.04$ ) as compared to the Xience Prime ( $0.21 \pm 0.03$ ), but not the Promus Element ( $0.24 \pm 0.04$ ) stent.



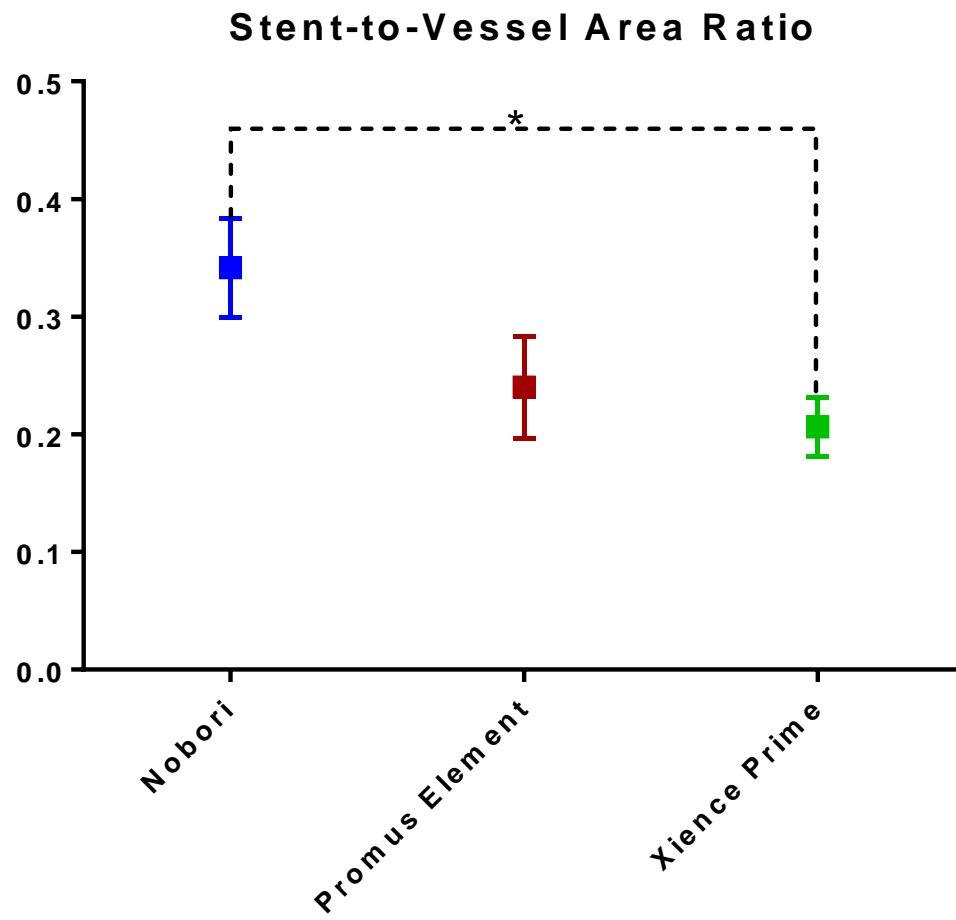


Figure 19: Comparison of the stent-to-vessel area ratio, \*=significance (mean±SEM).

Distributions of normalized low WSS as a percentage of the entire artery model at post-stenting were greatest for the Nobori, followed by the Xience Prime and Promus Element stents (Figure 20;  $24.1\pm 6.7\%$ ,  $18.4\pm 4.6\%$ , and  $14\pm 2.2\%$ , respectively). These differences did not reach significance. Distributions of normalized stent-induced low WSS at post-stenting were greatest for the Nobori, followed by the Promus Element and Xience Prime stents (Figure 21;  $11.6\pm 2.31\%$ ,  $7.44\pm 1.76\%$ , and  $6.3\pm 1.2\%$ , respectively), but these differences did not reach significance.

### Normalized Area of Low WSS: Post Stenting (%)

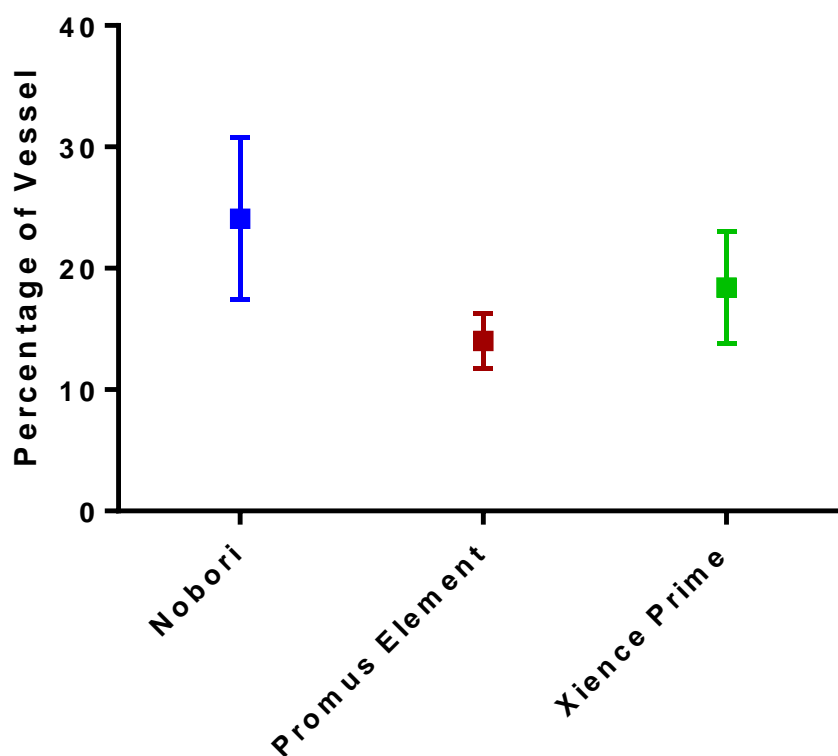


Figure 20: Comparison of the post-stenting normalized area of low WSS as a percentage of the entire vessel (mean $\pm$ SEM).

## Normalized Stent-Induced Area of Low WSS (%)

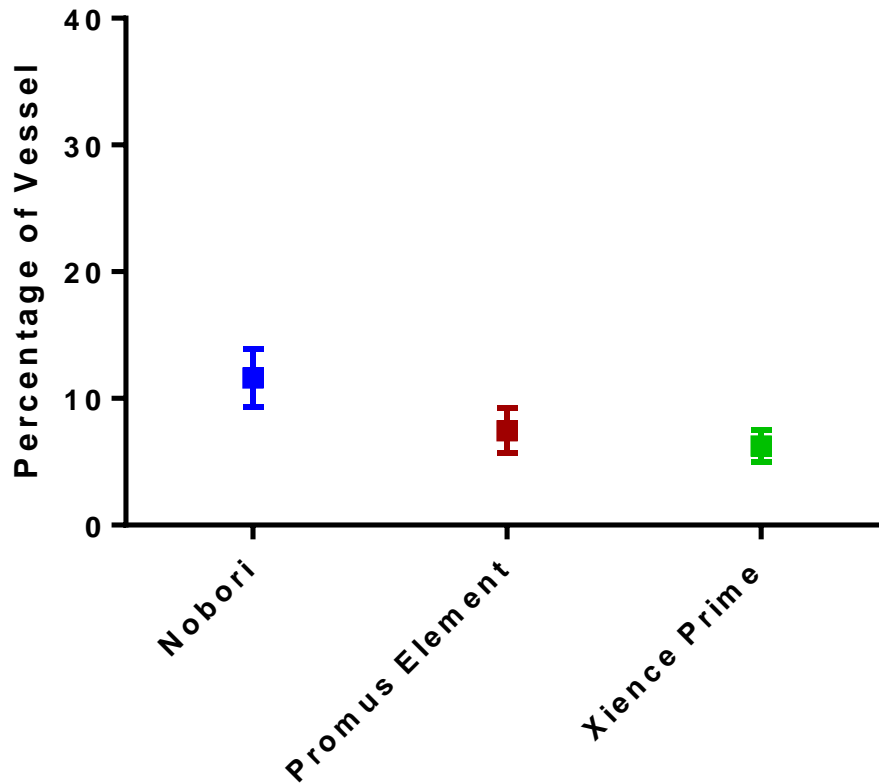


Figure 21: Comparison of the post-stenting normalized stent-induced area of low WSS (mean $\pm$ SEM).

The normalized stent-induced area of low WSS per stent length for the three stents can be seen in Figure 22. The Nobori stent with its thick struts resulted in a significantly greater normalized stent-induced area of low WSS per stent length ( $2.0\pm 0.41$  mm<sup>2</sup>/mm) as compared to the Promus Element ( $1.05\pm 0.27$  mm<sup>2</sup>/mm), but not for the Xience Prime ( $1.1\pm 0.2$  mm<sup>2</sup>/mm).

## Normalized Stent-Induced Area of Low WSS Per Stent Length ( $\text{m m}^2/\text{m m}$ )

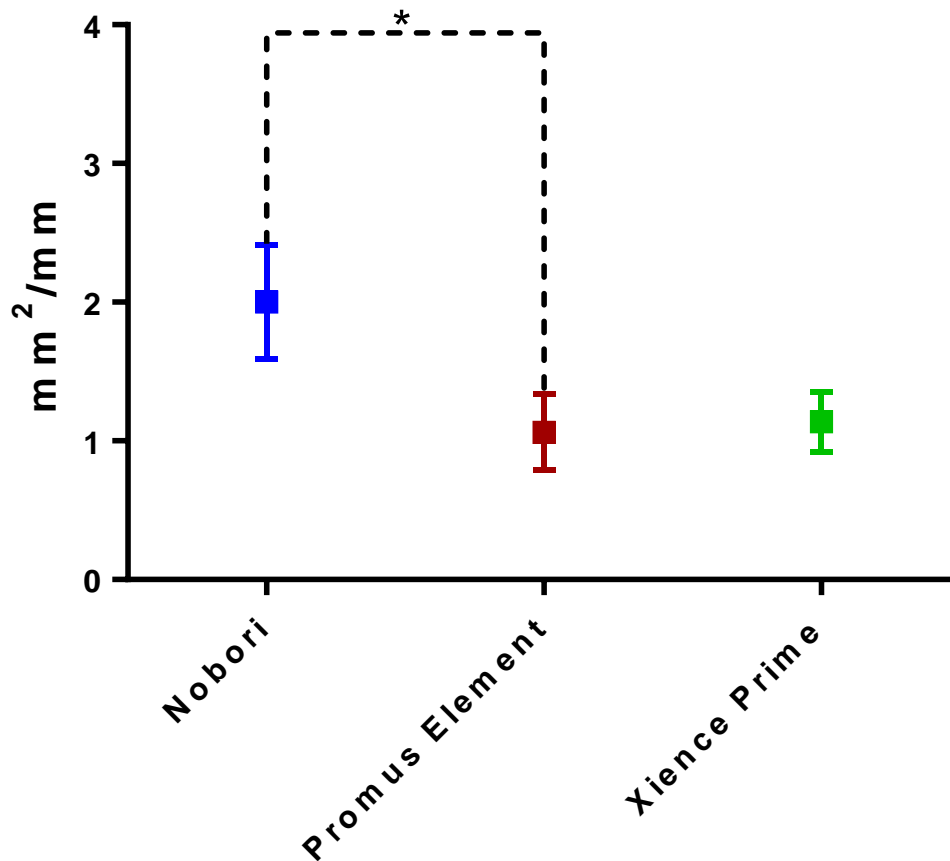


Figure 22: Comparison of the post-stenting normalized stent-induced area of low WSS per stent length, \*=significance (mean $\pm$ SEM).

The percentage of stent-induced OSI > 0.1 for the three stents can be seen in Figure 23. The Nobori stent with thicker struts and greater stent-to-vessel area ratio resulted in a significantly greater percentage of stent-induced OSI > 0.1 (4.5 $\pm$ 1.0%) as compared to the Xience Prime (1.4 $\pm$ 0.3%) and Promus Element (1.2 $\pm$ 0.3%).

## Stent-Induced OSI > 0.1: Post Stenting (%)

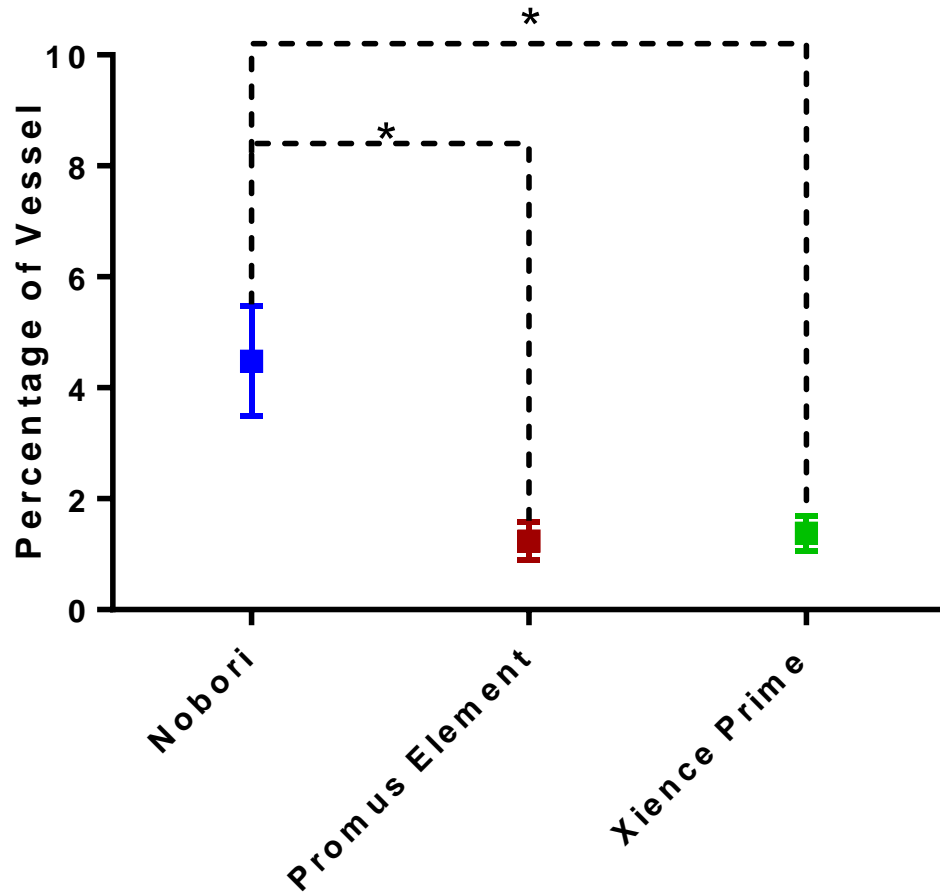


Figure 23: Comparison of the post-stenting stent-induced OSI greater than 0.1, \*=significance (mean±SEM).

### 3.1.2 Follow-up Results

Follow-up CFD model results for low normalized WSS and OSI > 0.1 for all three stent models can be seen in Figure 24 and 25, respectively.

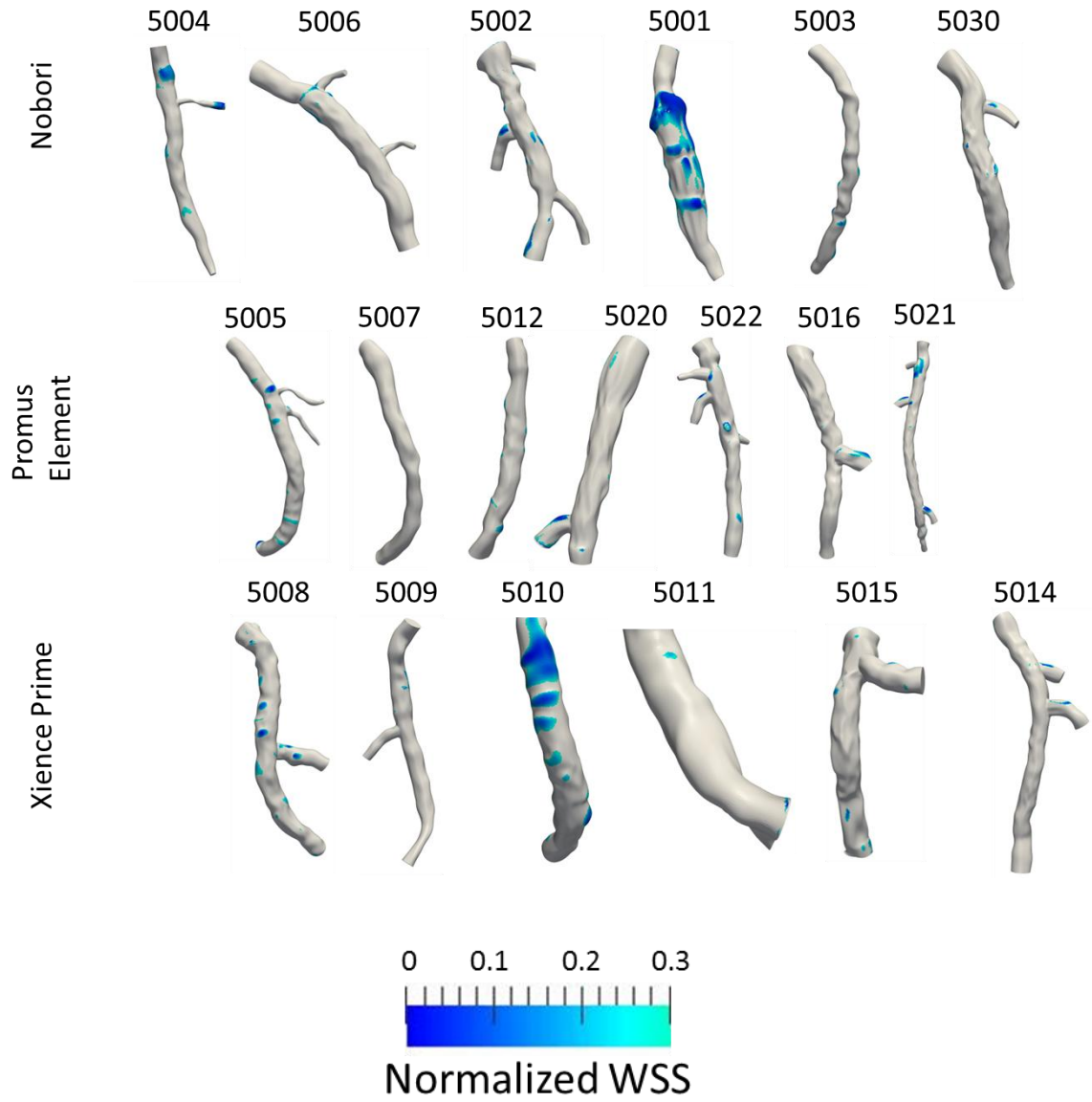


Figure 24: Follow-up distributions of low normalized WSS.

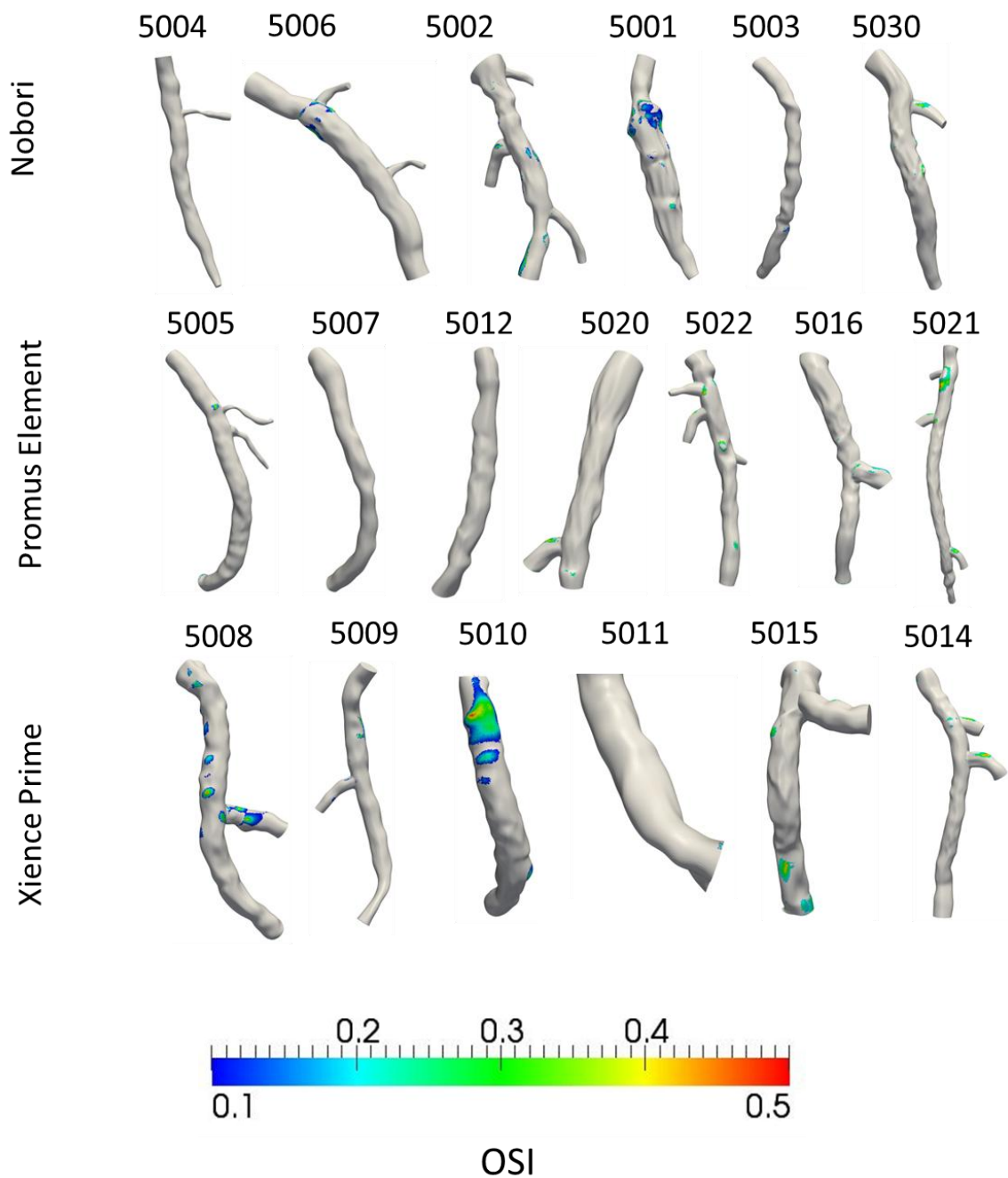


Figure 25: Follow-up distributions of OSI > 0.1.

Distributions of normalized low WSS as a percentage of the entire vessel model at follow-up were greatest for the Nobori, followed by the Xience Prime and Promus Element stents (Figure 26;  $10.7 \pm 6.4\%$ ,  $7.7 \pm 2.0\%$ , and  $5.8 \pm 1.2\%$ , respectively). These

differences did not reach significance. This order of outcomes based on stent model was also found in normalized area of low WSS per stent length at follow-up (Figure 27;  $0.7\pm 0.5\%$ ,  $0.4\pm 0.1\%$ , and  $0.3\pm 0.1\%$ , respectively). These differences did not reach significance.

### Normalized Area of Low WSS: Follow-Up (%)

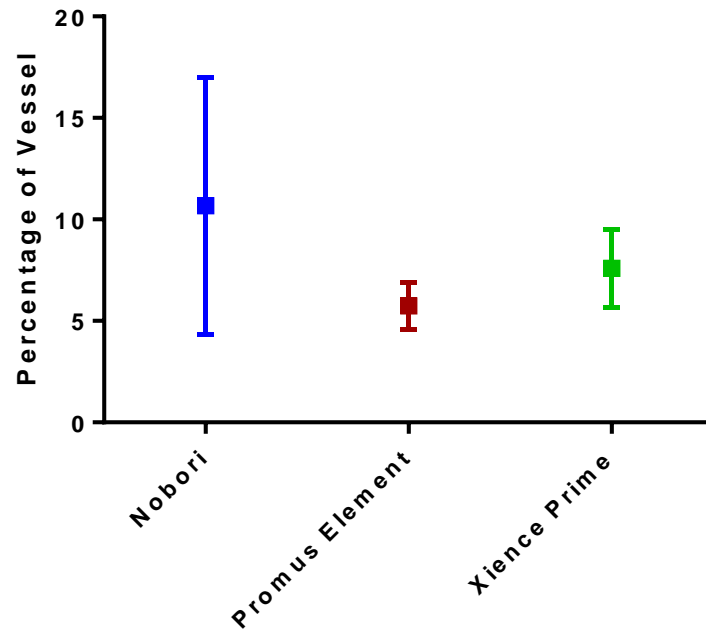


Figure 26: Comparison of the follow-up normalized area of low WSS as a percentage of the entire vessel (mean $\pm$ SEM).



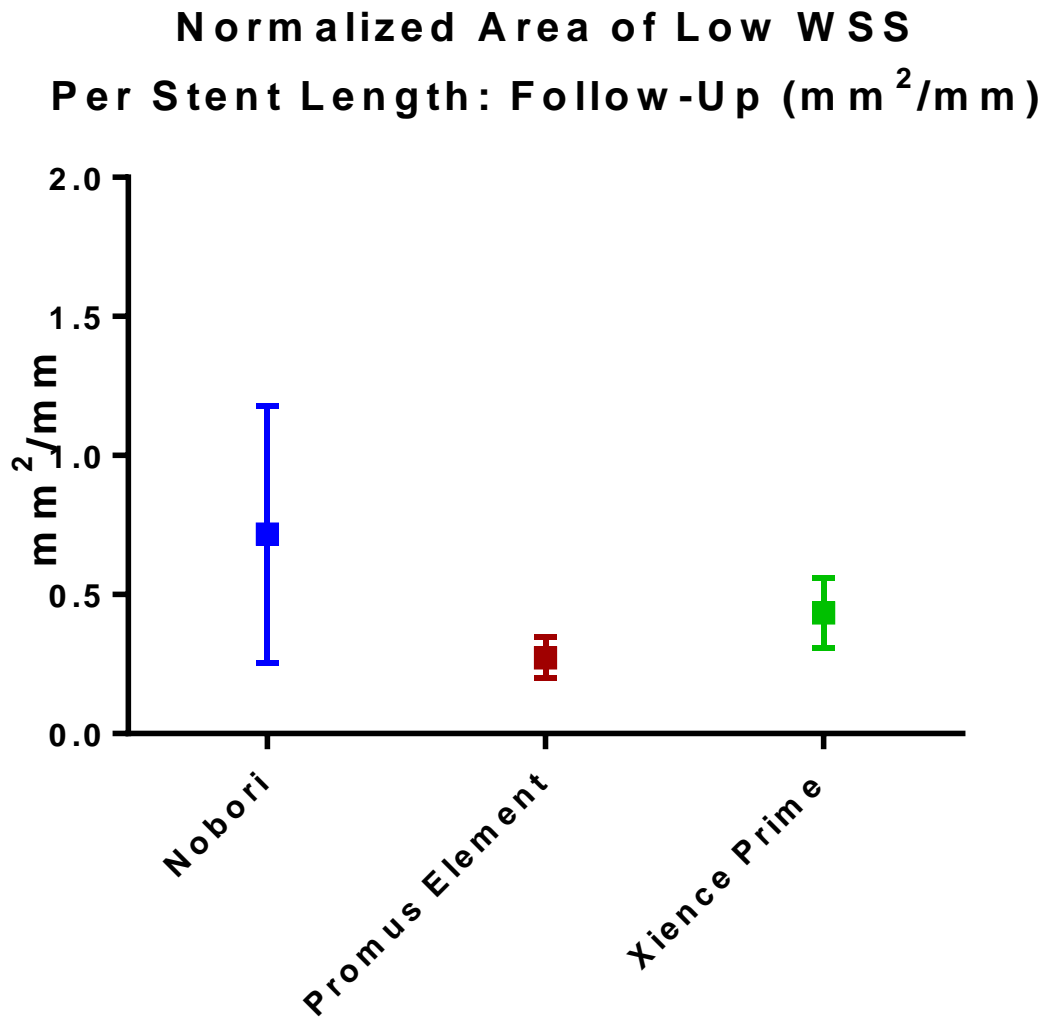


Figure 27: Comparison of the follow-up normalized stent-induced area of low WSS per stent length (mean $\pm$ SEM).

Post-stenting and follow-up CFD model results for low normalized WSS for all three stent models can be seen side by side in Figure 28.

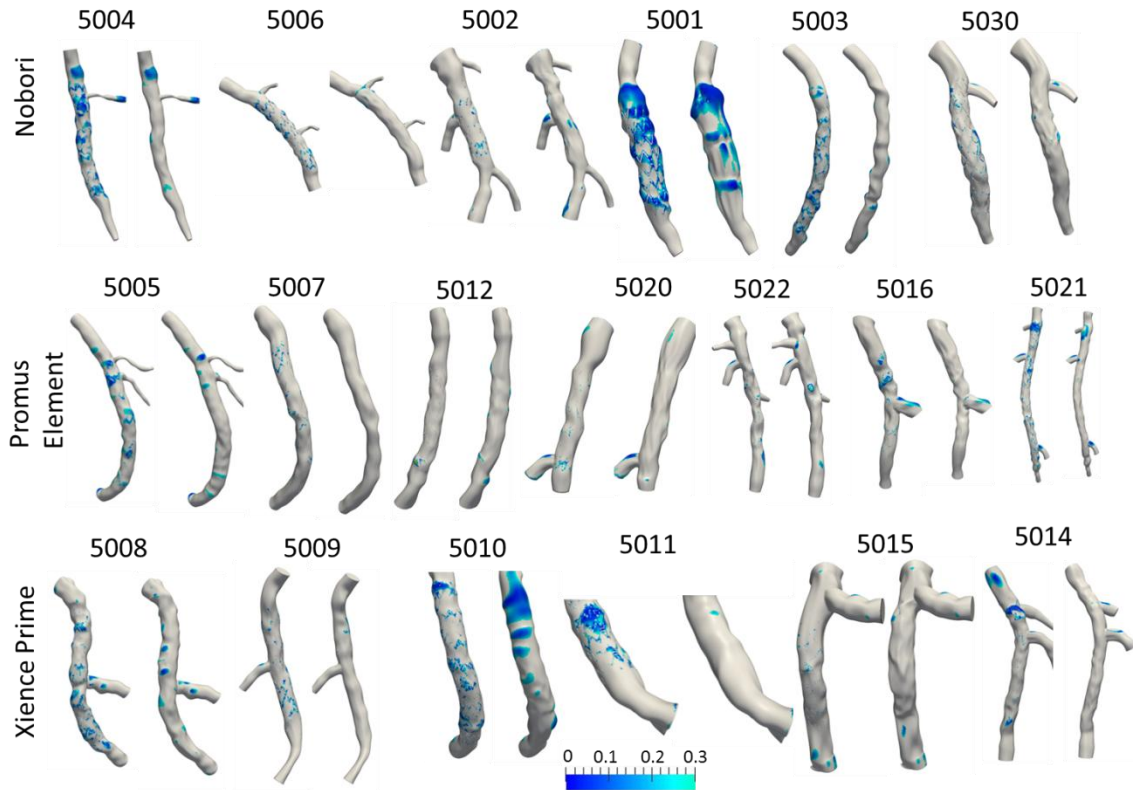


Figure 28: Post-stenting and follow-up distributions of low normalized WSS.

For all groups of stents, the normalized area of low WSS decreased from post-stenting to follow-up. This decrease in normalized area of low WSS between post-stenting and follow-up was greatest for the Nobori ( $13.4\pm 3.4\%$ ) followed by Promus Element ( $7.2\pm 1.6\%$ ) and Xience Prime ( $4.8\pm 1.6\%$ ). The difference between the Nobori and Xience Prime was significant (Figure 29). One patient (5010) had increased distributions of normalized low WSS at follow-up compared to post-stenting. This was due to tissue resorption in an area of the stented region, causing the area of the vessel to increase, thereby further decreasing adverse WSS distributions.

### Normalized Area of Low WSS Difference Between Post and Follow-Up (%)

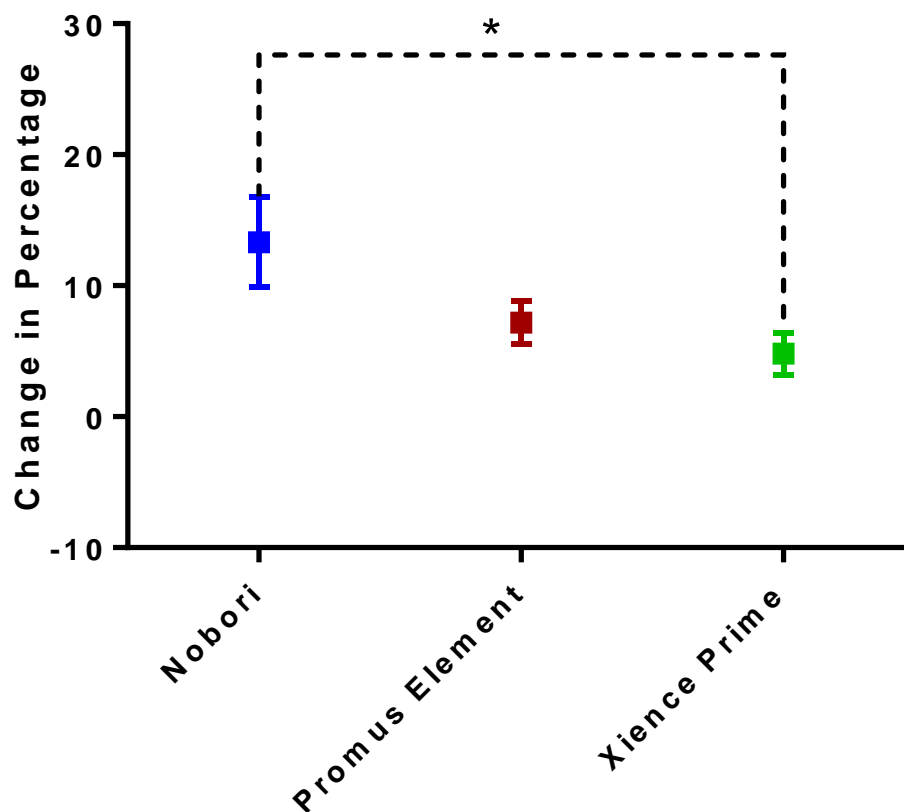


Figure 29: Comparison of the post-stenting and follow-up normalized area of low WSS as a percentage of the entire vessel, \*=significance (mean±SEM).

OSI > 0.1 as a percentage of the entire vessel model at follow-up was greatest for the Nobori, followed by the Xience Prime and Promus Element stents (Figure 30; 5.2±1.2%, 4.9±1.0%, and 2.4±0.8%, respectively). The differences between stents did not reach significance.

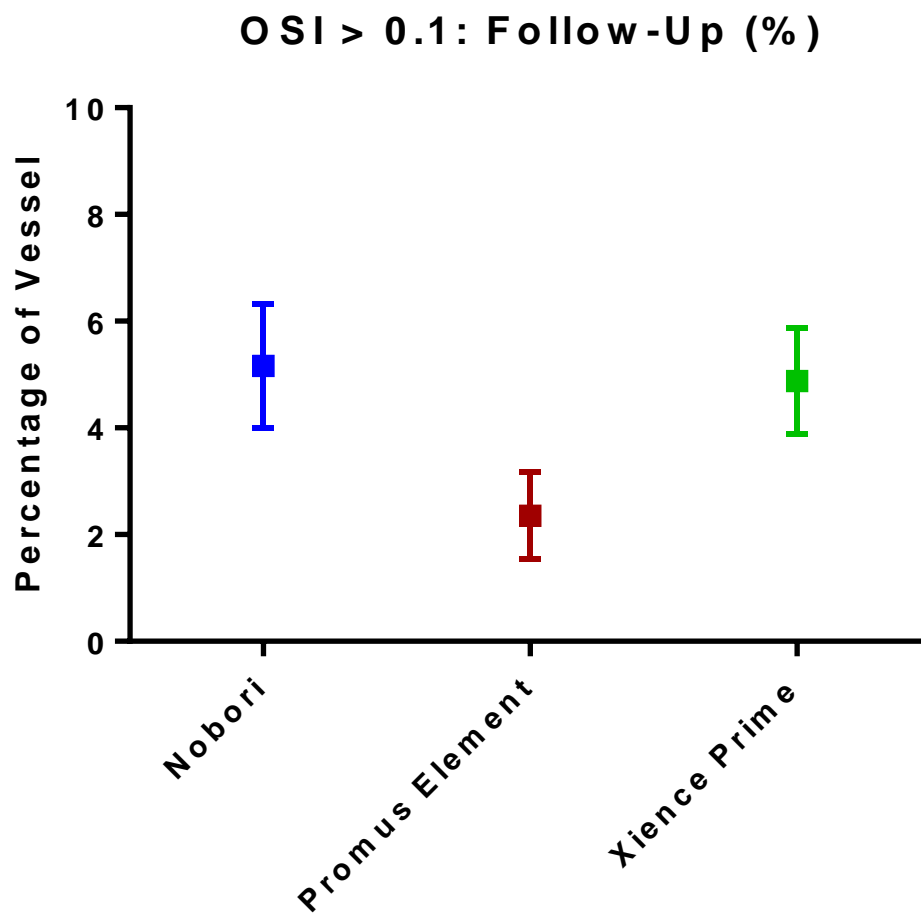


Figure 30: Comparison of the follow-up OSI greater than 0.1 (mean±SEM).

For all groups of stents, OSI > 0.1 decreased from post-stenting to follow-up (Figure 31). This decrease in OSI > 0.1 between post-stenting and follow-up was greatest for the Nobori ( $4.8 \pm 2.2\%$ ) followed by Promus Element ( $1.0 \pm 0.4\%$ ) and Xience Prime ( $0.4 \pm 0.4\%$ ). The differences between stents did not reach significance.

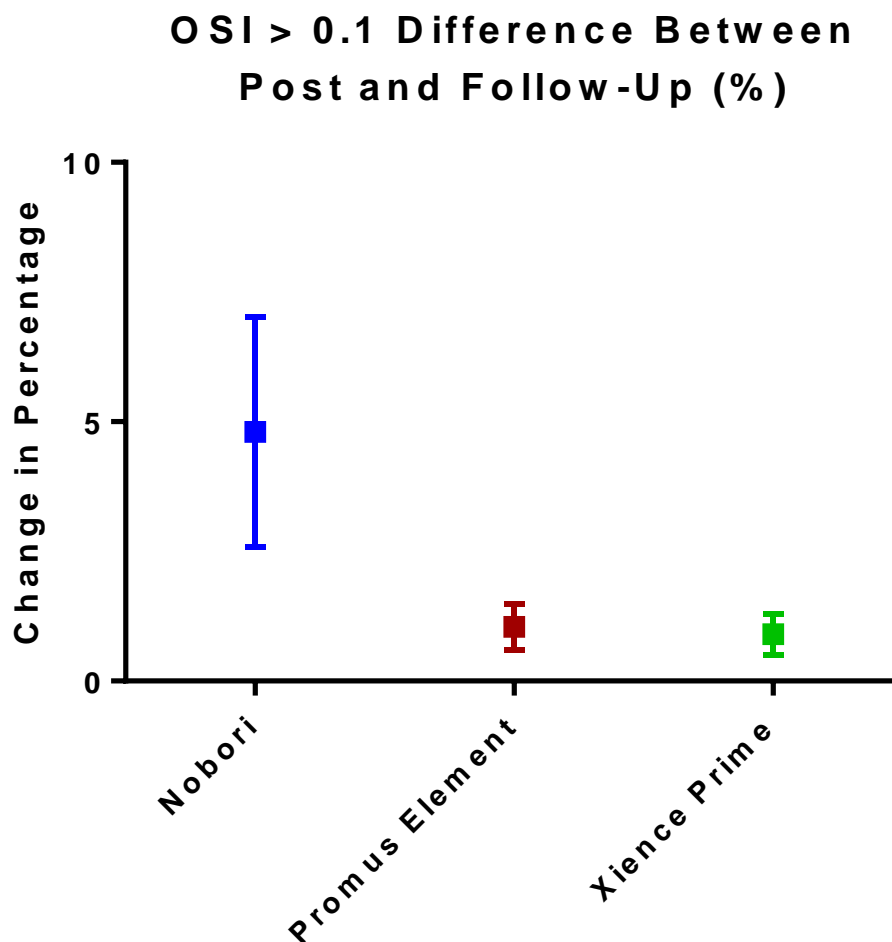


Figure 31: Comparison between post-stenting and follow-up OSI greater than 0.1 (mean $\pm$ SEM).

### 3.2 Post-Stenting WSS and Follow-Up Tissue Growth

#### 3.2.1 Comparison Between Post-Stenting WSS and Follow-Up Neointimal Tissue

Inverse correlations were observed between values of post-stent WSS and NT at follow-up for all stents. These correlations are determined using linear regression analysis producing a correlation coefficient and slope value, as demonstrated in previous studies[39], [41]. Figure 32 shows a representative version of the correlation between post-stenting WSS and NT at follow-up.

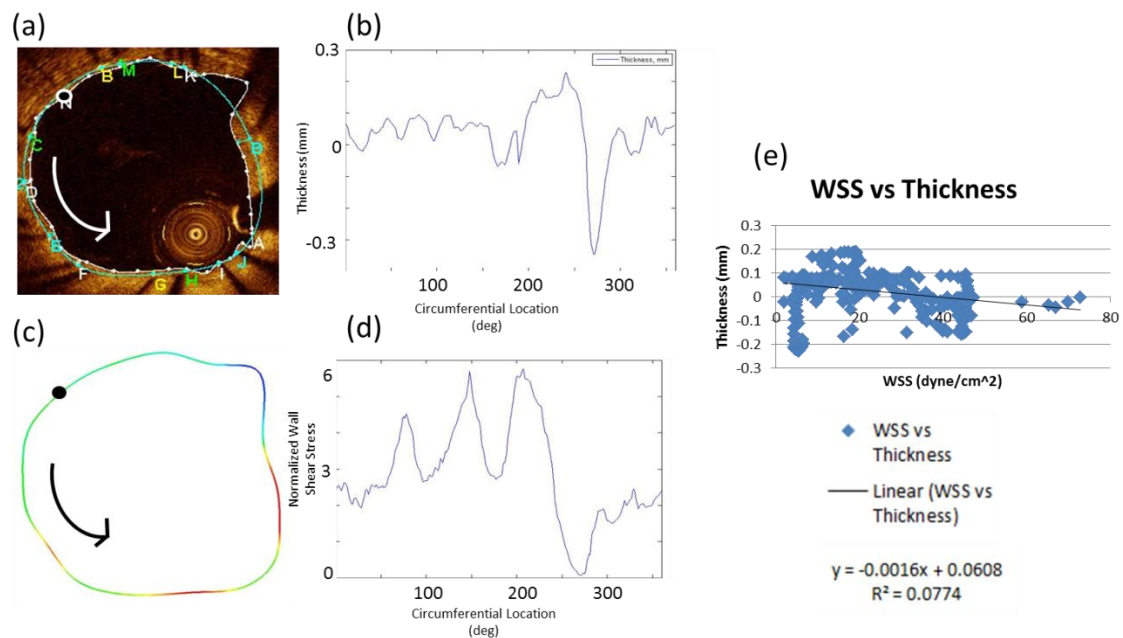


Figure 32: OCT image at follow-up (a) with circumferential NT measurements starting at the zero degree position (b). Paraview slice at post-stenting (c) with circumferential WSS measurements starting at the zero degree position (d). Correlation between post-stenting WSS and NT at follow-up (e).

Correlations for all quantified regions can be found in Figures 33-38. Excluding the distal and middle regions, this inverse correlation was greatest for the Nobori stent. Also, for all regions excluding the proximal region, the inverse correlation was least for the Xience Prime stent.

When combining the data from the proximal, middle, and distal regions, the inverse correlation between post-stenting WSS and NT at follow-up was greatest for the Nobori ( $-0.019 \pm 0.001$  mm/Pa) followed by Promus Element ( $-0.017 \pm 0.003$  mm/Pa) and Xience Prime ( $-0.008 \pm 0.003$  mm/Pa). The difference between the Nobori and Xience Prime was significant (Figure 38).

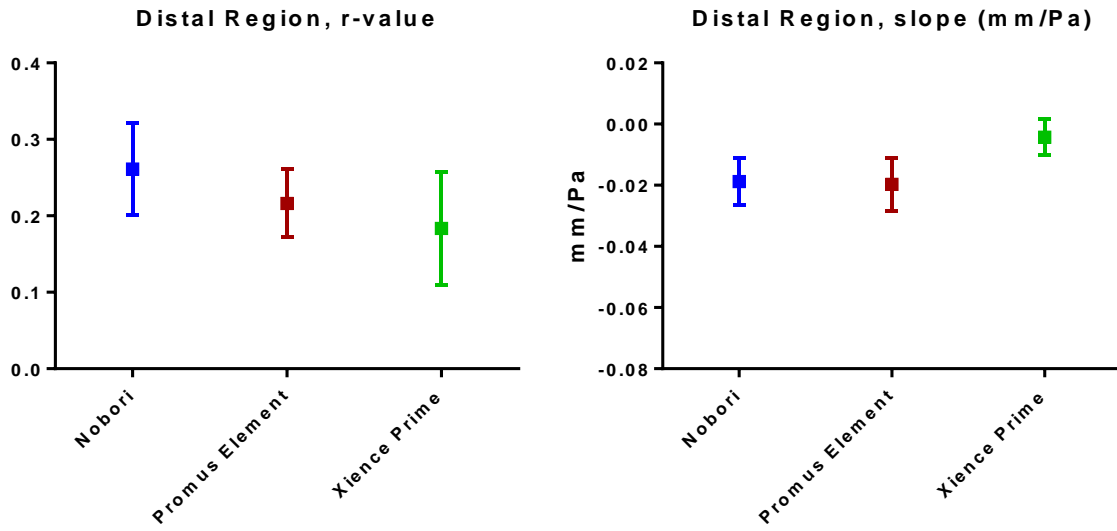


Figure 33: Distal region comparison of inverse correlations of post-stenting WSS and follow-up neointimal thickness represented by the r-value and slope from regression analysis (mean $\pm$ SEM).

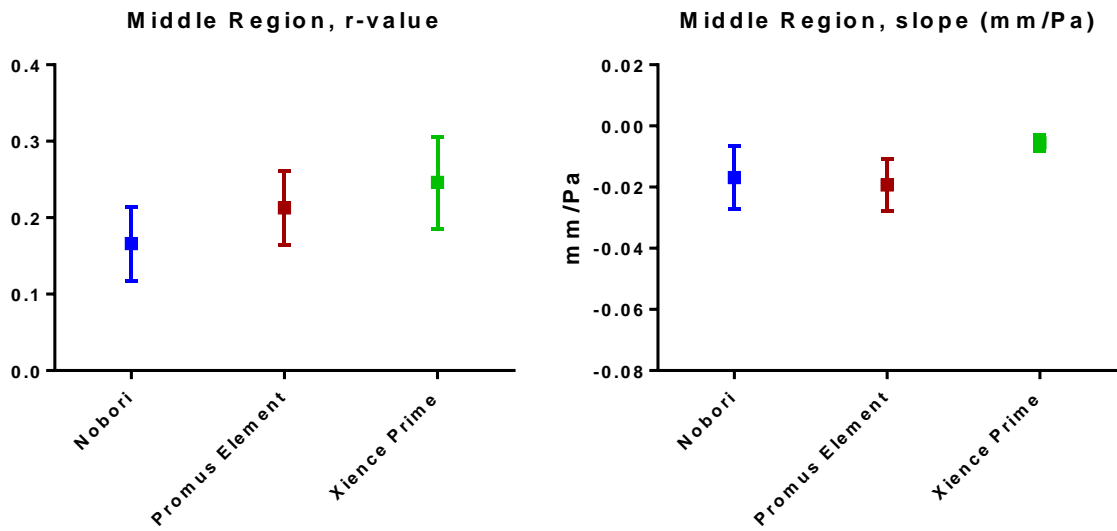


Figure 34: Middle region comparison of inverse correlations of post-stenting WSS and follow-up neointimal thickness represented by the r-value and slope from regression analysis (mean $\pm$ SEM).

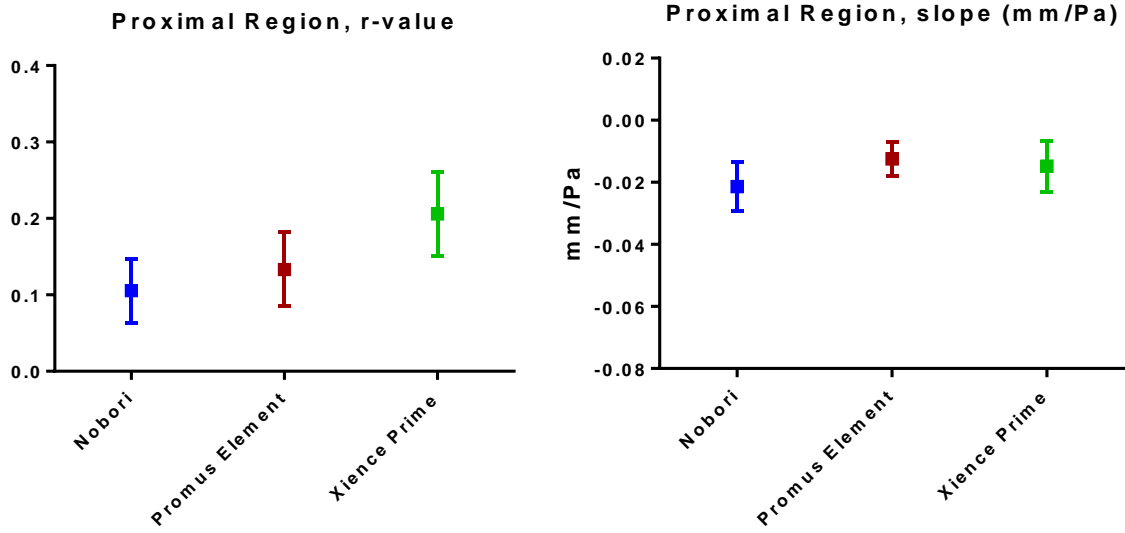


Figure 35: Proximal region comparison of inverse correlations of post-stenting WSS and follow-up neointimal thickness represented by the r-value and slope from regression analysis (mean±SEM).

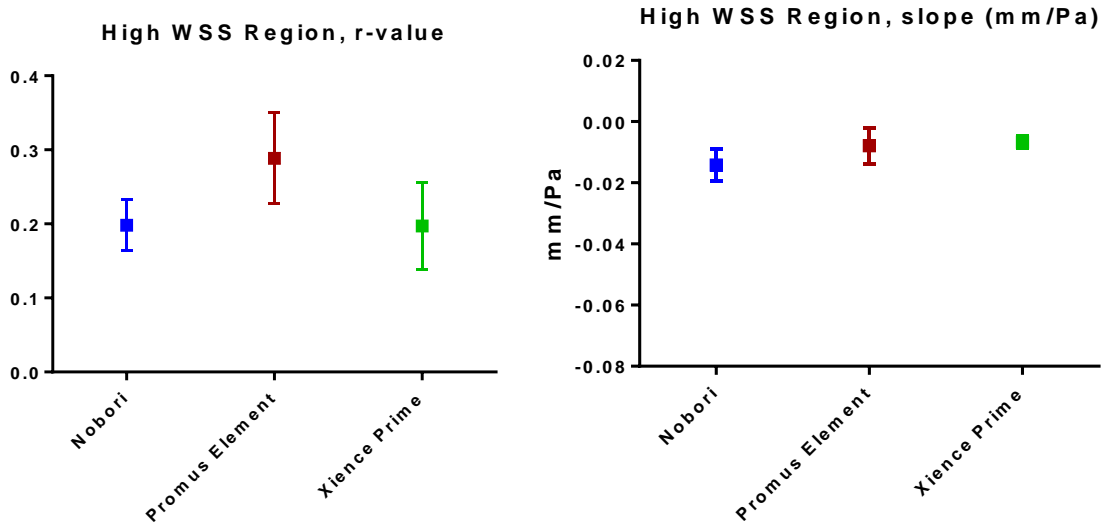


Figure 36: High WSS region comparison of inverse correlations of post-stenting WSS and follow-up neointimal thickness represented by the r-value and slope from regression analysis (mean±SEM).



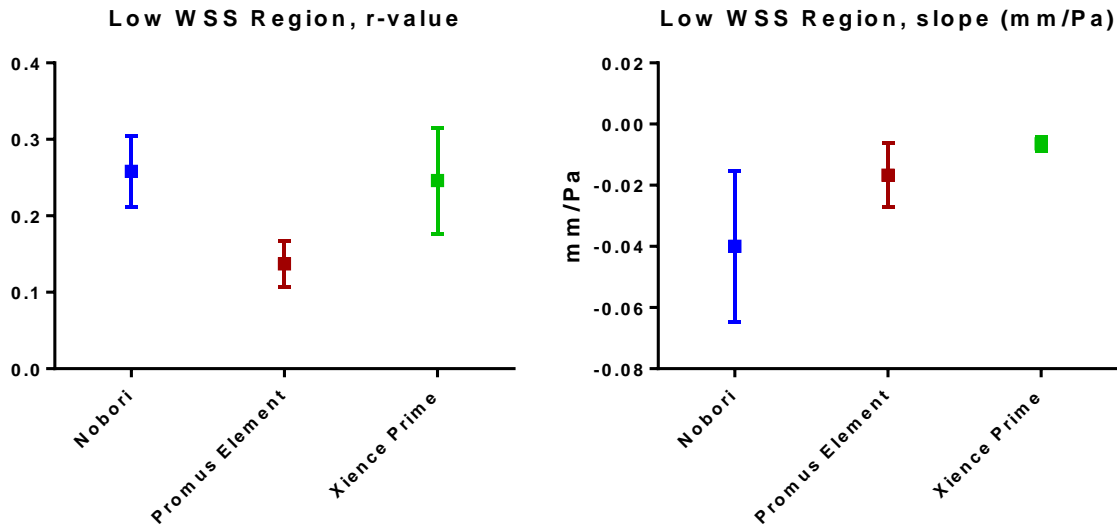


Figure 37: Low WSS region comparison of inverse correlations of post-stenting WSS and follow-up neointimal thickness represented by the r-value and slope from regression analysis (mean±SEM).

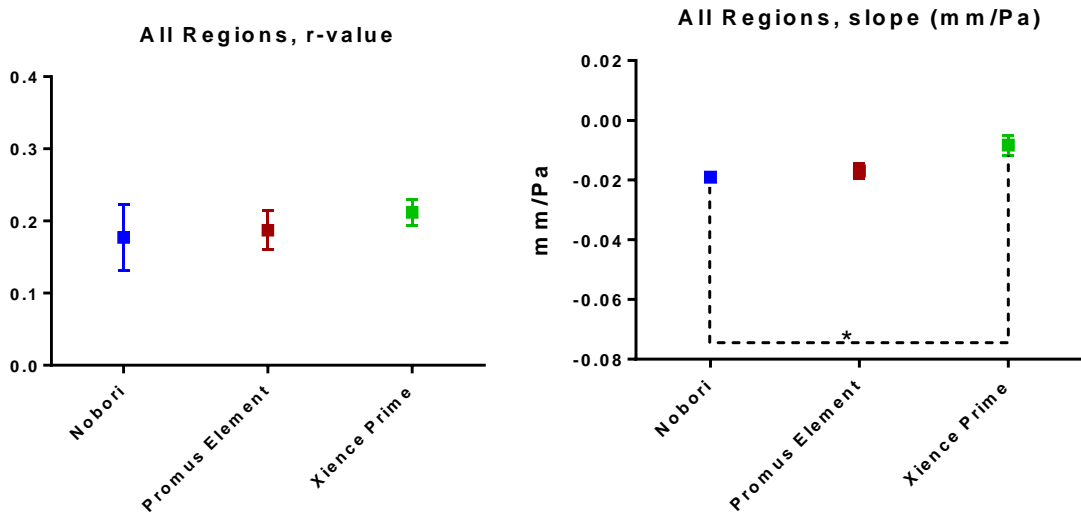


Figure 38: Combined proximal, middle, and distal regions comparison of inverse correlations of post-stenting WSS and follow-up neointimal thickness represented by the r-value and slope from regression analysis, \*=significance (mean±SEM).

### 3.2.2 Total Neointimal Growth at Follow-Up

The decrease in volume of the vessel during the follow-up is shown in  $\text{mm}^3$  (Figure 39) and as a percentage change from post-stenting to follow-up (Figure 40). Decrease in volume in  $\text{mm}^3$  at follow-up was greatest for the Nobori, followed by the Promus Element and Xience Prime stents but differences did not reach significance (Figure 39;  $14.7 \pm 4.2 \text{ mm}^3$ ,  $6.4 \pm 3.8 \text{ mm}^3$ , and  $6.2 \pm 3.2 \text{ mm}^3$ , respectively). This order of outcomes based on stent model was also found in percentage decrease in volume from post-stenting to follow-up but differences did not reach significance (Figure 40;  $12 \pm 3.9\%$ ,  $5.8 \pm 3.5\%$ , and  $5.2 \pm 2.3\%$ , respectively).

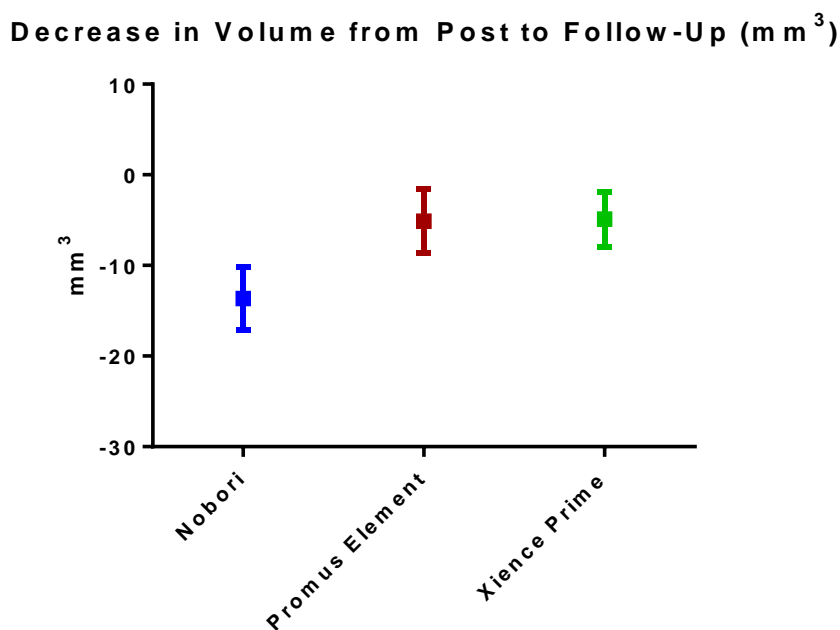


Figure 39: Comparison of the change in volume from post-stenting to follow-up (mean  $\pm$  SEM).

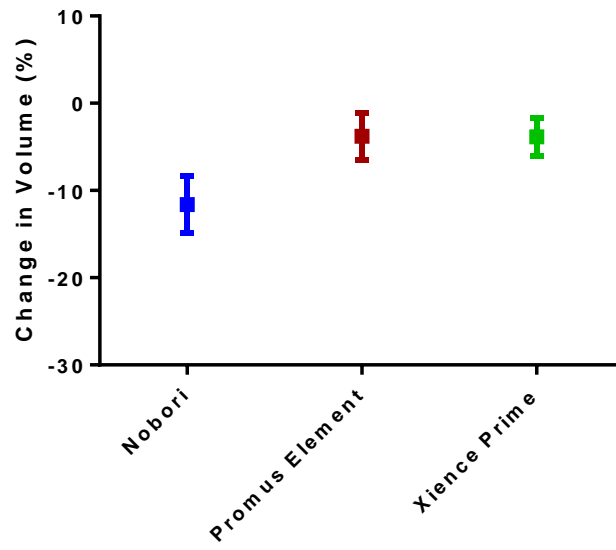
**Decrease in Volume from Post to Follow-Up (%)**

Figure 40: Comparison of the change in volume from post-stenting to follow-up as a percent of post-stenting volume (mean $\pm$ SEM).

## Chapter 4

---

### Discussion

#### **4.1 Review of Specific Aims and Summary of Major Findings**

The objective of this study was to evaluate three current generation stent geometries via WSS patterns, and their respective impact on NT, a component of restenosis. To satisfy this objective, OCT and CTA data were obtained just after stent implantation and at 9-months follow-up. CFD simulations were performed on the post-stent and follow-up patient-specific models to analyze the effects of the Nobori, Promus Element, and Xience Prime stents via their WSS distributions and respective NT. Furthermore, this thesis was separated into three aims to better understand the effects of the stents, that is, evaluate the relationship between low WSS distributions and stent geometry, compare post-stent and follow-up low normalized WSS, and the correlation between post-stent WSS and follow-up NT.

The first aim of this study was to use patient-specific models to confirm previous idealized studies regarding the amount of low WSS and stent design. Stent design has been shown to influence local distribution of adverse WSS and correlate with NT. For example, Gundert et al performed CFD simulations on idealized stented coronary arteries. Their study created a hierarchy of stent design factors that can lead to adverse WSS distributions. The authors found that strut thickness had the greatest impact on adverse WSS distributions. When this attribute was similar among stent designs, the stent-to-lumen area ratio, angle of struts relative to the primary direction of blood flow, and arrangement of connector elements were also predictive of adverse WSS

distributions. Using patient-specific models, we were able to confirm the conclusions from the idealized study. The data presented in the current work indicates that the greater stent-induced low normalized WSS in the Nobori (n=6) compared to the Promus Element (n=8) and Xience Prime (n=8) is attributed to the larger strut thickness and increased stent-to-lumen area ratio. While the strut thickness for the Promus Element and Xience Prime are the same, the difference in low normalized WSS per stent length may be caused by the increased number of connectors in the Xience Prime.

The second aim of this study was to compare post-stent normalized low WSS with follow-up normalized low WSS. During the follow-up period, tissue grows atop and around the stent struts. This tissue growth should return the WSS distributions closer to the arteries' native values, decreasing the consequences of adverse WSS distributions. This aim was completed by comparing the low normalized WSS at post-stent and at follow-up for each patient. The pronounced reduction in normalized low WSS from post-stent to follow-up in the Nobori stents can be attributed to its thicker stent struts. Thicker struts provide more space for the tissue to grow. Therefore, the Nobori was anticipated to yield greater NT compared to the thinner struts of the Promus Element and Xience Prime.

The third aim of this study was to evaluate post-stent WSS and follow-up NT. Adverse distributions of WSS triggered by stenting can cause increased NT leading to restenosis. In order to complete this aim, NT measurements from follow-up models were correlated with WSS measurements from the post-stent model. The correlation between post-stent WSS and follow-up NT could be attributed to the mechanism of action for the specific elution agent as previously suggested[39], [41]. NT leading to restenosis is a process dictated by arterial wall remodeling as well as proliferation of smooth muscle

cells. Limus-based elution agents are thought to inhibit cell migration leading to NT by blocking the activation of mTOR, a protein kinase that plays a critical part in the signaling pathway that regulates cell growth[57][58]. Though limus-based DES agents are thought to inhibit NT regardless of WSS, our results show a potential inverse correlation with WSS for the biolimus-eluting Nobori. In contrast, the more favorable stent geometries of Promus Element and Xience Prime were associated with less of an influence of adverse WSS on NT.

Coupled with the mechanism of action for the elution agent, the correlation between post-stent WSS and NT at follow-up may be affected by stent geometry. The Promus Element and Xience Prime stents use the same drug-elution agent and coating, however, have different geometries. Our results for the Promus Element and Xience Prime show that there is a difference, though not significant, in correlation between post-stent WSS and follow-up NT. These differences may be caused by different WSS distributions that in turn affect the amount of drug absorbed in the vessel wall.

All arteries have a homeostatic WSS value. After stent implantation, WSS values within the stented region will typically decrease since all stents need to be implanted to a diameter larger than the native vessel diameter. Arteries undergo autoregulation (i.e. tissue growth or resorption) in an effort to return the WSS distributions to more preferential native range of values. Knowing that the Nobori has thicker struts compared to the Promus Element and Xience Prime, one would expect greater flow disruptions resulting in greater areas of adverse WSS, which was illustrated in the current results. This is also likely the stimuli behind greater tissue growth compared to the thinner struts of the Promus Element and Xience Prime, even though all the stents have limus-based

elution agents. Due to the increased amount of adverse WSS distributions in the Nobori compared to the Promus Element and Xience Prime, it seems there is a threshold beyond which the effects of the drug-elution agent are mitigated.

After WSS distributions return to their homeostatic value, there is a possibility of neointimal tissue continuing to grow. This is known as late catch-up and can be attributed to delayed healing and local inflammatory reactions to the polymer carrier. Long-term studies conducted by Hagiwara et al found that the Nobori maintained efficacy after 15 months and can reduce rates of late restenosis due to its polymer degradation[59]. These long-term effects were not within the scope of the current study.

From these results, it seems that while the DES elution agent can be an important factor in NT, stent geometry (e.g. strut thickness) still plays a vital role in the effect of WSS on NT.

#### **4.2 Relationship to Previous Work Underscoring Unique Contributions**

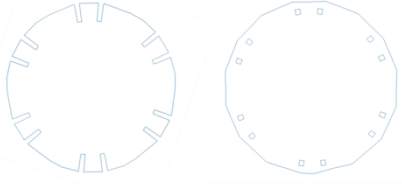

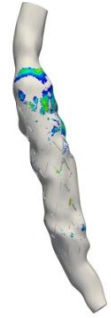

Using the same CFD approach as Ellwein et al, this project was able to confirm idealized findings from Gundert et al regarding adverse WSS distributions and stent geometry using a large population of patient-specific models[34]. This confirmation helps prove that stent design factors (i.e. strut thickness, number of connectors) have an effect on the WSS distributions in human coronary arteries.

There have been several small studies correlating WSS distribution to sites of NT for first generation DES. Gijssen et al presented a study using 3-dimensional lumen reconstruction and computational fluid dynamics to analyze the relationship between blood-flow induced WSS and NT in 6 patients with first-generation sirolimus-eluting stents. Linear regression showed an inverse relationship between NT and WSS.

Papafaklis et al conducted a study analyzing the relationship between WSS and NT following the implantation of sirolimus- and paclitaxel-eluting stents, both of which are first-generation DES. These findings were compared to the results produced by bare metal stents. The study involved 30 total patients, 10 per stent group. Results showed a significant inverse relationship between WSS and NT for the paclitaxel-eluting stents. However, contrary to the before mentioned study (Gijssen et al), this relationship was absent in the sirolimus-eluting stents. The current project is the largest known study to date to analyze the impact of WSS on NT at several regions of the stented artery (i.e. distal, middle, proximal, high WSS, low WSS) in the setting of current generation DES. Similar to prior findings correlating WSS to NT in 6 patients with sirolimus-eluting DES by Gijssen et al, the inverse correlation in areas of low WSS were present for the biolimus-eluting Nobori (n=6) and the everolimus-eluting Promus Element (n=7) and Xience Prime (n=6).

As mentioned throughout this thesis, there are several aspects of this study that are novel contributions to science. These contributions are summarized in Table 2.



Novel Aspect of Thesis	Description	Image
Accounting for malapposed struts	When virtually implanting stents into a patient-specific artery, previous methods did not account for malapposed struts, thereby leading to thickened representations of struts to an unrealistic dimension.	 <p>Previous method (left) and current method (right)</p>
Implanting stent based on circumferential and longitudinal locations	When virtually implanting stents, stent placement is based on the longitudinal location in the artery as well as the circumferential locations of the struts. This process assures for an accurate stented model.	 <p>Previous method (middle) and current method (right) shifting the stent based on the OCT image (left) * = guidewire artifact. ● = stent strut.</p>
Analyze and visualize OSI > 0.1	A custom program allows for the calculation of the percentage of the vessel above a threshold. Program also isolates this area of the vessel for visualization.	 <p>OSI &gt; 0.1</p>
Distinguish between adverse wall shear stress distributions caused by local vessel geometry and the implanted stent	To calculate the stent-induced area of low WSS, simulations were performed on un-stented arteries created from and subtracted from the stented vessel. This eliminates the normalized low WSS areas that are caused by vessel geometry, rather than that of the implantation of the stent.	 <p>Low normalized WSS distributions produced by the vessel (left) and by the vessel and stent geometry (right).</p>

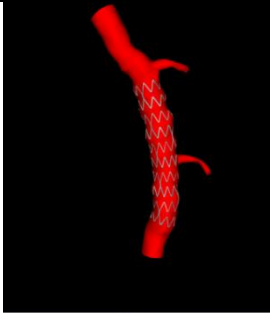
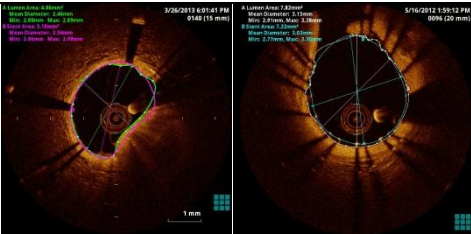
<p>Determining patient-specific stent-to-vessel area ratio</p>	<p>The stent-to-vessel area ratio represents the area of exposed stent to the area of the lumen within the flow domain where the stent was deployed</p>	 <p>Stented coronary artery with area of the stent in contact with the lumen wall highlighted silver</p>
<p>Additions to the reconstruction code</p>	<p>In an effort to make the reconstruction code more robust, additions including being able to isolate OCT contours of different color schemes, accepting OCT images of different sizes, and adding an input of the pixel per millimeter ratio of the OCT image series.</p>	 <p>OCT images with different color schemes</p>

Table 2: Summarizing unique contributions this study presented.

### 4.3 Limitations

The current project should be interpreted within the constraints of several potential limitations. CT data was only acquired immediately post-stenting. This study did not take into consideration the possibility of any major structural changes in the arteries proximal or distal of the stented region during the 9-month follow-up. This was based on the knowledge that structural changes would be minimal. Also, this assumption greatly decreased computational time. The number of slices used here (one image per millimeter) is consistent with the current norm implemented during quantification clinically. However, the OCT imaging system has the capability to obtain 10 images per millimeter. Also, our methods do not take into account the elution distributions

implemented by the stent geometry or release kinetics of the drugs as it was not within the scope of this study. Finally, this study does not distinguish between types of tissue growth at follow-up. Due to the high resolution of the OCT image, it is possible to delineate and quantify superficial plaque with accuracy. This delineation is completed using the different intensities of various types of plaque. While this was not in the scope of this study, it is starting to be performed similar to Celi et al[60]. This is an additional limitation of this study, but will likely be addressed in future work from our lab that leverages the advancements made in this thesis.

#### **4.4 Future Directions**

Promus Element, on average, proved to be a superior stent in terms of WSS distributions. However, initial studies indicate that not all patients received the optimal DES according to CFD. Local features in the artery can factor into adverse WSS and correlate with NT depending on the DES elution agent. One must determine what specific factors promote the success of one DES compared to another in terms of WSS. Also, if the process described in this thesis could be streamlined, the optimal stent could be determined case by case at bedside.

In order to fully understand the effects of different DES on WSS and NT, studies must be done to determine the relative contribution of the stent geometry and respective elution agent. While keeping either the stent design or elution agent constant, one will be able to hypothesize on the specific effects that each has on NT. This study has the potential to find an optimal pairing of geometric factors and elution agents that could improve the restenosis rate.

## BIBLIOGRAPHY

- [1] A. S. Go, D. Mozaffarian, V. L. Roger, E. J. Benjamin, J. D. Berry, W. B. Borden, D. M. Bravata, S. Dai, E. S. Ford, C. S. Fox, S. Franco, H. J. Fullerton, C. Gillespie, S. M. Hailpern, J. a Heit, V. J. Howard, M. D. Huffman, B. M. Kissela, S. J. Kittner, D. T. Lackland, J. H. Lichtman, L. D. Lisabeth, D. Magid, G. M. Marcus, A. Marelli, D. B. Matchar, D. K. McGuire, E. R. Mohler, C. S. Moy, M. E. Mussolino, G. Nichol, N. P. Paynter, P. J. Schreiner, P. D. Sorlie, J. Stein, T. N. Turan, S. S. Virani, N. D. Wong, D. Woo, and M. B. Turner, “Heart disease and stroke statistics--2013 update: a report from the American Heart Association.,” *Circulation*, vol. 127, no. 1, pp. e6–e245, Jan. 2013.
- [2] N. Westerhof, N. Stergiopulos, and M. Noble, *Snapshot of Hemodynamics*, Second. Springer.
- [3] W. Nichols and M. O’Rourke, *McDonald’s Blood Flow in Arteries: Theoretical, Experimental and Clinical Principles*. London: Hodder Arnold Group, 2005.
- [4] P. W. Serruys, M. J. B. Kutryk, and A. T. L. Ong, “Coronary-artery stents.,” *N. Engl. J. Med.*, vol. 354, no. 5, pp. 483–95, Feb. 2006.
- [5] H. Hamid and J. Coltart, “‘Miracle stents’--a future without restenosis.,” *Mcgill J. Med.*, vol. 10, no. 2, pp. 105–11, Jul. 2007.
- [6] V. Virga, E. Stabile, G. Biamino, L. Salemme, A. Cioppa, G. Giugliano, T. Tesorio, L. Cota, G. Popusoi, A. Pucciarelli, G. Esposito, B. Trimarco, and P. Rubino, “Drug-Eluting Balloons for the Treatment of the Superficial Femoral Artery in Stent Restenosis: 2-Year Follow-up.,” *JACC. Cardiovasc. Interv.*, Mar. 2014.
- [7] S.-Y. Lee, M.-K. Hong, D.-H. Shin, J.-S. Kim, B.-K. Kim, Y.-G. Ko, D. Choi, and Y. Jang, “Mechanisms of Postintervention and Nine-Month Luminal Enlargement After Treatment of Drug-Eluting In-Stent Restenosis With a Drug-Eluting Balloon.,” *Am. J. Cardiol.*, Feb. 2014.
- [8] L. T. Newsome, M. a Kutcher, and R. L. Royster, “Coronary artery stents: Part I. Evolution of percutaneous coronary intervention.,” *Anesth. Analg.*, vol. 107, no. 2, pp. 552–69, Aug. 2008.
- [9] T. Htay and M. W. Liu, “Drug-eluting stent: a review and update.,” *Vasc. Health Risk Manag.*, vol. 1, no. 4, pp. 263–76, Jan. 2005.
- [10] R. Waksman, “Drug-eluting stents,” *Cardiovasc. Radiat. Med.*, vol. 3, no. 3–4, pp. 226–241, Jul. 2002.

- [11] C.-H. Lee, S.-H. Chang, Y.-H. Lin, S.-J. Liu, C.-J. Wang, M.-Y. Hsu, K.-C. Hung, Y.-H. Yeh, W.-J. Chen, I.-C. Hsieh, and M.-S. Wen, "Acceleration of re-endothelialization and inhibition of neointimal formation using hybrid biodegradable nanofibrous rosuvastatin-loaded stents.," *Biomaterials*, vol. 35, no. 15, pp. 4417–27, May 2014.
- [12] D. R. Holmes, D. J. Kereiakes, S. Garg, P. W. Serruys, G. J. Dehmer, S. G. Ellis, D. O. Williams, T. Kimura, and D. J. Moliterno, "Stent thrombosis.," *J. Am. Coll. Cardiol.*, vol. 56, no. 17, pp. 1357–65, Oct. 2010.
- [13] A. V Finn, G. Nakazawa, M. Joner, F. D. Kolodgie, E. K. Mont, H. K. Gold, and R. Virmani, "Vascular responses to drug eluting stents: importance of delayed healing.," *Arterioscler. Thromb. Vasc. Biol.*, vol. 27, no. 7, pp. 1500–10, Jul. 2007.
- [14] S. Tsimikas, "Drug-eluting stents and late adverse clinical outcomes lessons learned, lessons awaited.," *J. Am. Coll. Cardiol.*, vol. 47, no. 10, pp. 2112–5, May 2006.
- [15] G. G. L. Biondi-Zoccai, P. Agostoni, G. M. Sangiorgi, F. Airoldi, J. Cosgrave, A. Chieffo, R. Barbagallo, C. Tamburino, G. Vittori, E. Falchetti, M. Margheri, C. Briguori, E. Remigi, I. Iakovou, and A. Colombo, "Incidence, predictors, and outcomes of coronary dissections left untreated after drug-eluting stent implantation.," *Eur. Heart J.*, vol. 27, no. 5, pp. 540–6, Mar. 2006.
- [16] J. F. Ladisa, L. E. Olson, R. C. Molthen, D. A. Hettrick, P. F. Pratt, M. D. Hardel, J. R. Kersten, D. C. Warltier, P. S. Pagel, F. John, and A. Hettrick, "Alterations in wall shear stress predict sites of neointimal hyperplasia after stent implantation in rabbit iliac arteries," vol. 53226, pp. 2465–2475, 2005.
- [17] D. Katritsis, L. Kaiktsis, A. Chaniotis, J. Pantos, E. P. Efstathopoulos, and V. Marmarelis, "Wall shear stress: theoretical considerations and methods of measurement.," *Prog. Cardiovasc. Dis.*, vol. 49, no. 5, pp. 307–29, 2007.
- [18] F. J. H. Gijzen, F. Migliavacca, S. Schievano, L. Soggi, L. Petrini, A. Thury, J. J. Wentzel, A. F. W. van der Steen, P. W. S. Serruys, and G. Dubini, "Simulation of stent deployment in a realistic human coronary artery.," *Biomed. Eng. Online*, vol. 7, p. 23, Jan. 2008.
- [19] J. J. Wentzel, R. Krams, J. C. H. Schuurbiers, J. a. Oomen, J. Kloet, W. J. van der Giessen, P. W. Serruys, and C. J. Slager, "Relationship Between Neointimal Thickness and Shear Stress After Wallstent Implantation in Human Coronary Arteries," *Circulation*, vol. 103, no. 13, pp. 1740–1745, Apr. 2001.
- [20] C. a Taylor and D. a Steinman, "Image-based modeling of blood flow and vessel wall dynamics: applications, methods and future directions: Sixth International

- Bio-Fluid Mechanics Symposium and Workshop, March 28-30, 2008 Pasadena, California.,” *Ann. Biomed. Eng.*, vol. 38, no. 3, pp. 1188–203, Mar. 2010.
- [21] L. M. Ellwein, H. Otake, T. J. Gundert, B.-K. Koo, T. Shinke, Y. Honda, J. Shite, and J. F. LaDisa, “Optical Coherence Tomography for Patient-specific 3D Artery Reconstruction and Evaluation of Wall Shear Stress in a Left Circumflex Coronary Artery,” *Cardiovasc. Eng. Technol.*, vol. 2, no. 3, pp. 212–227, May 2011.
- [22] B. S. Corp, “Introduction to IVUS Technology Intravascular Ultrasound Clinical Applications.”
- [23] V. Chan and A. Perlas, “Atlas of Ultrasound-Guided Procedures in Interventional Pain Management,” pp. 13–20, 2011.
- [24] S. E. Nissen and P. Yock, “Clinical Cardiology : New Frontiers Intravascular Ultrasound Rationale for Ultrasound Imaging,” 2011.
- [25] G. De Santis, P. Mortier, M. De Beule, P. Segers, P. Verdonck, and B. Verhegghe, “Patient-specific computational fluid dynamics: structured mesh generation from coronary angiography.,” *Med. Biol. Eng. Comput.*, vol. 48, no. 4, pp. 371–80, Apr. 2010.
- [26] L. Goubergrits, E. Wellnhofer, U. Kertzsch, K. Affeld, C. Petz, and H.-C. Hege, “Coronary artery WSS profiling using a geometry reconstruction based on biplane angiography.,” *Ann. Biomed. Eng.*, vol. 37, no. 4, pp. 682–91, Apr. 2009.
- [27] H. Otake, J. Shite, J. Ako, T. Shinke, Y. Tanino, D. Ogasawara, T. Sawada, N. Miyoshi, H. Kato, B.-K. Koo, Y. Honda, P. J. Fitzgerald, and K. Hirata, “Local determinants of thrombus formation following sirolimus-eluting stent implantation assessed by optical coherence tomography.,” *JACC. Cardiovasc. Interv.*, vol. 2, no. 5, pp. 459–66, May 2009.
- [28] C. J. Slager, J. J. Wentzel, J. C. H. Schuurbijs, J. A. F. Oomen, J. Kloet, R. Krams, C. Von Birgelen, W. J. Van Der Giessen, W. Serruys, and P. J. De Feyter, “True 3-Dimensional Reconstruction of Coronary Arteries in,” 2000.
- [29] K. Fujii, S. G. Carlier, G. S. Mintz, W. Wijns, A. Colombo, D. Böse, R. Erbel, J. de Ribamar Costa, M. Kimura, K. Sano, R. a Costa, J. Lui, G. W. Stone, J. W. Moses, and M. B. Leon, “Association of plaque characterization by intravascular ultrasound virtual histology and arterial remodeling.,” *Am. J. Cardiol.*, vol. 96, no. 11, pp. 1476–83, Dec. 2005.
- [30] A. Hirohata, K. Yamamoto, Y. Imai, K. Senoh, E. Hirose, Y. Kobayashi, H. Takafuji, F. Sano, M. Ohara, K. Ohkawa, Y. Toyama, K. Nosaka, J. Yoshida, Y. Iino, and T. Ohe, “AS-062 Comparison of Coronary Plaque Characterization by

- Spectral Radiofrequency of Intravascular Ultrasound Signals (VH-IVUS and i-MAP),” *Am. J. Cardiol.*, vol. 107, no. 8, p. 24A–25A, Apr. 2011.
- [31] P. Barlis and J. M. Schmitt, “Current and future developments in intracoronary optical coherence tomography imaging,” *EuroIntervention*, vol. 4, no. 4, pp. 529–33, Jan. 2009.
- [32] J. Dijkstra, G. Koning, and J. H. Reiber, “Quantitative measurements in IVUS images,” *Int. J. Card. Imaging*, vol. 15, no. 6, pp. 513–22, Dec. 1999.
- [33] M. L. Gabriele, G. Wollstein, H. Ishikawa, L. Kagemann, J. Xu, L. S. Folio, and J. S. Schuman, “Optical coherence tomography: history, current status, and laboratory work,” *Invest. Ophthalmol. Vis. Sci.*, vol. 52, no. 5, pp. 2425–36, Apr. 2011.
- [34] T. J. Gundert, R. J. Dholakia, D. McMahon, and J. John F. LaDisa, “Computational Fluid Dynamics Evaluation of Equivalency in Hemodynamic Alterations Between Driver, Integrity, and Similar Stents Implanted Into an Idealized Coronary Artery,” *J. Med. Device.*, 2013.
- [35] B. T. Tang, C. P. Cheng, M. T. Draney, N. M. Wilson, P. S. Tsao, R. J. Herfkens, C. A. Taylor, and T. Beverly, “Abdominal aortic hemodynamics in young healthy adults at rest and during lower limb exercise : quantification using image-based computer modeling,” vol. 5431, pp. 668–676, 2006.
- [36] Y. Otsuka, S. Saito, M. Nakamura, H. Shuto, and K. Mitsudo, “Comparison of pharmacokinetics of the limus-eluting stents in Japanese patients,” *Catheter. Cardiovasc. Interv.*, vol. 78, no. 7, pp. 1078–85, Dec. 2011.
- [37] T. J. Gundert, A. L. Marsden, W. Yang, D. S. Marks, and J. F. LaDisa, “Identification of hemodynamically optimal coronary stent designs based on vessel caliber,” *IEEE Trans. Biomed. Eng.*, vol. 59, no. 7, pp. 1992–2002, Jul. 2012.
- [38] R.-J. van Geuns, C. Tamburino, J. Fajadet, M. Vrolix, B. Witzenbichler, E. Eeckhout, C. Spaulding, K. Reczuch, A. La Manna, R. Spaargaren, H. M. García-García, E. Regar, D. Capodanno, G. Van Langenhove, and S. Verhey, “Self-expanding versus balloon-expandable stents in acute myocardial infarction: results from the APPOSITION II study: self-expanding stents in ST-segment elevation myocardial infarction,” *JACC. Cardiovasc. Interv.*, vol. 5, no. 12, pp. 1209–19, Dec. 2012.
- [39] F. J. H. Gijssen, R. M. Oortman, J. J. Wentzel, J. C. H. Schuurbiens, K. Tanabe, M. Degertekin, J. M. Ligthart, A. Thury, P. J. de Feyter, P. W. Serruys, and C. J. Slager, “Usefulness of shear stress pattern in predicting neointima distribution in sirolimus-eluting stents in coronary arteries,” *Am. J. Cardiol.*, vol. 92, no. 11, pp. 1325–1328, Dec. 2003.

- [40] N. Suzuki, H. Nanda, D. J. Angiolillo, H. Bezerra, M. Sabaté, P. Jiménez-Quevedo, F. Alfonso, C. Macaya, T. a Bass, O. J. Ilegbusi, and M. a Costa, "Assessment of potential relationship between wall shear stress and arterial wall response after bare metal stent and sirolimus-eluting stent implantation in patients with diabetes mellitus.," *Int. J. Cardiovasc. Imaging*, vol. 24, no. 4, pp. 357–64, Apr. 2008.
- [41] M. I. Papafaklis, C. V Bourantas, P. E. Theodorakis, C. S. Katsouras, K. K. Naka, D. I. Fotiadis, and L. K. Michalis, "The effect of shear stress on neointimal response following sirolimus- and paclitaxel-eluting stent implantation compared with bare-metal stents in humans.," *JACC. Cardiovasc. Interv.*, vol. 3, no. 11, pp. 1181–9, Nov. 2010.
- [42] S. Abbara, A. Arbab-Zadeh, T. Q. Callister, M. Y. Desai, W. Mamuya, L. Thomson, and W. G. Weigold, "SCCT guidelines for performance of coronary computed tomographic angiography: a report of the Society of Cardiovascular Computed Tomography Guidelines Committee.," *J. Cardiovasc. Comput. Tomogr.*, vol. 3, no. 3, pp. 190–204, 2009.
- [43] L. Antiga and D. a Steinman, "Robust and objective decomposition and mapping of bifurcating vessels.," *IEEE Trans. Med. Imaging*, vol. 23, no. 6, pp. 704–13, Jun. 2004.
- [44] T. J. Gundert, S. C. Shadden, A. R. Williams, B.-K. Koo, J. a Feinstein, and J. F. Ladisa, "A rapid and computationally inexpensive method to virtually implant current and next-generation stents into subject-specific computational fluid dynamics models.," *Ann. Biomed. Eng.*, vol. 39, no. 5, pp. 1423–37, May 2011.
- [45] J. F. LaDisa, D. a Hettrick, L. E. Olson, I. Guler, E. R. Gross, T. T. Kress, J. R. Kersten, D. C. Warltier, and P. S. Pagel, "Stent implantation alters coronary artery hemodynamics and wall shear stress during maximal vasodilation.," *J. Appl. Physiol.*, vol. 93, no. 6, pp. 1939–46, Dec. 2002.
- [46] J. F. LaDisa, Jr., I. Guler, L. E. Olson, D. a. Hettrick, J. R. Kersten, D. C. Warltier, and P. S. Pagel, "Three-Dimensional Computational Fluid Dynamics Modeling of Alterations in Coronary Wall Shear Stress Produced by Stent Implantation," *Ann. Biomed. Eng.*, vol. 31, no. 8, pp. 972–980, Sep. 2003.
- [47] J. F. LaDisa, L. E. Olson, I. Guler, D. a Hettrick, S. H. Audi, J. R. Kersten, D. C. Warltier, and P. S. Pagel, "Stent design properties and deployment ratio influence indexes of wall shear stress: a three-dimensional computational fluid dynamics investigation within a normal artery.," *J. Appl. Physiol.*, vol. 97, no. 1, pp. 424–30; discussion 416, Jul. 2004.
- [48] J. F. Ladisa, L. E. Olson, I. Guler, D. A. Hettrick, J. R. Kersten, D. C. Warltier, P. S. Pagel, F. John, and A. Douglas, "Circumferential vascular deformation after



stent implantation alters wall shear stress evaluated with time-dependent 3D computational fluid dynamics models,” vol. 53226, pp. 947–957, 2005.

- [49] A. R. Williams, B.-K. Koo, T. J. Gundert, P. J. Fitzgerald, and J. F. LaDisa, “Local hemodynamic changes caused by main branch stent implantation and subsequent virtual side branch balloon angioplasty in a representative coronary bifurcation,” *J. Appl. Physiol.*, vol. 109, no. 2, pp. 532–40, Aug. 2010.
- [50] D. M. Leaman, R. W. Brower, G. T. Meester, P. Serruys, and M. van den Brand, “Coronary artery atherosclerosis: severity of the disease, severity of angina pectoris and compromised left ventricular function,” *Circulation*, vol. 63, no. 2, pp. 285–299, Feb. 1981.
- [51] G. a Van Huis, P. Sipkema, and N. Westerhof, “Coronary input impedance during cardiac cycle as determined by impulse response method,” *Am. J. Physiol.*, vol. 253, no. 2 Pt 2, pp. H317–24, Aug. 1987.
- [52] B. S. Gow and C. D. Hadfield, “The elasticity of canine and human coronary arteries with reference to postmortem changes,” *Circ. Res.*, vol. 45, no. 5, pp. 588–594, Nov. 1979.
- [53] N. Stergiopoulos, J. J. Meister, and N. Westerhof, “Simple and accurate way for estimating total and segmental arterial compliance: the pulse pressure method,” *Ann. Biomed. Eng.*, vol. 22, no. 4, pp. 392–7, 1994.
- [54] N. Stergiopoulos, P. Segers, and N. Westerhof, “Use of pulse pressure method for estimating total arterial compliance in vivo,” *Am. J. Physiol.*, vol. 276, no. 2 Pt 2, pp. H424–8, Feb. 1999.
- [55] A. M. Malek and S. L. Alper, “Hemodynamic Shear Stress and Its Role in Atherosclerosis,” vol. 282, no. 21, pp. 2035–2042, 2014.
- [56] J. J. Wentzel and F. J. H. Gijsen, “The influence of shear stress on in-stent restenosis and thrombosis,” 2008.
- [57] J. R. Sindermann, V. Verin, J. W. Hopewell, H. P. Rodemann, and J. H. Hendry, “Biological aspects of radiation and drug-eluting stents for the prevention of restenosis,” *Cardiovasc. Res.*, vol. 63, no. 1, pp. 22–30, Jul. 2004.
- [58] N. Oshiro, K. Yoshino, S. Hidayat, C. Tokunaga, K. Hara, S. Eguchi, J. Avruch, and K. Yonezawa, “Dissociation of raptor from mTOR is a mechanism of rapamycin-induced inhibition of mTOR function,” *Genes Cells*, vol. 9, no. 4, pp. 359–66, Apr. 2004.
- [59] H. Hagiwara, M. Sasaki, Y. Hiraishi, H. Terao, J. Kimura, and K. Inoue, “Vascular Responses To a Newly Developed Coronary Stent (Nobori) Coated With the

Bioabsorbable Polymer, Polylactic Acid and Biolimus a9,” *J. Am. Coll. Cardiol.*, vol. 55, no. 10, p. A194.E1811, Mar. 2010.

- [60] S. Celi, M. Vagheti, C. Palmieri, and S. Berti, “Superficial coronary calcium analysis by OCT: Looking forward an imaging algorithm for an automatic 3D quantification,” *Int. J. Cardiol.*, vol. 168, no. 3, pp. 2958–60, Oct. 2013.

## Appendix

**1. Initial Programs and Set-Up**

- a. The following arrangement of directories and programs should be used for all cases, both post-stenting and follow-up. This arrangement can also be seen in the demo files in the Code Repository.

Post (or follow-up)

→ mLCX – This directory contains the surface and centerline points from CT data found using the instructions in the documents Master\_Simulation\_Document.doc and Steps\_to\_Segmenting.doc created by Laura Ellwein.

→ Post

adjacency\_blkdiag.m

advanced\_dijkstra.m

calculate\_regionprops.m

circum\_interpolate\_fixed.m

dat2jpg.m

find\_pathpoints.m

func\_Write\_Axial\_Spline\_VTP.m

isolate\_image\_contours.m

isolate\_image\_contours\_green\_purple.m

jpg2dat.m

LCX\_csa.m

masking\_extras.m

masking\_extras\_AB.m  
OCT\_group\_content\_creator.m  
OCT\_path\_creator.m  
OCT\_segment\_creator.m  
OCT\_segment\_creator\_smooth.m  
pixel\_sorter.m  
plotpoints.m  
point\_order.m  
refine\_transducer.m  
refined\_shortest\_path.m  
rotate\_dist\_prox\_slices.m  
rotate\_OCT\_slices.m  
rotate\_OCT\_slices\_trans.m  
rotate\_OCT\_slices\_trans\_final.m (follow-up only)  
rotate\_refined\_transducer.m  
save\_normals\_points.m  
shortest\_path\_dijkstra\_method.m  
testABmask.m  
TRACE\_MooreNeighbourhood.m  
trans\_interp.m

→ Post\_Stent

calculate\_regionprops.m  
isolate\_image\_contours.m

isolate\_image\_contours\_green\_purple.m

masking\_extras.m

OCT\_group\_content\_creator.m

OCT\_path\_creator.m

OCT\_segment\_creator.m

OCT\_segment\_creator\_smooth.m

pixel\_sorter.m

point\_order.m

rotate\_OCT\_slices\_trans.m

truncate.m

b. **Program:** *simvas\_shift.m*

- i. **Function:** The coordinate system in Simvascular coincides with that of VolView, using an image origin at (0,0,0); however ITK-Snap uses the NIFTI coordinate system to save meshes, and likewise the centerline generated from VMTK will be in this same coordinate system. Therefore a coordinate shift is used to convert between NIFTI and “Simvascular” coordinates.
- ii. **Input:** Size and spacing of DICOM image sequence can be found in Volview (Figure 41). Superior image position can be found by first opening the image sequence using ImageJ (Figure 42). Scroll to the most superior image and open the image info (ctrl+I) and scroll to “Image Position (Patient) Field (0020,0032)”. All the

mentioned parameters are input into the pop-up GUI when the program is run.

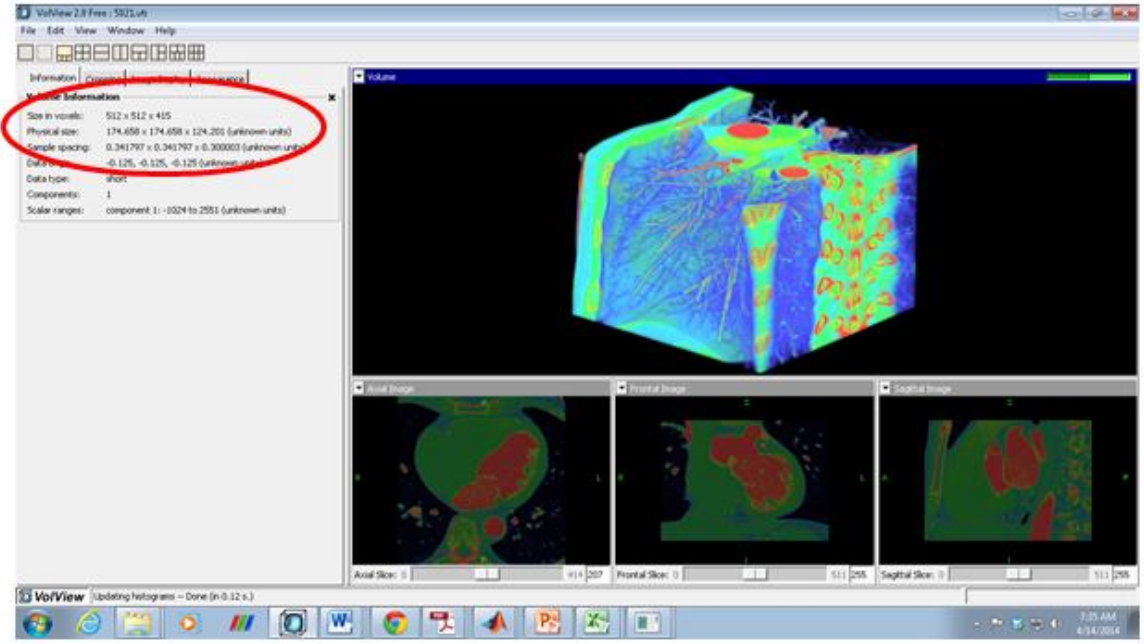


Figure 41: 3D volume in Volview showing the size in voxels and image spacing.

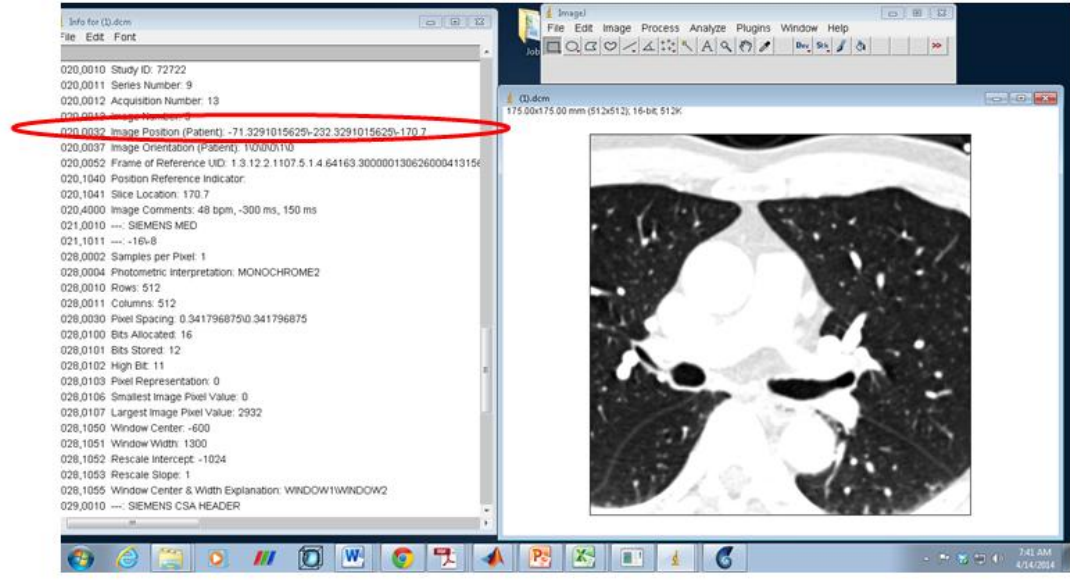


Figure 42: Using ImageJ, determine the Image Position for the most superior image.

- iii. **Output:** Xshift, Yshift, and Zshift are displayed in the Matlab command window (Figure 43).



```

Command Window
xshift =
    2.3940625000000000e+02

yshift =
    2.3940625000000000e+02

zshift =
    33.4750000000000001

```

Figure 43: X, Y, and Z shifts output in Matlab.

## 2. OCT Image Processing

The following programs should be run for the post-stenting and follow-up cases.

a. **Program:** *isolate\_image\_contours.m*

- i. **Function:** Isolates the lumen or stent contours from a series of .jpg images. Make sure the program is isolating the correct contour (lumen or stent). If it is not, select the correct *isolate\_image\_contours.m*. The programs are separated by which color contour they isolate.
- ii. **Input:** The following parameters should be inserted into the pop-up GUI: starting number of the .jpg images, threshold for converting to binary lumen images, and if the program should show the original image. Segment matrix should correspond to the

range and interval of the OCT image series (This will be the same throughout the entire case). A representation of the segment matrix can be seen in Figure 44. Also, at line 48, the name of the images being loaded should match the header of the OCT images as seen below.

```

46 - for i = 1:num_im
47 -     ni = num2str(segment(i));
48 -     eval(['im_slice' ni '=imread('Frame ' ni ' of #4PL post KBT.jpg')']);
49 - end

```

OCT Image Directory:

Name	Date modified	Type	Size
Frame 141 of #4PL post KBT.jpg	7/19/2013 12:52 PM	JPEG image	75 KB
Frame 151 of #4PL post KBT.jpg	7/19/2013 12:52 PM	JPEG image	77 KB
Frame 161 of #4PL post KBT.jpg	7/19/2013 12:52 PM	JPEG image	83 KB
Frame 171 of #4PL post KBT.jpg	7/19/2013 12:53 PM	JPEG image	82 KB
Frame 181 of #4PL post KBT.jpg	7/19/2013 12:53 PM	JPEG image	83 KB
Frame 191 of #4PL post KBT.jpg	7/19/2013 12:53 PM	JPEG image	82 KB
Frame 201 of #4PL post KBT.jpg	7/19/2013 12:54 PM	JPEG image	86 KB
Frame 211 of #4PL post KBT.jpg	7/19/2013 12:54 PM	JPEG image	84 KB
Frame 221 of #4PL post KBT.jpg	7/19/2013 12:54 PM	JPEG image	81 KB
Frame 231 of #4PL post KBT.jpg	7/19/2013 12:54 PM	JPEG image	79 KB
Frame 241 of #4PL post KBT.jpg	7/19/2013 12:55 PM	JPEG image	79 KB
Frame 251 of #4PL post KBT.jpg	7/19/2013 12:55 PM	JPEG image	77 KB
Frame 261 of #4PL post KBT.jpg	7/19/2013 12:55 PM	JPEG image	80 KB
Frame 271 of #4PL post KBT.jpg	7/19/2013 12:55 PM	JPEG image	83 KB
Frame 281 of #4PL post KBT.jpg	7/19/2013 12:56 PM	JPEG image	82 KB
Frame 291 of #4PL post KBT.jpg	7/19/2013 12:56 PM	JPEG image	84 KB
Frame 301 of #4PL post KBT.jpg	7/19/2013 12:56 PM	JPEG image	85 KB
Frame 311 of #4PL post KBT.jpg	7/19/2013 12:57 PM	JPEG image	77 KB
Frame 321 of #4PL post KBT.jpg	7/19/2013 12:57 PM	JPEG image	75 KB
Frame 331 of #4PL post KBT.jpg	7/19/2013 12:57 PM	JPEG image	75 KB
Frame 341 of #4PL post KBT.jpg	7/19/2013 12:57 PM	JPEG image	74 KB
Frame 351 of #4PL post KBT.jpg	7/19/2013 12:58 PM	JPEG image	73 KB

Segment Matrix: [141 151 161 171 181 191 201 211 221 231 241 251 261 271 281 291 301 311 321 333 341 351]

Figure 44: Naming the slice and creating the segment matrix.

iii. **Output:** Each resulting image is saved as

'lumen\_segs\lumen#.dat', with the # referring to the slice number.



b. **Program:** *masking\_extras.m*

- i. **Function:** Masks over all of the unwanted parts of the images, including headers, footers, and measurement markings.
- ii. **Input:** Segment matrix should correspond to the range and interval of the OCT image series as previously described.
- iii. **Output:** Each resulting image is saved as the file 'masked\_segs\masked#.dat'.

c. **Program:** *dat2jpg.m*

- i. **Function:** Convert 'masked\_segs\masked#.dat' to 'masked\_segs\masked#.jpg'. Check image to make sure that all unwanted parts of image are removed. Also, make sure that the contour is completely filled. If not, manually edit in paint.
- ii. **Input:** Segment matrix should correspond to the range and interval of the OCT image series as previously described.
- iii. **Output:** Each resulting image is saved as the file 'masked\_segs\masked#.jpg'.

d. **Program:** *jpg2dat.m*

- i. **Function:** Convert edited 'masked\_segs\masked#.jpg' to 'masked\_segs\masked#.dat'.
- ii. **Input:** Segment matrix should correspond to the range and interval of the OCT image series as previously described.

- iii. **Output:** Each resulting image is saved as the file  
 ‘masked\_segs\masked#.dat’.

e. **Program:** *point\_order.m*

- i. **Function:** This program orders the points on the boundary of the filled contour delineated by the segment. Determines the centroid of the filled segment and converts all pixels to xyz coordinates. Note that *TRACE\_MooreNeighbourhood.m* must be in the ‘masked\_segs’ directory.
- ii. **Input:** An even multiple of four that will equal the number of circumferential resolution and the number of millimeters per x and y pixel (determined from ImageJ). Also, the segment matrix is the same as previous programs. If the OCT image has an anomaly (dissection, overlapping tissue, etc.) change the contour being saved to ‘vesseln\_one#’ instead of ‘vesseln\_sparse#’ as seen in Figure 45.

```

96 - for i = 1:num_im $incerblength
97 -     ni = num2str(segment(i));
98 -     eval(['save contour_' ni '.dat vesseln_sparse' ni ' -ascii'])
99 -     eval(['save center_' ni '.dat centroid_' ni ' -ascii'])
100 - end

96 - for i = 1:num_im $incerblength
97 -     ni = num2str(segment(i));
98 -     eval(['save contour_' ni '.dat vesseln_one' ni ' -ascii'])
99 -     eval(['save center_' ni '.dat centroid_' ni ' -ascii'])
100 - end

```

Figure 45: Saving the ‘vesseln\_sparse’ or ‘vesseln\_one’, depending if the image has an anomaly.

If you incur an error when lofting the segments in Simvascular, you must decrease the amount of points in the segment by adjusting the circled value below in ‘vessel\_sparse#’ (Figure 46) and save the contour using the adjusted ‘vessel\_sparse#’. The circled value can range from 2-8 (higher value corresponds to fewer points being saved).

```
while k<eval(['length(vesseln_one' ni ' ')]
    eval(['vesseln_sparse' ni ' ((k-1),8+1,:)=vesseln_one' ni ' (k,:);'])
    k=k-8;
end
```

Figure 46: Adjusting the number of points being saved for a contour.

- iii. **Output:** Each resulting contour is saved as the file ‘contours\_centers/contour\_#.dat’ and ‘contours\_centers/center\_#.dat’ and plotted (Figure 47).

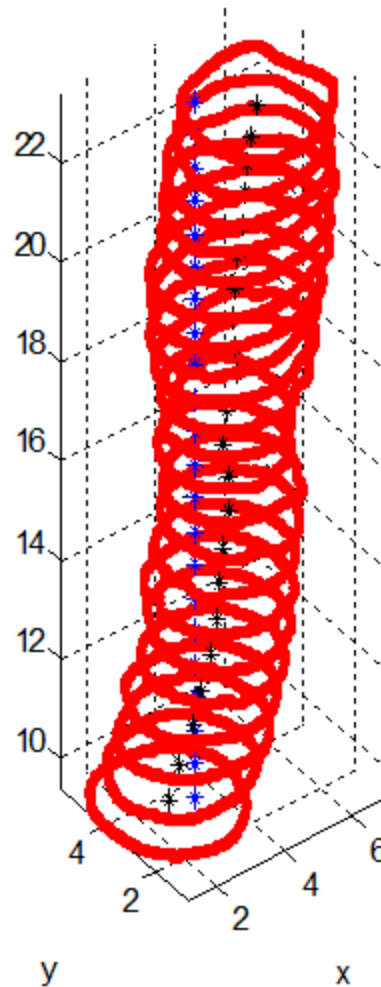


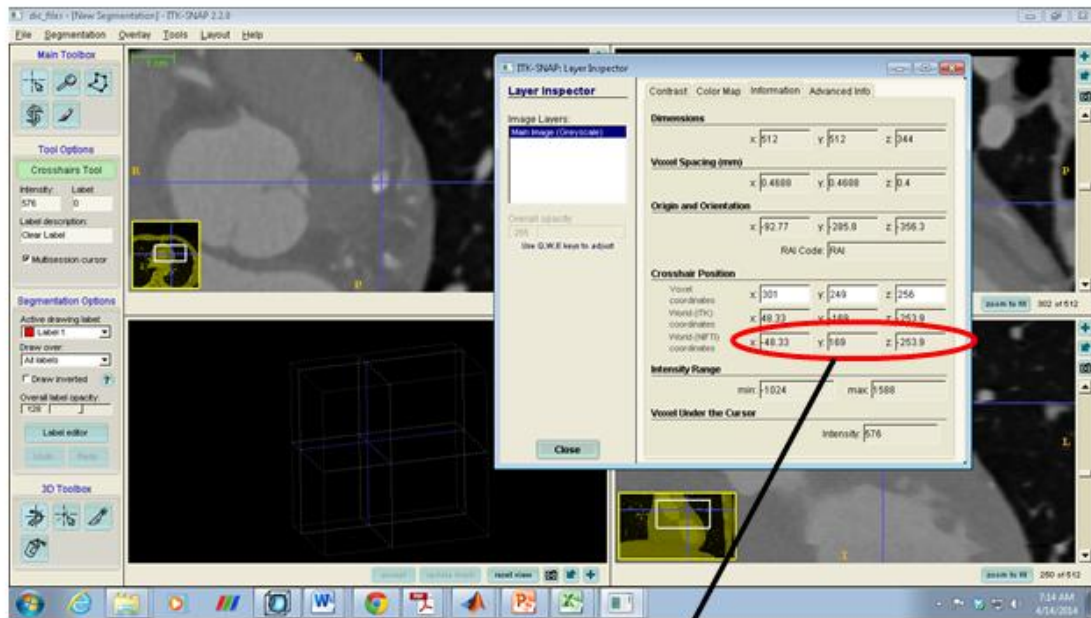
Figure 47: Illustrating the X, Y, and Z coordinates of contours.

### 3. Vessel Reconstruction

- a. **Overview:** The following programs are used to reconstruct the stented coronary arteries using OCT images. This series of vessel reconstruction programs should be ran for post-stenting and follow-up cases. Before running these programs, the vessel surface and centerline should be found using the instructions in the document Master\_Simulation\_Document.doc and Steps\_to\_Segmenting.doc created by Laura Ellwein. These programs

must be run in order, as the inputs for the programs are the outputs of the programs run before it.

- b. **Program:** *find\_pathpoints.m (Option 1)*
  - i. **Function:** This script determines the points at which slices are located, both initially on the centerline and finally on the transducer path. Distances between data centerline points are calculated and saved in a vector. A vector of cumulative distances is created. These points are interpolated to 0.1mm distances and saved in 'new\_cl.dat'.
  - ii. **Input:** The centerline and surface from CT are loaded. Make sure that the directories are consistent when loading these files. 'Tript' (distal) and 'Branchpt'(proximal) are the two landmarks. These points are determined from ITK-Snap (Figure 48).



```

45
46 -   tript=[-48.33 170.5 -254.3];
47 -   branchpt=[-34.27 156.4 -243.9];
48

```

Figure 48: Determining the landmark positions in ITK-Snap and inserting them into Matlab.

“reg\_points” is a matrix of 3 columns and X amount of rows where X is the number of OCT images. Next, “reg\_points(Y,:)=new\_xyz(tri\_id,:)” and “reg\_points(Z,:)=new\_xyz(branch\_id,:)” are set where Y and Z are the numbers of the OCT images (in series) at the distal and proximal landmarks, respectively (Figure 49). “tri2branch\_dist” is the distance between the two landmarks. “dist2slice\_ratio” is the “tri2branch\_dist” divided by the number of OCT images in between the two landmark images. “start\_dist” is the distal landmark position minus the number of images before the distal

landmark multiplied by the “dist2slice\_ratio”.

“start\_dist2slice\_ratio” is the “start2tri\_dist” divided by the number of OCT images before the distal landmark image. Please reference the Figure 50 for an example of how to set up the aforementioned matrices.

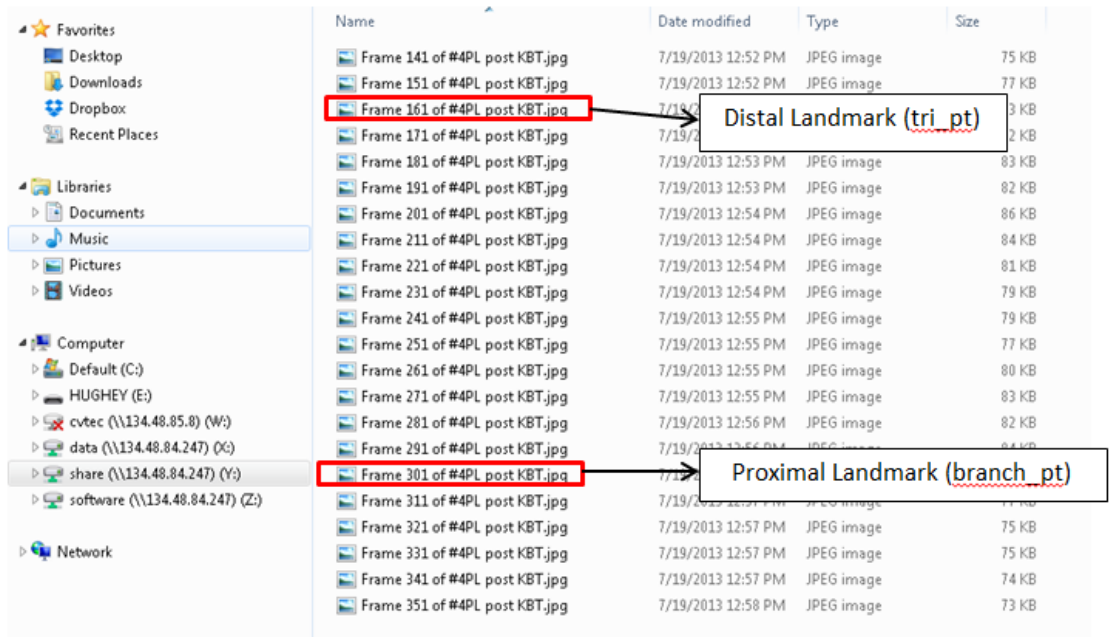


Figure 49: Determining which OCT images correspond to the landmark positions.

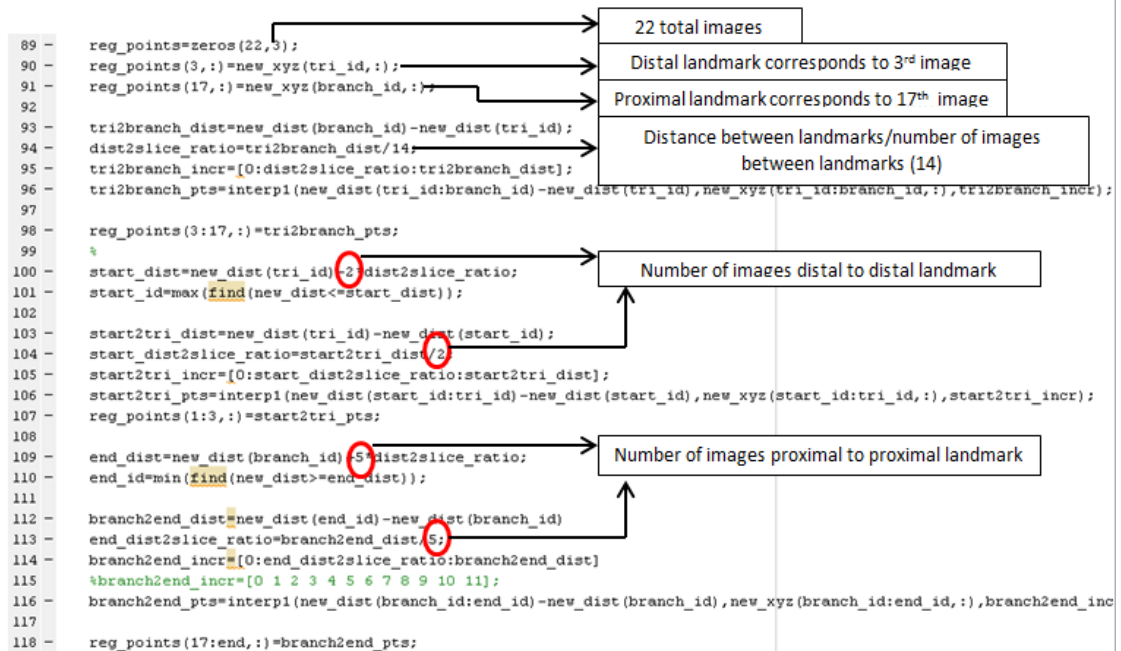


Figure 50: Creating the matrices for `find_pathpoints.m`.

iii. **Output:** Locations are saved as “`reg_points.dat`”. Points are interpolated to 4mm to establish locations for transducer candidate point locations, saved in “`path_points4.dat`”. These are located distal and proximal to the stented region.

c. **Program:** `LCX_csa.m` (Option 1)

- i. **Function:** Finds the cross-sectional area at each of the points “`new_cl.dat`”, the 0.1 mm interpolation of points. This program reads in data files from the vessel surface and centerline points, and calculates the corresponding cross-sectional area.
- ii. **Input:** Select the stented region in the GUI. The centerline and surface from CT are loaded. Make sure that the directories are



consistent when loading these files (i.e set-up of directories is exactly like the example previously shown).

- iii. **Output:** Cross-sectional area from the vessel surface and centerline points within the stented region.

d. **Program:** *rotate\_OCT\_slices.m*

- i. **Function:** Rotates the slices so they are positioned on the centerline of the vessel at each of the points “reg\_points.dat”. The rotational matrices are found which would rotate the centerline parallel with the vector [0,0,1]. These are applied in the reverse direction to the slices thus registering them in 3D on the centerline. To find the candidate points for the transducer, first the transducer locations for the two landmarks are estimated from ITK-Snap. For all other segments, candidate points for the transducer location are chosen – 13 points equally spaced around the centerline at a radius equal to the distance between the transducer and centroid. Finally, the upper left hand corner is tracked.
- ii. **Input:** The segment matrix is the same as previous programs. The mm/pixel calibration needs to be inserted at the lines calculating the “new\_transducer” and “new\_ul” as seen in Figure 51. This value should be the same value used in *point\_order.m*.

```

63 - | eval(['new_transducer=[352*0.01, 352*0.01, 0]-[center_' ns ' 0]'';'] ) |
64 - | eval(['new_ul=[1*0.01, 1*0.01, 0]-[center_' ns ' 0]'';'] ) % ADDED

```

Figure 51: Adding the mm/pixel ratio.

For the landmark positions, candidate points from ITK-Snap and their corresponding OCT image number (in series) must be inserted as seen in Figure 52.

```

84 - | if p==3 → Distal landmark corresponds to 3rd image
85 - |   for ap=1:angpts
86 - |     eval(['transducer_candidates_' ns '(ap,)' '-11.91 159.2 -234.9;'])
87 - |   end
88 - | elseif p==17 → Proximal landmark corresponds to 17th
89 - |   for ap=1:angpts
90 - |     eval(['transducer_candidates_' ns '(ap,)' '-1.78 170.1 -235.5;'])
91 - |   end
92 - | else
93 - |   for ap=1:angpts%+1
94 - |     eval(['transducer_candidates_' ns '(ap,)=inv(trans_matrix1)*inv(trans_matrix2)*transducer_temps_' ns '(ap,)' '+pa
95 - |   end
96 - | end

```

Figure 52: Setting the candidate points (circled) for the landmark positions.

- iii. **Output:** Transducer candidate points are saved as “transducer\_candidates\transducer\_candidates\_#.dat”. The upper left hand corner points are saved as “real\_ul\real\_ul\_#.dat”.

e. **Program:** *LCX\_csa.m* (Option 2)

- i. **Function:** Finds the cross-sectional area and resulting average radius at each of the points ‘path\_points4.dat’, spaced 4 mm apart distal and proximal to the stented region. The radius is used to find candidate points for the transducer location, 4 points equally spaced at 1/3 radius away from the centerline, and 8 points equally

spaced  $2/3$  radius away from the centerline. Center point is included as well for a total of 13 points. Candidate points saved in 'distal\_proximal\dist\_prox\_#.dat'.

- ii. **Input:** Select the distal/proximal region in the GUI. The centerline and surface from CT are loaded. Cross-sectional area and resulting average radius at each of the points 'path\_points4.dat' is determined.
  - iii. **Output:** 'Distal\_proximal' directory is created. Candidate points are saved in this directory as 'dist\_prox\_#.dat'.
- f. **Program:** *rotate\_dist\_prox\_slices.m*
- i. **Function:** Rotates the 2D transducer candidate points 'dis\_prox\_#.dat' into the vessel to create 3D transducer candidate points distal and proximal to the stented region.
  - ii. **Input:** The surface points from CT are loaded. Centerline ('new\_cl.dat') and center path points ('path\_points4.dat') are loaded. 3D transducer candidate points are created using the candidate points ('dist\_prox\_#.dat') from *LCX\_csa.m*.
  - iii. **Output:** 3D transducer candidate points are saved as 'distal\_proximal\dist\_prox\_candidates\_#.dat' and plotted as seen in Figure 53.

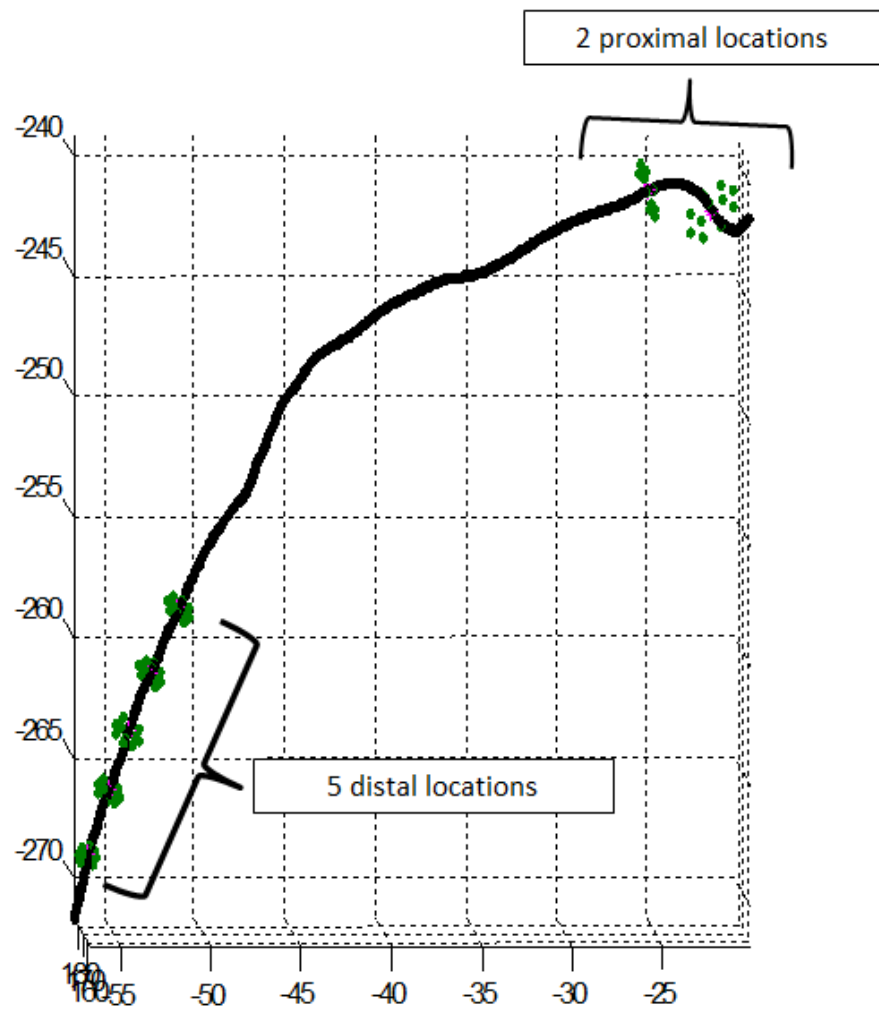


Figure 53: Transducer candidate points for the proximal and distal regions.

g. **Program:** *shortest\_path\_dijkstra\_method.m*

- i. **Function:** Determine the path of minimum bending energy through the candidate points using a shortest path algorithm, Dijkstra's algorithm.
- ii. **Input:** The segment matrix is the same as previous programs. For the distal region, determine the number of locations and set 'n' in

the for loop to '1:number of locations'. Perform this same step for the proximal region and set 'n' accordingly. The following example in Figure 54 corresponds to Figure 53 (5 distal locations and 2 proximal locations).

```

31 - cd distal_proximal
32 - for n=1:5 → 5 distal locations
33 -     nn=num2str(n);
34 -     eval(['load dist_prox_candidates_' nn '.dat;'])
35 -     eval(['slice_array=cat(3,slice_array,dist_prox_candidates_' nn ');'])
36 - end
37 - cd ../transducer_candidates
38 - for p=1:length(segment)
39 -     s=segment(p); ns=num2str(s);
40 -     eval(['load transducer_candidates_' ns '.dat;'])
41 -     eval(['slice_array=cat(3,slice_array,transducer_candidates_' ns ');'])
42 -     % pause
43 - end
44 - cd ../distal_proximal
45 - for n=6:7 → 2 proximal locations
46 -     nn=num2str(n);
47 -     eval(['load dist_prox_candidates_' nn '.dat;'])
48 -     eval(['slice_array=cat(3,slice_array,dist_prox_candidates_' nn ');'])
49 - end
50 - cd ..

```

Figure 54: Setting up for-loops to properly determine transducer pathway.

- iii. **Output:** Saves the candidate transducer points at a 0 degree offset from the original transducer location ('trans\_start\_ang0.dat') and the final transducer points ('final\_transducer\_points.dat').
- h. **Program:** *find\_pathpoints.m* (Option 2)
  - i. **Function:** Interpolates the points found in the shortest path algorithm to 0.1mm and finds points spaced ~1mm apart. This distance is approximate, because as with option 1, slices between landmarks are then placed equally spaced on the centerline. This spacing is used to place slices distal and proximal to the region

between landmarks. Results are saved in 'trans\_interp\_pts.dat' and 'reg\_points\_trans.dat'.

ii. **Input:** The centerline and surface from CT are loaded. Landmark positions are the same from *find\_pathpoints.m* (Option 1). Loads the transducer points from 'trans\_interp\_pts.dat'.

iii. **Output:** Program automatically saves 'trans\_interp\_pts.dat' and 'reg\_points\_trans.dat'.

i. **Program:** *refine\_transducer.m*

i. **Function:** Adapted from *LCX\_csa.m*. Finds 12 new points around each point in 'reg\_points\_trans.dat' according to a radius of 1.1 mm. The radius is used to find candidate points for the transducer location, 4 points equally spaced at 1/3 radius away from the centerline, and 8 points equally spaced 2/3 radius away from the centerline. Center point is included as well for a total of 13 points. Candidate points saved in 'refined\_transducer\refined\_transducer\_#.dat'.

ii. **Input:** The centerline and surface from CT are loaded. 'Trans\_interp\_pts.dat' and 'trans\_start\_ang0.dat' are loaded. 'Refined\_transducer' directory is created.

iii. **Output:** Refined candidate points are saved in the newly created 'refined\_transducer' directory as 'refined\_transducer\_#.dat'.

j. **Program:** *rotate\_refined\_transducer.m*

- i. **Function:** Similar to *rotate\_dist\_prox\_slices.m*, except that it now applies rotations from 2D to 3D for the ‘refined\_transducer\_#.dat’ points from *refine\_transducer.m*.
  - ii. **Input:** The surface data from CT is loaded. ‘Trans\_interp\_pts.dat’ and ‘trans\_start\_ang0.dat’ are loaded.
  - iii. **Output:** Output files are saved in the ‘refined\_transducer’ directory as ‘refined\_transducer\_candidates\_#.dat’.
- k. **Program:** *refined\_shortest\_path.m*
  - i. **Function:** Similar to *shortest\_path\_dijkstra\_method.m*, but now uses ‘refined\_transducer\_candidates\_#.dat’ from *rotate\_refined\_transducer.m*.
  - ii. **Input:** The segment matrix is the same as previous programs. In the first for loop, ‘n’ must go from 1 to the total number of refined transducer candidate files in the ‘refined\_transducer’ directory. Program loads in the ‘refined\_transducer\_candidates\_#.dat’ from the ‘refined\_transducer’ directory.
  - iii. **Output:** Shortest path points are saved in ‘refined\_trans\_start.dat’.
- l. **Program:** *find\_pathpoints.m (Option 3)*
  - i. **Function:** Interpolates the points found in the shortest path algorithm to 0.1mm and finds points spaced ~1mm apart. This distance is approximate, because as with option 1, slices between landmarks are then placed equally spaced on the centerline. This

spacing is used to place slices distal and proximal to the region between landmarks.

- ii. **Input:** The centerline and surface from CT are loaded. Landmark positions are the same from *find\_pathpoints.m* (Option 1 and 2). Loads the transducer points from 'refined\_trans\_start.dat'.
- iii. **Output:** Program automatically writes over 'trans\_interp\_pts.dat' and 'reg\_points\_trans.dat'.

m. **Program:** *rotate\_OCT\_slices\_trans.m*

- i. **Function:** Rotates the slices so they are now positioned on the transducer path of the LCX at each of the points 'reg\_points\_trans.dat'. The rotational matrices are found which would rotate the transducer to be parallel with the vector [0,0,1]. These are applied in the reverse direction to the slices thus registering them in 3D on the transducer. In the final step, the contour is rotated within the orthogonal plane such that the transducer point, the centroid, and the point of intersection between the centerline and the orthogonal plane align with each other.
- ii. **Input:** The surface data from CT is loaded. The segment matrix is the same as previous programs. The program loads 'trans\_interp\_pts.dat', 'trans\_start\_ang0.dat' and 'new\_cl.dat'. Coordinate shifts found previously are set as the 'Xshift', 'Yshift', and 'Zshift', respectively.



- iii. **Output:** The directories 'final\_slice\_points', 'projected\_center' and 'final\_center' are created. Segments are saved in 'final\_slice\_points\final\_slice\_points\_#.dat' and the new estimated centers are saved in 'projected\_center\projected\_center\_#.dat'. Finally, the vectors from the image centroid to the upper-left-hand corner are plotted to allow for visual confirmation of slice location as seen in Figure 55.

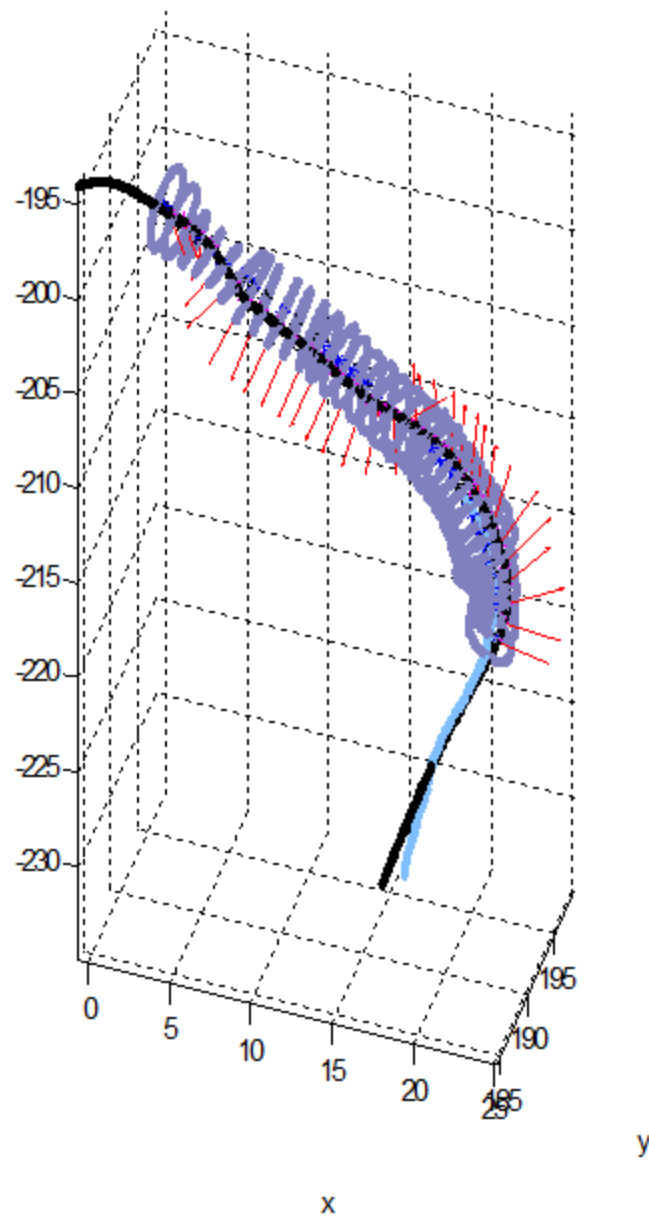


Figure 55: Final rotated segments with the centerline (blue) and transducer pathway (black). Also, the upper-left hand corner of the images is tracked and plotted.

n. **Program:** *OCT\_segment\_creator.m*

- i. Function: Create a group of segments that can be loaded into Simvascular.

- ii. **Input:** The segment matrix is the same as previous programs. Coordinate shifts found previously are set as the ‘Xshift’, ‘Yshift’, and ‘Zshift’, respectively. At line 55, set the name you wish to call the group (Figure 56).

```

54      % creating the groups file for the common and internal carotid
55 -   fid = fopen('lcx_post','w'); %%%Group name here, "testmatlabcy1"
56 -   for i = 1:length(segment)
57 -       s=segment(i);
58 -       ns=num2str(s);

```

Figure 56: Naming the group for Simvascular.

- iii. **Output:** A group with the assigned name is created and saved in the ‘groups’ file.

o. **Program:** *OCT\_group\_content\_creator.m*

- i. **Function:** This program creates the group contents file necessary to load groups into Simvascular
- ii. **Input:** At line 29, change the group name to match that of your group (Figure 57). This file only needs to be created once. For multiple group files in the ‘groups’ directory, manually edit the group contents file.

```

28      %%% Group is labeled here, "lcx_post" in this case.
29 -   fprintf(fid,'\n group_readProfiles (lcx_post) file join $grpdir {lcx_post}');
30 -   fprintf(fid,'\n');

```

Figure 57: Naming the groups in the group\_contents file.

- iii. **Output:** The 'group\_contents' file is saved. Move this file into the 'groups' directory.
- p. Copy 'new\_cl.dat', 'reg\_points\_trans.dat', and 'trans\_interp\_pts.dat' into the 'Post\_Stent' directory. Perform the OCT Image Processing programs from part two, this time isolating the stent contour.
- q. **Program:** *truncate.m*
  - i. **Function:** Truncate the transducer wire pathway to only include the stented region.
  - ii. **Input:** 'reg\_points\_trans.dat' is loaded into the program. At line 5, set the bounds of 'r' to only include the stented region (Figure 58). .
  - iii. **Output:** 'reg\_points\_trans\_trunc.dat' is saved.

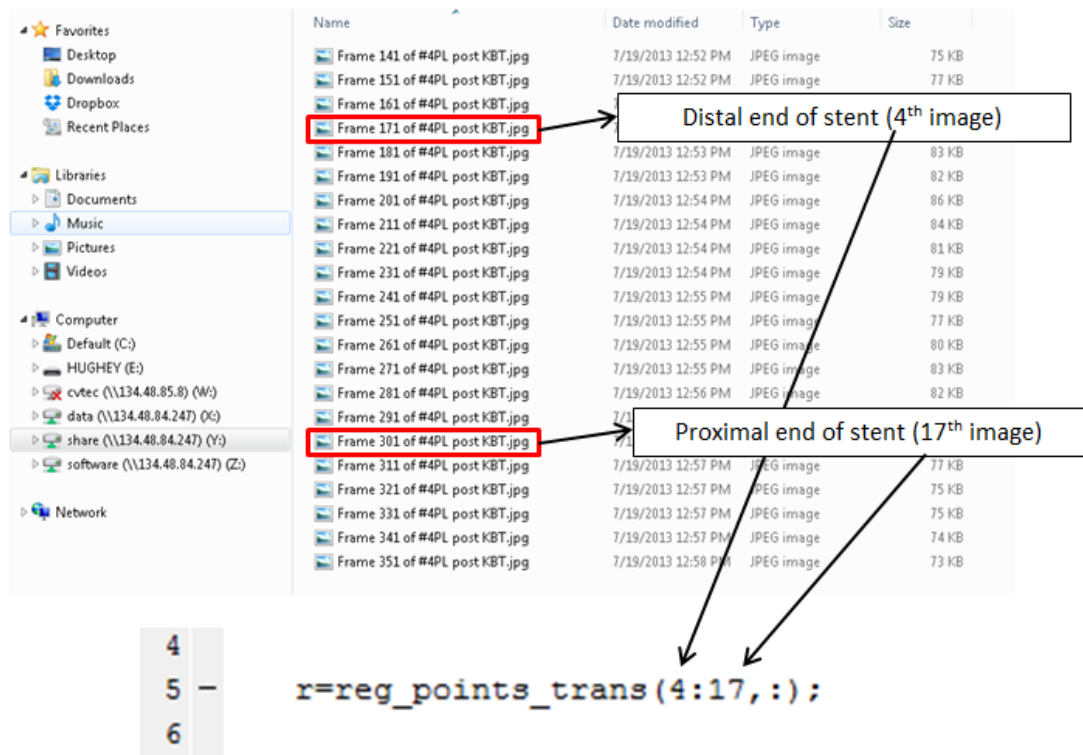


Figure 58: Truncating the transducer pathway based on the stented region.

- r. Run `rotate_OCT_slice_trans.m` (same program as step m), however, for the stented region the program will load 'reg\_points\_trans\_trunc.dat'. No changes need to be made to the code as this program is already set in the demo files within the 'Post\_Stent' directory.

#### 4. Virtual Stent Implantation

- a. **Preprocessing:** For preparation of the stent model, creating a thin-wall model from the stent outer boundary, and flexing the stent model, see instructions created by Timothy Gundert in

Instructions\_for\_Implanting\_Stents\_in\_OCT\_model.doc. Note the Boolean operations should be performed as described below.

- b. **Program:** *implant\_stent\_intersect.tcl*
  - i. **Function:** Perform Boolean operations using Simvascular to virtually implant the flexed stent into the vessel model.
  - ii. **Input:** Edit *implant\_stent\_intersect.tcl* using a text editor such as Notepad. Scroll to the bottom of the document under the ‘Parameters’ section. Change the parameters to match the file names and save the file. Parameters are defined below. In Simvascular, navigate to the directory containing the files as well as the *implant\_stent\_intersect.tcl*. To run the script, enter “source implant\_stent\_intersect.tcl”. This command executes the file and saves the output.

thinWallFileName- shell model

thickStentFileName- flexed thick stent

lumenFileName- lumen model

outputSolidFileName- desired output file name

## 5. Circumferentially Shifting Stent

- a. **Preprocessing:** Perform a simulation using arbitrary boundary conditions and write output files. Create the ‘wss.vtk’ file. Load the ‘wss.vtk’ file into Paraview. Select and apply slices using locations from the ‘group’

file. Save the slices and their respective OCT images in a separate directory.

b. **Program:** *orient.m*

- i. **Function:** This program provides circumferential shifts that can be applied to the stent in Solidworks. This allows for a more accurate model of the stented coronary artery.
- ii. **Input:** 'Slice' is the name of the comma separated value spreadsheet saved from the Paraview slice. 'OCT' is the OCT image corresponding to Paraview slice. 'Center\_point' is the center of the slice and can be found in the 'group' file. Inputs can be seen in Figure 59.

```

9
10 - slice= csvread('vtk_slice.csv',1,1);
11 - oct = imread('Frame 186 of #7-8 Xience Prime 2.5-18 post POBA.jpg');
12 - center_point = ([128.584 101.847 43.363]); % group file: position number for specific slice
13

```

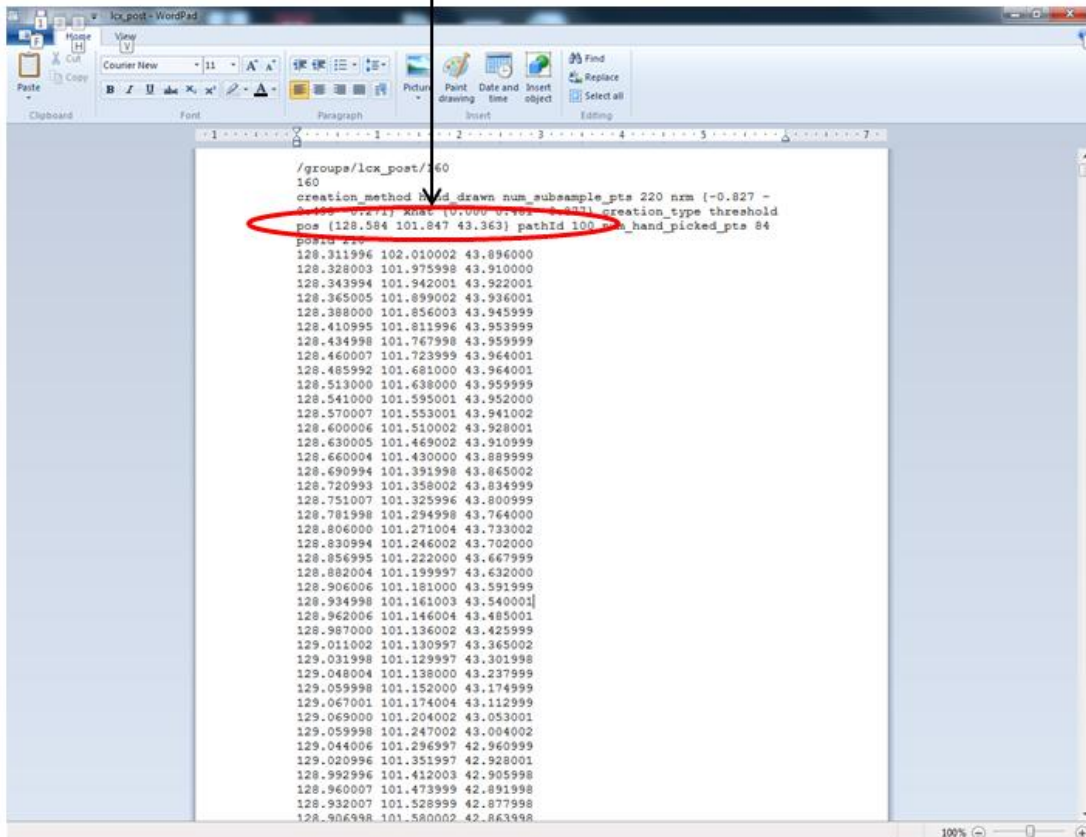


Figure 59: Inputs for orient.m.

When the program is ran, the Paraview slice will appear. Using the mouse, the user should select three strut locations. Next, the OCT image will appear. The user should first select an estimation of the contour center followed by three struts similar to the Paraview slice locations.

- iii. **Output:** Circumferential rotations will be displayed in the Matlab command window. This program should be run for three locations



(proximal, middle, and distal) within the stented region. Using the rotate feature in Solidworks as seen in the Virtual Stent Implantation Instructions by Timothy Gundert, rotate the stent using an average of the three circumferential rotations. Repeat as necessary.

## 6. Zero Degree Positioning for Local Quantification

- a. **Preprocessing:** Apply and save Paraview slices for desired regions of quantification. Slices should be applied to both the stented and unstented model. Using the README.doc within the Unwrapping directory in the Code Repository as well as the corresponding Matlab programs created by Timothy Gundert, unwrap both the post-stent and follow-up models assigning the epicardial surface as the zero degree location. Load the zero degree text files (.dat files) into Paraview and save them as comma separated value files in the directory containing the follow-up reconstruction files.
- b. **Program:** *rotate\_OCT\_slices\_trans\_final.m*
  - i. **Function:** The purpose of this program is to correlate post-stenting WSS and neointimal thickness at follow-up. Specifically, this program shifts the zero degree location to a spatially consistent point at the epicardial surface between post-stenting and follow-up.
  - ii. **Input:** Created from *rotate\_OCT\_slices\_trans.m*. All files being input are the same from *rotate\_OCT\_slices\_trans.m*. In addition, the zero degree location (epicardial surface) from unwrapping is

loaded. At line 137, 's' should be set to the OCT image being quantified (Figure 60).

```

136 |
137 - | if s==146 % || s==207 || s==238 || s==267 || s==282 || s==315 || s==330 || s==345 || s==372 || s==390 || s==411
138 - |     eval(['final_slice_points_2' ns '='[final_slice_points_' ns '(:,1) final_slice_points_' ns '(:,2) final_slice_poin
139 - |     eval(['cent_zerx' ns '=sum(final_slice_points_' ns '(:,1))/(length(final_slice_points_' ns '));']);
140 - |     eval(['cent_zery' ns '=sum(final_slice_points_' ns '(:,2))/(length(final_slice_points_' ns '));']);
141 - |     eval(['cent_zerz' ns '=sum(final_slice_points_' ns '(:,3))/(length(final_slice_points_' ns '));']);
142 - |     eval(['cent_cont=[cent_zerx' ns ',cent_zery' ns ',cent_zerz' ns '];']);
143 |

```

Figure 60: Setting 's' to be the OCT image being quantified.

At line 267, 'deg\_shift' is calculated (Figure 61). 'Deg\_shift' determines which direction the rotation of the zero degree point is applied.

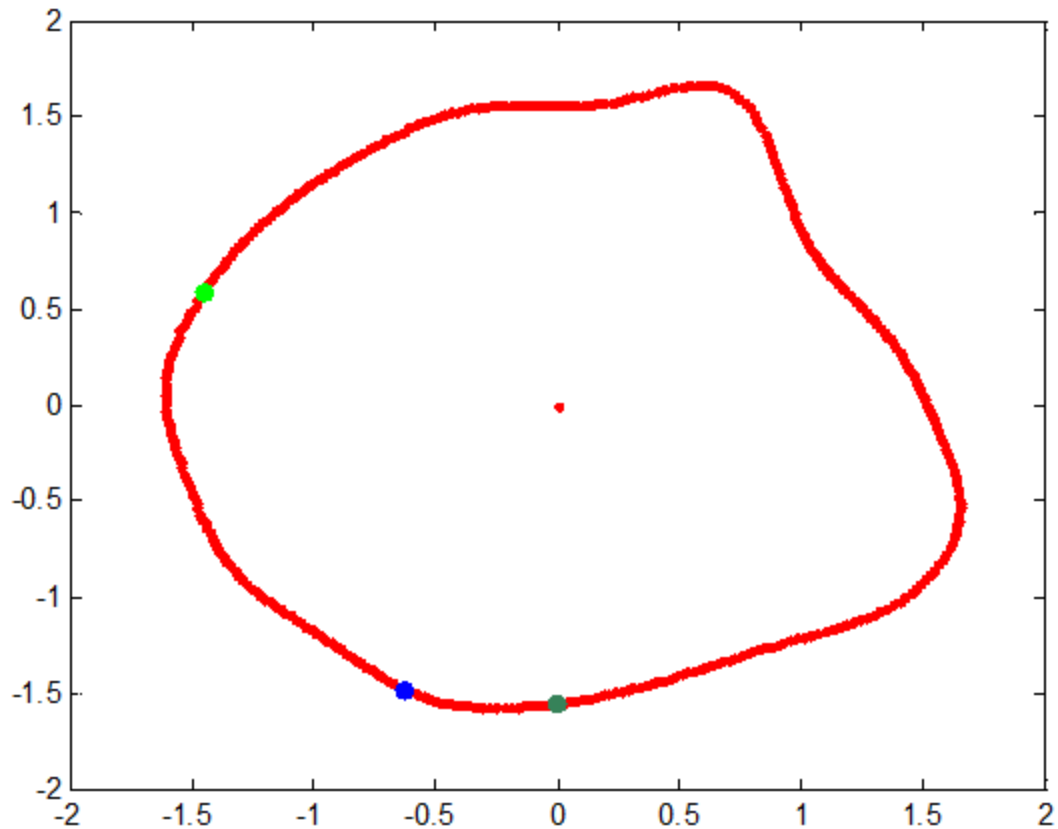
```

274 | % Make Sure green (epicardial) and black (shifted zero) dots are on
275 | % same spot, else comment out deg_shift that was used and use other
276 | %deg_shift=360-round(theta_deg_cut);
277 - | deg_shift=round(theta_deg_cut);
278 |

```

Figure 61: Determining 'deg\_shift', if the circumferential shift was applied in the wrong direction, comment out 'deg\_shift' that was used and un-comment the other one. Note, one instance must be commented.

- iii. **Output:** Figure 1 is the Paraview slice showing the initial zero degree location (forest green point), epicardial surface (lime green point), final zero degree location after rotation (black point), and the final 90 degree location after rotation (blue point). The epicardial surface and final zero degree location should be in the same position (i.e. black point should be hidden behind lime green point) as seen in Figure 62.



*Figure 62: Final zero and epicardial surface (lime green point) are in the same location. Initial zero degree location (forest green point) and final 90 degree locations (blue point) are also plotted.*

If they are not in the same position (Figure 63), the shift was applied in the wrong direction and the 'deg\_shift' that was used must be commented out and the other one used. Re-run program if necessary.

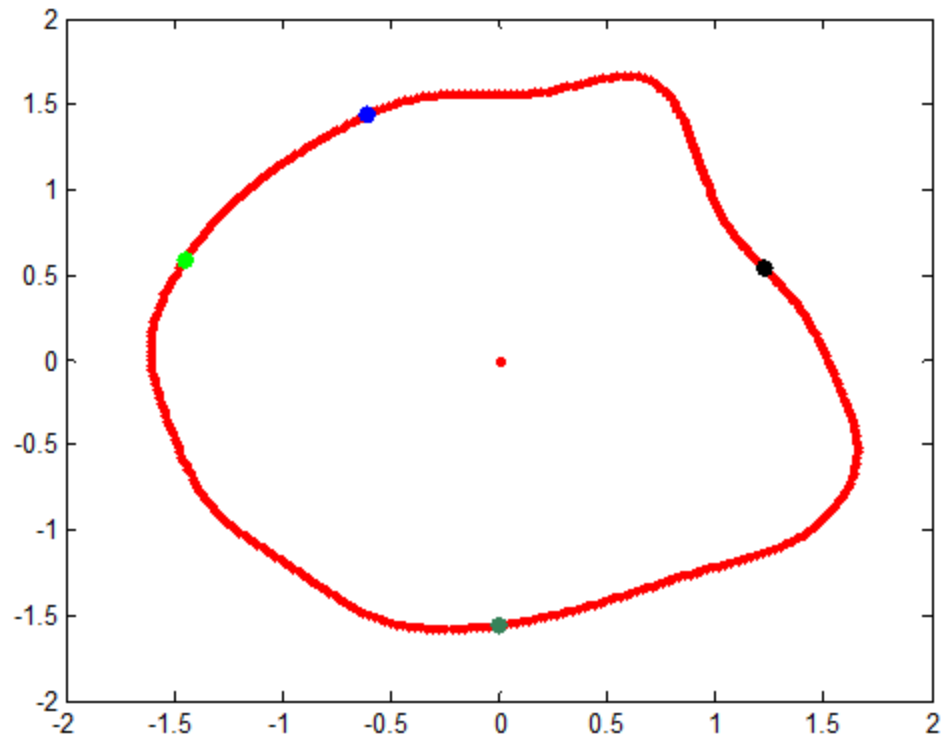


Figure 63: Example of shift being applied in the wrong direction. Final zero degree location (black point) and epicardial surface (lime green point) do not overlap.

‘Final\_wss\_angle’ is output and is a matrix where the first column is the angle (0-359) and the second column is the WSS value corresponding to that angle. Final WSS versus angle is also plotted as seen in Figure 64. Copy and paste ‘final\_wss\_angle’ into a separate excel spreadsheet for linear regression analysis.

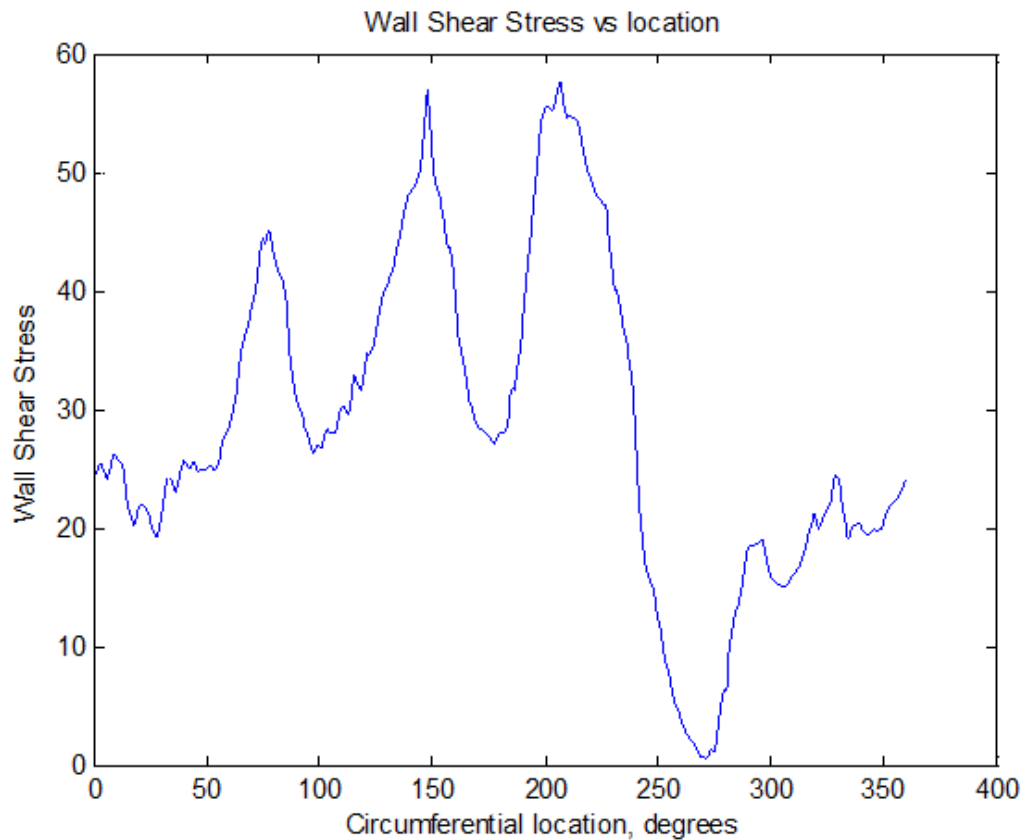


Figure 64: WSS versus circumferential location plot.

‘Theta\_deg’ is displayed in the Matlab command window and is the circumferential shift for the follow-up thickness calculation.

c. **Program:** *thickness.m*

- i. **Function:** Calculate the thickness of select OCT images at follow-up using the epicardial surface as the zero-degree location.
- ii. **Input:** ‘Segment’ is the number corresponding to the OCT image being quantified. Coordinate shifts found previously are set as the ‘Xshift’, ‘Yshift’, and ‘Zshift’, respectively. ‘Theta\_deg’ is the

circumferential shift found from *rotate\_OCT\_slices\_trans\_final.m*.

Inputs can be seen in Figure 65.

```
12
13 - segment=[201]; % 345 390 238 267 315 372 411
14 - num_im=length(segment);
15 - theta_deg=142;
16 - theta_deg=round(theta_deg);
17
18 - Xshift=120.6995;
19 - Yshift=-97.30051;
20 - Zshift=222.77318;
21
```

Figure 65: Inputs for *thickness.m* program.

- iii. **Output:** ‘Thickness#’ is created and plotted where # corresponds to the slice number (Figure 66). ‘Thickness#’ is a matrix where the first column is the angle (0-359) and the second column is the thickness value corresponding to that angle. Copy and paste second column of ‘thickness#’ into the same spreadsheet as the WSS results for linear regression analysis.

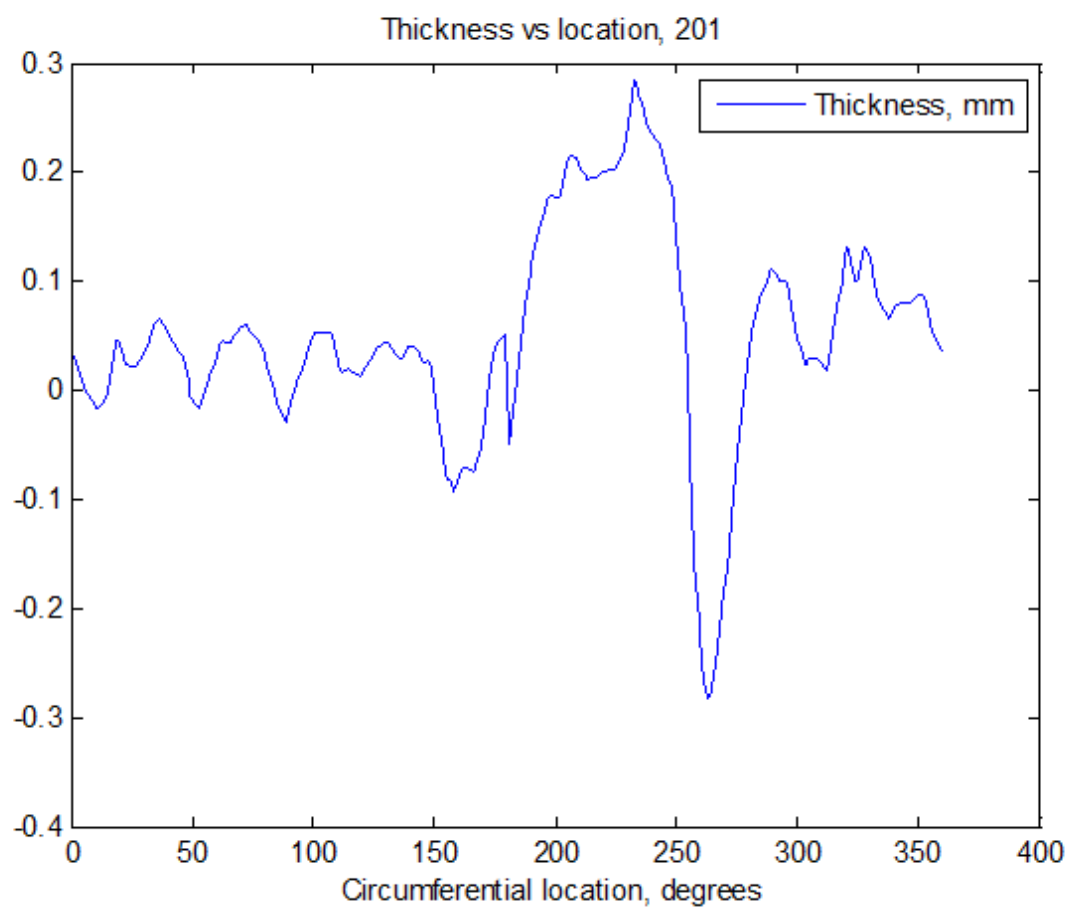


Figure 66: Thickness versus circumferential location plot.